8-27-2009

Analysis of moment-preserving methods for charged particle transport

Paul Smith

Recommended Citation

Smith, Paul. "Analysis of moment-preserving methods for charged particle transport." (2009). https://digitalrepository.unm.edu/ne_etds/47

Paul H. Smith

Candidate

Chemical and Nuclear Engineering

Department

This thesis is approved, and it is acceptable in quality and form for publication on microfilm:

Approved by the Thesis Committee:

AKPrinja, Chairperson

Taro Ueki

Adam H

Accepted:

Dean, Graduate School

Date

Analysis of Moment-Preserving Methods for Charged Particle Transport

by

Paul H. Smith

B.S. Nuclear Engineering
University of New Mexico, 2007

THESIS

Submitted in Partial Fulfillment of the
Requirements for the Degree of

Master of Science
Nuclear Engineering

The University of New Mexico

Albuquerque, New Mexico

August, 2009

Dedication

I dedicate this work to my wife, Angelina, and two wonderful children, Elijah and Jenae, without whom I would not be myself.

Acknowledgments

I acknowledge the hard work of my advisor and mentor Anil Prinja. His ideas made this work possible and his guidance and wisdom kept me on track. I would like to thank him for the opportunities that he has given me, and I only hope that I've lived up to his expectations. I would also like to thank my friend and colleague, Lee Harding. He helped me countless times through this work, and it was the parallels to his own work that helped me realize my errors. In addition, I thank the entire UNM Chemical and Nuclear Engineering faculty, notably Bob Busch, Gary Cooper, Mohammed El-Genk, and Taro Ueki. I spent my undergraduate and graduate years learning from them, and their lessons won't be forgotten soon. Finally, I would like to thank my mom, dad, and two brothers for their continued encouragement. Who know's where I would be without them.

Analysis of Moment-Preserving Methods for Charged Particle Transport

by

Paul H. Smith

ABSTRACT OF THESIS

Submitted in Partial Fulfillment of the
Requirements for the Degree of

Master of Science
Nuclear Engineering

The University of New Mexico

Albuquerque, New Mexico

August, 2009

Analysis of Moment-Preserving Methods for Charged Particle Transport

by

Paul H. Smith

B.S. Nuclear Engineering
University of New Mexico, 2007

M.S., Nuclear Engineering, University of New Mexico, 2009

Abstract

The simulation of electrons, protons, and other charged particles can be an expensive computation. On the one hand, the small mean free path of a charged particle makes direct simulations very costly. On the other hand, the cross sections are very singular making a deterministic calculation difficult to impossible. Nevertheless, the accurate computation of high energy charged particle densities is an important task for many engineering calculations.

In this thesis, a variety of methods for computing these densities and distributions are assessed. Among these methods are the well-known Fokker-Planck and Fermi approximations. These methods are known to be particularly bad for electrons. It is shown in this thesis that they are in fact very poor for all charged particle transport. Specifically, it will be seen that the Fokker-Planck method and the Fermi

approximation that can be derived from it allow for higher order spatial and angular modes to creep into the solutions for shallow and deep penetrations alike. On the other hand, the true physics only requires a few modes at deeper penetrations. Also, for shallow penetrations, most of the modes of the actual solution to the transport equation are incorrectly approximated by the Fokker-Planck approximation.

It has been realized in recent years that the Fokker-Planck approximation is simply a leading order term in an asymptotic approximation. This realization with some clever manipulation of mathematical operators allows one to obtain higher order approximations to the scattering operator. The Fokker-Planck operator is then simply a specific case of this general framework. This general framework is explained in great detail. The inability of these higher order approximations to capture the true physics in some situations is assessed.

Finally, hybrid methods will be introduced with parallels made to the well known Boltzmann Fokker-Planck approximation. It is seen that the higher order approximations used in place of the Fokker-Planck approximation can make the method more robust, more accurate, and more efficient. Also, parallels between the hybrid methodology and naturally occuring physics that is associated with very heavy ions incident on light targets will be seen. A general framework for approximating the solutions to these types of equations by using a lab frame analysis of the relevant physics will be introduced.

Contents

List of Figures

List of Tables

Glossary

Z_i, Z_t	Atomic number of incident and target particles respectively (1 for electrons or positrons).
A_i, A_t	Atomic mass number of incident and target particles respectively.
M_i, M_t	Incident and target particle masses respectively
e	Fundamental unit of charge, $e \approx 1.602 \times 10^{-19}$ C.
ϵ_0	Vacuum permittivity, $\epsilon_0 \approx 8.854 \times 10^{-12}$.
c	Speed of light in vacuum, $c \approx 2.998 \times 10^9$ m/s.
m_e	Mass of an electron, $m_e \approx 0.511$ MeV/c^2.
r_e	Classical radius of an electron, $r_e \approx 2.818 \times 10^{-15}$ m.
α	Fine structure constant, $\alpha \approx \frac{1}{137}$
β	Relativistic velocity ratio of the incident particle $\frac{v}{c}$
γ	Relativistic parameter, $\gamma^2 = \frac{1}{1-\beta^2}$
τ	Particles kinetic energy in units of electron rest mass, $\tau = \frac{E}{m_e c^2}$.
$\psi(\mathbf{r}, \Omega, E)$	Angular flux

Ω, Ω'	Incident and deflected directions of a particle mapped on the unit sphere.
$d\Omega$	Differential of solid angle, $d\Omega = sin\theta d\theta d\phi = d\mu d\phi$.
E	Particle energy.
p	Particle momentum.
θ_0, μ_0	Scattering angle and its cosine in the center of mass frame, $\mu_0 = \cos(\theta_0) = \Omega \cdot \Omega'$
θ,μ	Angle between particle's direction vector and the positive z-axis of the local spherical coordinate system, $\mu = \cos(\theta) = \Omega_3$
Q, Q_{min}, Q_{max}	Collisional energy loss of particle, cutoff energy loss, and maximum possible energy loss respectively.
$\sigma_e, \sigma_{t,e}$	Microscopic elastic scattering DCS and total elastic scattering cross section, $\sigma_{t,e} = \int_{-1}^{1} \sigma_e(\mu) d\mu$.
$\sigma_{in}, \sigma_{t,in}$	Microscopic inelastic scattering DCS and total inelastic scattering cross section, $\sigma_{t,in} = \int_{Q_{min}}^{Q_{max}} \sigma_{in}(Q) dQ$.
$\Sigma_e, \Sigma_{t,e}$	Macroscopic elastic scattering DCS and total elastic scattering cross section, $\Sigma_{t,e} = \int_{-1}^{1} \Sigma_e(\mu) d\mu$.
$\Sigma_{in}, \Sigma_{t,in}$	Macroscopic inelastic scattering DCS and total inelastic scattering cross section, $\Sigma_{t,in} = \int_{Q_{min}}^{Q_{max}} \Sigma_{in}(Q) dQ$.
θ_1	Lower bound on validity of Rutherford scattering due to Rossi
θ_2	Upper bound on validity of Rutherford scattering due to Rossi

Chapter 1

Introduction

There are many applications in physics and engineering that require an accurate determination of charged particle densities in a medium. In medical applications, one would like destroy a tumor by locally depositing a large quantity of energy. This can be accomplished by aiming a collimated beam of high energy protons or heavier ions at the tumor. Though this process is theoretically very sound and well understood, specific treatment plans for patients and various predictive analyses require a model for repetitive calculations of dose.

There is also great interest in accurately calculating the effectiveness of radiation shielding designs for satellite electronics. Given the large cost of sending heavy objects into space, it is of interest to NASA and other agencies to reduce the weight of their payloads. However, the harsh environment in space demands a large amount of shielding for many payloads. Meeting this demand while keeping weight to a minimum thus becomes a primary goal for engineers with these organizations.

These are just a couple of the applications for charged particle transport calculations. Others include fission damage in reactor materials, semiconductor design, and particle accelerator operation. We will see later that the physics of charged particle interactions, governed by long range Coulomb interactions, makes a direct solution of the transport equation for these problems too computationally demanding. Even with computing resources becoming more advanced and widely available, these problems are still too costly to run using standard Monte Carlo or deterministic algorithms. Yet, even as we see the growing need for accurate and efficient electron and ion transport codes, it is a surprise to find that many of the codes in use today still use very old approximations with well know flaws.

It is the objective of this thesis to systematically examine many of the approximations used in high energy proton and ion transport. In many cases, the theory behind these approximations predate mainstream computing languages. The goal will be to identify under what conditions the old algorithms break down and why they break down. Newer models developed only recently that have yet to be implemented in large scale computing architectures will also be presented. The theory behind these methods, and how the newer methods are connected to the older methods will be discussed.

The second chapter will be an introduction to transport theory. Without transport theory, the ideas presented in this thesis do not exist. It is the need to resolve particle density in both physical space and velocity space that we arive at such a challenging problem. In the third chapter, the physics of charged particles will be discussed. We will see how the problem becomes very challenging, even by the standards of transport theory. Also, the physical intuition needed to understand the results will be developed in this chapter.

The fourth chapter is brief discussion of the Fokker-Planck and Fermi approximations. These approximations, though having known flaws, are important for understanding the developments of later chapters. Also, these approximations appear in production level codes to this day, so it is worthwhile to understand the point at which they fail. In the fifth and sixth chapters, the research that has been this thesis is based on will be discussed. Numerical experiments will be given to help us understand how good or how bad the moment preserving methods can be. Drawing on the knowledge gained from previous chapters, a clear understanding of the methods can be found.

Chapter 2

An Introduction to Transport Theory and Methods

Transport theory has been an important topic for describing many types of phenomena. For nuclear engineers, the transport equation is a very accurate description of the balance of neutrons within the phase space inside a reactor. Though a resolution of the full phase space density of particles is rarely needed in applications, its resolution is required to accurately obtain quantities that can be derived from it. In this chapter, we will discuss some basic concepts that pertain to transport theory. We will also given a brief introduction to the major numerical techniques used to solve the transport equation.

2.1 The Transport Equation

As an introduction to the topics being discussed in this thesis, we will briefly discuss the Boltzmann transport equation, often just called the transport equation by professionals in the field. The steady state equation can be written in general as

$$\begin{aligned}
&\Omega \cdot \nabla\psi(\mathbf{r},\Omega,E) + \Sigma_t(\mathbf{r},E)\psi(\mathbf{r},\Omega,E) = \\
&\quad\int_0^\infty dE' \int_{4\pi} d\Omega' \Sigma_s(E' \rightarrow E, \Omega\cdot\Omega')\psi(\mathbf{r},E',\Omega') + S(\mathbf{r},\Omega,E) \qquad (2.1)\\
&\psi(\mathbf{r}_b,\Omega,E) = \Gamma(\mathbf{r},\Omega,E), \quad \Omega\cdot\mathbf{n} < 0 \qquad (2.2)
\end{aligned}$$

The variable Ω represents a point on the unit sphere and is given by the unit vector pointing in the direction of travel of the particle. It is often referred to as just the angle of the particle. In addition, we have introduced the particle's position vector $\mathbf{r}$ and kinetic energy E. The dependent variable $\psi(\mathbf{r},\Omega,E)$ is known as the angular flux. The transport equation represents a balance in phase space, where we may have particles being redistributed in energy and angle based on the integral term. The source $S(\mathbf{r},\Omega,E)$ often contains additional terms that depend on the angular flux such as particle production due to nuclear absorption and decay.

The boundary condition is called a partial range boundary condition because it only involves the portion of phase space that is pointing inward at the boundary which is completely characterized by its outward normal vector $\mathbf{n}$. The meaning of the partial range boundary condition is that we cannot specify particles leaving the system because that is part of the solution to the equation. For this reason, the transport equation can only be used on domains without reentrant surfaces, characterized by locally concave portions where particles can leave one surface and enter in an adjacent surface.

Much of the particular physics of the transport equation is in the macroscopic cross sections Σ_t and the double differential cross section $\Sigma_s(E' \rightarrow E, \Omega\cdot\Omega')$. It is noted by the form of the double differential cross section that the only important quantity for determining the angular redistribution of particles in the medium is the angle between the incoming and outgoing direction vectors θ_0 or equivalently the cosine of this angle μ_0. In the absence of absorption, the double differential cross section and the total cross section are related by

$$\Sigma_t(E') = \Sigma_s(E') \equiv \int_0^\infty dE \int_{-1}^{1} d\mu_0 \Sigma_s(E' \to E, \mu_0) \tag{2.3}$$

When absorption is present, $\Sigma_t(E') = \Sigma_s(E') + \Sigma_a(E')$. The cross sections are dependent both on the medium and the incident particles. Even in the absence of complicated flux dependent source, we can still get widely varying behavior of the system depending on the particular form that the cross sections take.

In practice, only the energy loss, $Q = E' - E$ and the scattering cosine $\mu_0 = \Omega \cdot \Omega'$ needs to be specified to compute the redistribution of particles. The azimuthal angle ϕ is uniformly distributed during a scattering event. Furthermore, the two quantities, μ_0 and the final energy E are highly correlated in most models. This gives rise to additional complications when studying the behavior of Eq.(2.1). Often times, the scattering kernel is rewritten

$$\Sigma_s(E' \to E, \mu_0) = \Sigma_s(E') p(E' \to E, \mu_0) \tag{2.4}$$

where the normalized probability distribution in energy and angle $p(E' \to E, \mu_0)$ is introduced. It satisfies

$$\int_0^\infty dE \int_{-1}^{1} d\mu_0 p(E' \to E, \mu_0) = 1, \quad 0 < E' < \infty \tag{2.5}$$

The distribution can be further expanded using the Legendre polynomials, $P_l(x)$.

$$p(E' \to E, \mu_0) = \sum_{l=0}^{L} \frac{2l+1}{4\pi} f_l(E' \to E) P_l(\mu_0) \tag{2.6}$$

Since the integral is over solid angle Ω', we must use the addition theorem for Legendre polynomials[2] to obtain

$$p(E' \to E, \mu_0) = \sum_{l=0}^{L} f_l(E' \to E) \sum_{m=-l}^{l} Y_l^m(\Omega) Y_l^{*m}(\Omega') \tag{2.7}$$

where $Y_l^m(\Omega)$ are the spherical harmonics with the normalization

$$\int_{4\pi} d\Omega Y_l^m(\Omega) Y_{l'}^{*m'}(\Omega) = \delta_{ll'} \delta_{mm'} \tag{2.8}$$

Often the energy dependence is removed by introducing a multigroup transport method. In this case, the $f_l(E' \rightarrow E)$ becomes $f_l^{g \rightarrow g'}$ where g represents an energy group. The result of transforming to a multigroup form is ultimately to identify $\psi(\mathbf{r}, \Omega, E)$ with $\psi^g(\mathbf{r}, \Omega)$ and append all of the other parameters in Eq.(2.1) with a g superscript to identify which group the equation represents. To avoid confusion, these superscripts will be left off.

This expansion allows for various numerical methods that are deterministic in nature to be applied in solving Eq.(2.1). The two most well known methods are the S$_N$ method and the P$_N$ method. The S$_N$ method, or discrete ordinates method, uses a highly accurate quadrature formula to approximate the integral term. To do this, we must specify a discrete solution in angular space given by

$$\psi(\mathbf{r}, \Omega, E) = \begin{cases} \psi_n(\mathbf{r}) & : \quad \Omega = \Omega_n \\ 0 & : \quad \Omega \neq \Omega_n \end{cases} \qquad 1 \leq n \leq N \tag{2.9}$$

Substituting this into Eq.(2.1) gives the discrete ordinates equations

$$\begin{aligned} &\Omega_n \cdot \nabla\psi(\mathbf{r})_n + \Sigma_t \psi_n(\mathbf{r}) = \\ &\Sigma_s \sum_{l=0}^{L} f_l \sum_{m=-l}^{l} Y_l^m(\Omega_n) \sum_{k=0}^{N} C_k \psi_k(\mathbf{r}) Y_l^m(\Omega_k) \end{aligned} \tag{2.10}$$

The values of C_k are given by the quadrature set that has been optimized for the problem. Typically, Gaussian quadrature is used.

The S$_N$ equations are a set of first order partial differential equations in space. It can, in principle, be solved very accurately with well established finite element methods. In reality, a very complicated method for solving the equations must be concocted so that a flow of particles may be established in the system. Also, we see that a sum over all $\psi_n(\mathbf{r})$ comes in on the right hand side due to the integral term in Eq.(2.1). To get the solution at a point, the solution at every other point is required first. Thus, the solution to Eq.(2.10) involves an iteration over the angular variable, known as source iteration, where a complicated solution to a PDE is required for all n at every iteration. This iteration can be very time consuming when scattering becomes dominant. In this case, acceleration schemes can also be used under the assumption that the scattering follows a certain behavior. Finally, since the solution is assumed to exist only on rays Ω_n, the solution for small N exhibits artifacts known as ray effects. These can only be mitigated by increasing the number of rays N.

The other prevailing deterministic solution to Eq.(2.1) is the P_N method, also known as the spherical harmonics method. In this method, we identify the moments of the solution by

$$\psi_l^m(\mathbf{r},E) \equiv \int_{4\pi} d\Omega Y_l^m(\Omega)\psi(\mathbf{r},\Omega,E) \tag{2.11}$$

and of the source by

$$S_l^m(\mathbf{r},E) \equiv \int_{4\pi} d\Omega Y_l^m(\Omega)S(\mathbf{r},\Omega,E). \tag{2.12}$$

Then the P_N equations can be written as

$$\begin{aligned}\sum_{l=0}^{L}\frac{2l+1}{4\pi}\sum_{m=-l}^{l}\left[\int_{4\pi} d\Omega\Omega Y_l^{*m}(\Omega)Y_{l'}^{m'}(\Omega)\right]\cdot\nabla\psi_l^m(\mathbf{r})&\\ +(\Sigma_t-\Sigma_s f_l)\psi_l^m(\mathbf{r}) = S_{lm}&\end{aligned} \tag{2.13}$$

These equations appear rather tame except for the integral on the left side. The integral gives rise to a sum over other moments due to a lack of orthogonality of $\Omega Y_l^{*m}(\Omega)$ and $Y_{l'}^{m'}(\Omega)$. This expression is very complicated, so its one dimensional analog is given instead. In this case, $\Omega = \mu$ and $Y_l^m(\Omega) = P_l(\mu)$ and the relation is written

$$\int_{-1}^{1} d\mu\mu P_l(\mu)P_{l'}(\mu) = \frac{2(l+1)}{(2l+1)(2l+3)}\delta_{l',l+1} + \frac{2l}{(2l-1)(2l+1)}\delta_{l',l-1} \tag{2.14}$$

From Eq.(2.14) and the form given by Eq.(2.13) we see that the P_N equations couple higher moments to lower moments. This leads to a lack of closure of the system for finite L in general and leads to a very complicated matrix equation to solve in practice. The resulting system for dimensions higher than 1 were so formidable that the P$_N$ method wasn't even an option for solving the transport equation until the advent of the modern computers. Other complications arise in the specification of boundary conditions and in an apparent smearing of solutions that are discontinuous in Ω due to the well known Gibbs phenomena. Therefore, the method still has caveats that have not been addressed in full and there are comparatively fewer engineers using this method than those using the S$_N$ method.

This has been a brief introduction to transport theory. For more information on general transport theory considerations, the reader is referred to the extensive literature on the subject. For the problem at hand, we will see that deterministic methods pose additional complications to an already difficult problem. In particular, extremely fine grids and very large Legendre expansions are needed to get an accurate solution to Eq.(2.1) for high energy charged particles using the methods discussed so far[3]. In most cases, charged particle transport has been done in a Monte Carlo setting. We will discuss this topic more before delving into the specific problems in Chapter 2.

2.2 Analog Monte Carlo Methods

The Monte Carlo method was extensively used during the Manhattan Project by Fermi, von Neumann, Ulam, and others. It was named after a casino in Monaco where Ulam's uncle would borrow money to gamble[4]. The method, as it applies to particle transport, is analogous in many ways to the activities in a casino in that randomness decides individual outcomes, but long term average behavior is deterministic.

A particle being transported through a medium is assumed to follow a Markov chain of events. That is, the particle has no memory of its past, and its state changes at discrete instants corresponding to collisions with atoms of the medium. This process can be imitated easily by sampling outcomes based on cumulative distribution functions. Using this idea, it was realized early on that an exact solution to the transport equation could be found, in principle, by following an infinite number of particle trajectories in the medium. Rigorously, the Monte Carlo method can be thought of a solution to the integral form of the transport equation[2].

The desired quantities, like local dose deposition or transmission coefficients, can be found by scoring the appropriate events when they actually happen. Since an infinite number of trajectories cannot be sampled, one can only get a solution to within a certain, well defined, statistical error. In practice, one can get an answer with a small statistical error within reasonable time constraints for many types of problems. In a Monte Carlo process, a particle is sampled from a source distribution which can be known a priori or developed over the course of the calculation. This particle is moved through a path length that is sampled from a specific distribution. At the end of the path length, the particle has a collision and its state is updated based on other distributions. The distributions come directly from the physics.

For example, suppose we have a continuous distribution of possible outcomes x of a particular event described by the probability distribution function $f(x)$. Then, we have by definition of a cumulative distribution function

$$F(x) = \int_{x_{min}}^{x} f(x')dx', \tag{2.15}$$

$$\int_{x_{min}}^{x_{max}} f(x')dx' = F(x_{max}) = 1, \tag{2.16}$$

$$\int_{x_{min}}^{x_{min}} f(x')dx' = F(x_{min}) = 0. \tag{2.17}$$

From this, we can also show that $F(x)$ is a bijection in the unit interval. With this information, we know that we can find $F^{-1}(y)$ for any $y \in [0, 1]$. With the Monte

Carlo method, a user compiles each of the cumulative distribution functions that describes the physics of particle transport within the media that they are interested. To sample an event, the user samples a uniform pseudorandom number $\xi \in [0, 1]$ and obtains the outcome $x = F^{-1}(\xi)$. The term pseudorandom is a technicality that has no effect on the accuracy of the method. Pseudorandom numbers are essentially the closest thing to a random number that one can get by using deterministic algorithms.

As a concrete example, consider the random determination of path length between collisions. One would first obtain the number of particles $N(s)$ not removed from a system with macroscopic total cross section Σ_t in a path length of s using the differential equation

$$\frac{dN}{ds} = -\Sigma_t N(s), \quad N(0) = N_0 \tag{2.18}$$

The solution to this equation, $N(s) = N_0 \exp(-\Sigma_t s)$, is proportional to the probability of a particle streaming a distance s within the interval $[s, s + ds]$ before having a collision. We write this as

$$P(s)ds = KN_0 \exp(-\Sigma_t s), \quad 0 < s < \infty \tag{2.19}$$

The constant K is used to meet the normalization condition.

$$\int_0^\infty P(s)ds = \frac{KN_0}{\Sigma_t} = 1 \rightarrow K = \frac{\Sigma_t}{N_0} \tag{2.20}$$

The cumulative distribution function for path length x traveled between collisions then becomes

$$P(x < s) = F(s) = \int_0^s P(s')ds' = 1 - \exp(-\Sigma_t s). \tag{2.21}$$

Note that this CDF has the properties given in Eq.(2.17). Setting $F(x) = \xi$ with ξ a uniform pseudorandom number between 0 and 1, we get

$$x = -\bar{\lambda} \ln(1 - \xi) = -\bar{\lambda} \ln(\xi), \tag{2.22}$$

where we have defined the mean free path $\overline{\lambda} = 1/\Sigma_t$, and we have noted that the random variable $1 - \xi$ is a uniform pseudorandom number between 0 and 1, just like ξ.

The outcome of a collision can be found by using the probability distribution that was identified in Eq.(2.4). For simplicity, we can further break down the distribution as

$$p(Q, \mu_0) = p(E, \mu_0) g(E, Q|\mu = \mu_0) \tag{2.23}$$

where the distribution is now defined in terms of the energy transfer Q. This decomposition explicitly gives the probability distribution in Q for a specific scattering cosine μ_0. Both distributions are normalized to unity and both depend on the particles kinetic energy E. The scattering cosine μ' can be sampled using

$$\xi_1 = \int_{-1}^{\mu'} p(E, \mu_0) d\mu_0 \tag{2.24}$$

and the energy loss Q' from the collision can be sampled using

$$\xi_2 = \int_{Q_{min}}^{Q'} g(E, \mu', Q) dQ \tag{2.25}$$

for two uniform random numbers ξ_1 and ξ_2. It is always possible to get a unique energy loss and scattering cosine from these relationships. However, when the resulting equations do not have an analytical representation, special sampling methods are required. A discussion of these methods are not pertinent here, but a good discussion is given by Kalos and Whitlock[5] and a thorough analysis of their efficiency and accuracy for high energy charged particle transport applications is given by Harding[6].

A three collision realization of some process is shown in Fig.(2.1). The collisions happen in random intervals whose lengths are determined by the three different random numbers $\xi_{1,1}$, $\xi_{2,1}$, and $\xi_{3,1}$. The initial state of the particle is given by

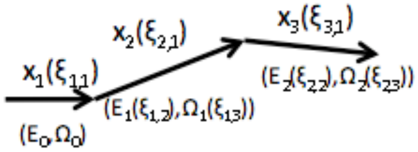

Figure 2.1: A possible realization of an analog Monte Carlo particle history.

(E_0, Ω_0), and it is evolved at each collision using new random numbers and the independent distribution functions given by the physics of the scattering process.

For a comprehensive review of Monte Carlo methods, the reader is referred to the literature. We will see in the next chapter that the methods discussed here are not suitable for solving a charged particle transport problem. The reason is that the number of collisions that are generated by this approach are high and the overall result is very large computational run times. As a result of this difficulty, a number of methods have been developed that are similar in spirit to the analog Monte Carlo calculation, but which explicitly treat collision processes over macroscopic distances.

2.3 The Condensed History Algorithm

One of the most notable approximation methods is the condensed history Monte Carlo algorithm developed largely by Berger in 1963[7]. Different versions of this algorithm can be found in almost any of the major charged particle codes in use today[8, 9, 10]. The algorithm, of course, can take many different forms as it has evolved over the past 45 years.

Many condensed history algorithms are type I, meaning there is no single event sampling of particles. In these algorithms, the particle is moved through a fixed step size based on its energy. Typically, this step size is chosen at the beginning of the calculation to be the path length required to lose a certain fraction of the particle's energy. At the end of the step, a new energy is sampled from an excitation/ionization distribution and a new particle direction is sampled from a multiple scattering distribution.

The energy loss will typically have a continuous slowing down (CSD) component and a straggling component. In electron codes, the Landau distribution[11] for energy straggling is often used for the straggling component, and is sampled at the end of the step. The cosine of the scattering angle may be sampled at several points in an energy step to get an accurate representation of the spatial spreading. For electrons, the Goudsmit-Saunderson[12, 13] or the Moliere[14] distributions are often used for this purpose. With protons and heavier ions, the energy loss straggling is typically sampled from the Vavilov[15] distribution while angular spreading from elastic collisions is sampled from a Gaussian with parameters based on an analysis done by Rossi[16]. These are the prescribed distributions used in MCNP5[8] and in MCNPX[17] as well as other codes [9, 10]

In each of these cases, the multiple scattering theory is based on an analysis of transport in infinite media. The streaming operator can be simplified by expressing it in terms of the pathlength variable s,

$$\Omega \cdot \nabla \psi(\mathbf{r}, \Omega, E) \rightarrow \frac{\partial \psi(s, E)}{\partial s} \tag{2.26}$$

The distance traveled can be treated as a time variable for this purpose since a collimated beam looks like an initial condition in this context. This can only be valid when the particle is far from boundaries and material interfaces. When it is valid, it has been shown that condensed history algorithms have an error that is $O(\Delta s)$ where Δs is the step size [18]. The error is much like a discretization error in that it results from approximating the particles average state over the step by its state at some point on the step. Much like in a discretization scheme, this error can be made to be $O(\Delta s^2)$ or higher by using more complex particle steps, but this would not remove the error due to the nature of the multiple scattering distributions. That is, we cannot remove the intrinsic error that occurs by approximating the spatial component of the transport equation.

Figure 2.2 shows a typical condensed history step when the particles trajectory is sampled over several substeps. In this case, the particle step is made up of six substeps. In each substep, the particle loses a deterministic amount of energy based on the stopping power and the step length. At the end of the step, a new particle trajectory is sampled from a multiple scattering distribution based on a random number ξ_i uniformly distributed in the unit interval, much the same as we saw in the previous section. The particle then moves another step in its current direction with a substep length that can vary with the particle's energy. This continues until the particle reaches the end of the full step. At this point, the particle has only lost a deterministic amount of energy. The energy of the particle is then straggled by sampling from the ionization/excitation distributions with another random number. The particle state at the end of the full step can be written as

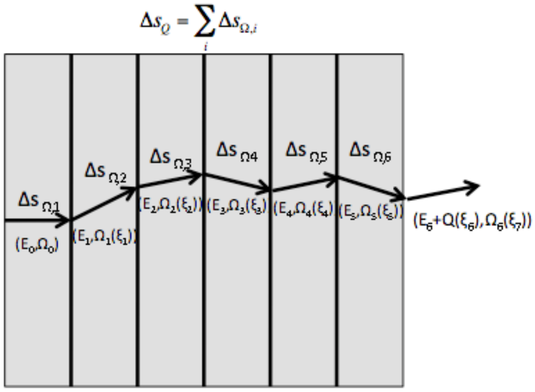

Figure 2.2: A typical type I condensed history energy step with a set of six substeps for sampling angular redistributions.

$$\tilde{\mathbf{r}}_s = \tilde{\mathbf{r}}_0 + \sum_i \tilde{\mathbf{\Omega}}_i \Delta s_i \tag{2.27}$$

$$E_s = E_0 - \Delta E + Q(\xi) \tag{2.28}$$

Here we see that the change in energy through the step ΔE is known in advance and is fixed. The value of $Q(\xi)$ is a random variable sampled from an appropriate distribution. Other type I algorithms may not use a fixed energy loss to define the step. In those cases, the value of ΔE is still calculated in advance based on the step size and the stopping power continuously modeled over the step.

These algorithms are good for approximating the transport of a particle whose state barely changes during a step. However, the type I algorithm breaks down completely when considering the infrequent catastrophic collisions that many charged particles experience. When these cannot be neglected, one uses a type II algorithm where the distance to the next catastrophic collision is sampled, and the particle is moved through fixed steps until reaching that distance. Alternatively, the catastrophic collisions can be built into the step as what happens in the MCNP code's logic [8].

In any case, we see that there are approximations made in the condensed history method that cannot be repaired at run time. That is, we cannot simply adjust the step size to be very small or apply a complicated variance reduction scheme to get a solution that is converging to the true solution. The true solution still eludes the user by virtue of the condensed history method itself. Furthermore, we will see later that these multiple scattering distributions can actually break down completely for cases where the material is very thin and there are several interfaces.

2.4 Moment Preserving Research Overview

The problem with the condensed history method can be identified with both a rigid step structure giving rise to the $O(\Delta s)$ error and an approximation of the distributions based on infinite medium transport calculations. The errors that occur due to these approximations are most apparent near boundaries and interfaces. For this reason, a new method for computing charged particle densities without the approximations of the condensed history method has been needed for quite some time.

One would like instead of a step and sample scheme, to use an event based algorithm where there is not a step structure built in. This would require a pseudo-differential cross section that is derived in some way that is consistent with the true physics but still leads to a computationally efficient treatment. In the next chapter, we will describe the physics of charged particles, and slowly unravel what makes the analog Monte Carlo simulation so slow and so difficult to approximate. What will emerge is a natural way of creating a pseudo-differential cross section based on the physics, not the transport equation itself. Due to the procedures involved, some have coined the term moment preserving methods to describe the general framework for these approximations.

After exploring the moment preserving concept, we will discuss ways of folding these methods with other well established methods such as condensed history. The end product is a set of charged particle algorithms that are more accurate, and in some cases, faster than the established methods. We will present numerical evidence to back these statements.

Chapter 3

Interactions of High Energy Charged Particles

The interaction of charged particles is dominated by long range Coulomb forces. Recall that the potential due to a point charge with Z_t fundamental charge units e can be written

$$V(r) = \frac{1}{4\pi\epsilon_0}\frac{Z_t e}{r} \tag{3.1}$$

For the purpose of high energy charged particle transport, a nucleus can be treated like a point charge. This relationship tells us that the potential energy lost or gained by a particle moving through the field of the nucleus falls off very slowly with distance. Without further analyzing the problem, we can already see that collisions between nuclei will happen frequently as a particle need not even be close to the nucleus to be deflected by it. Compare this reasoning with that of neutral particle interactions where the field of the nucleus has no effect on the particle. It is clear that the number of particle interactions will be far greater for the charged particles.

What is required for a transport calculation is not the potential due to the nucleus, but the differential cross section or DCS. The DCS gives us all of the information that we need to compute the redistribution of particles in energy and direction. Figure 3.1 is two views of the the elastic scattering DCS for high energy neutrons (typically between 1-20 MeV for many applications) and for high energy protons (typically 100 - 1000 MeV) incident on water. For high energy neutrons on water, linearly anisotropic scattering doesn't set in until about 5.5 MeV according to a formula given by Evans[19]. For this reason, the DCS for elastic scattering is nearly flat, and

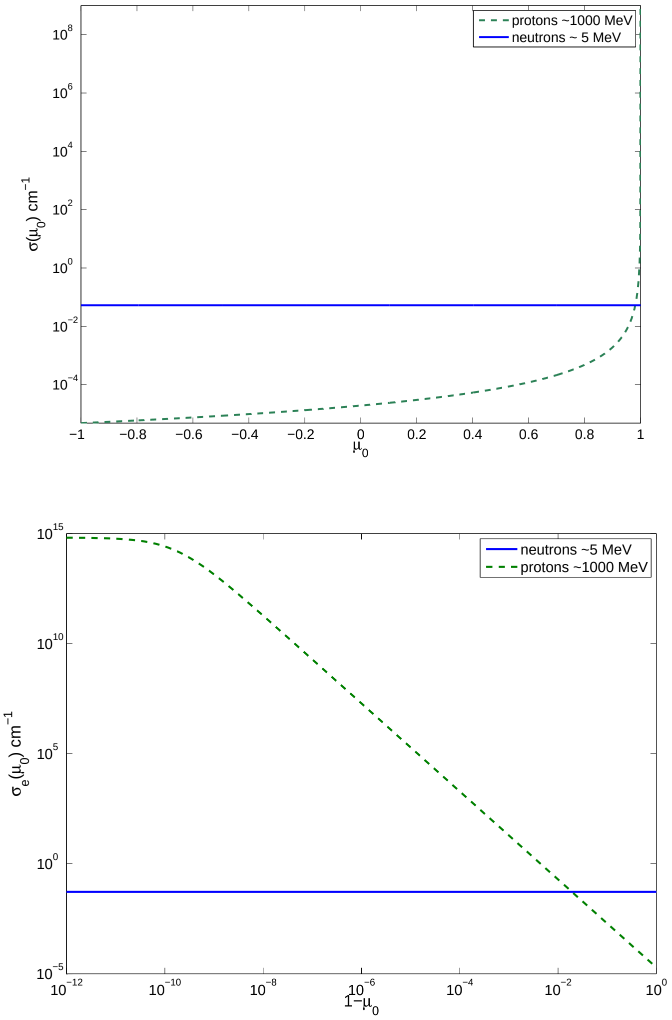

Figure 3.1: Macroscopic DCS for elastic scattering off of water molecules for high energy neutrons and protons.

its magnitude resembles that of a hard sphere approximation given by

$$\sigma_n \approx 4\pi R_A^2 = 4\pi R_0^2 A^{2/3}, \quad R_0 = 0.135 \times 10^{-12} \text{ cm} \tag{3.2}$$

The DCS for protons will be discussed in the next section. The figure on the right shows the two cross sections plotted on a log-log scale for varying $1 - \mu_0$ where $\mu_0 = \cos\theta$ is the cosine of the center of mass scattering angle. From the figures we see that our suspicions are correct. The protons scatter much more frequently than the neutrons, and the scattering angles are peaked near $\mu_0 = 1$ or $\theta = 0$. For lower energy protons, we will see that the DCS is even larger in magnitude and still as forward peaked as in the figure.

The DCS for a given collision type can be found by analyzing the equations of motion for the system. Classically, we can write the equations that describe the kinematics for a general collision as

$$\Delta p = M_1(V_1 - v_1) + M_2(V_2 - v_2) = 0 \tag{3.3}$$

$$\Delta E = M_1(V_1^2 - v_1^2) + M_2(V_2^2 - v_2^2) + Q_r = 0 \tag{3.4}$$

Here we have the classical momentum and energy balance equations. The parameter Q_r is the Q-value of the reaction. It can be set to 0 for elastic collisions. For inelastic collisions where energy is not conserved, this number can be positive for endothermic and negative for exothermic reactions. In what follows, we will discuss the DCS for elastic and inelastic scattering of high energy particles due to interactions with the nucleus and the atomic electrons respectively. These will be the only two types of interactions that will be considered from here on. The other types of reactions that are conceivable make up a negligible amount of the total scattering in many cases and can be neglected.

Its not that the other types of interactions between charged particles are all negligible. Inelastic scattering with the nucleus is very important for protons and heavier charged particles. However, these interactions are very complicated and require sophisticated nuclear models. Also, these reactions result in the spallation of the nucleus and a loss of identity of the incident particle. These collisions are an example of the so called catastrophic collisions that we briefly mentioned in Chapter 1. For this particular brand of catastrophic reaction, we require special handling to account for the byproducts and the final state of the system even with the analog Monte Carlo method. Even when taking these collisions into account, we still must model the elastic and inelastic collisions between the catastrophic collisions. Thus, we will ignore the catastrophic component to the problem without loss of generality.

3.1 Elastic Scattering of Charged Particles off Atomic Nuclei

For an incident particle with Z_i units of fundamental charge, the potential energy function becomes $Z_i e V(r)$ where $V(r)$ is given by Eq.(3.1). A collision occurs when the incident particle is deflected by the field of the target particle. Using Lagrangian mechanics[20], we find that the trajectories are hyperbolic with asymptotic deflection related to the impact parameter by

$$b = |a| \cot\left(\frac{\theta}{2}\right), \quad a = \frac{1}{2}\frac{Z_t Z_i e^2}{E} \tag{3.5}$$

The DCS is given by the expected number of particles crossing the infinitesimal surface area $b\,db\,d\phi$ where ϕ is the azimuthal angle of deflection. We can write the DCS relation as

$$d\sigma_e = b\,db\,d\phi = b\frac{db}{d\theta}d\theta d\phi = \frac{a^2}{4\sin^4(\theta/2)} \tag{3.6}$$

This analysis is completely classical in nature. However, a similar analysis done using wave mechanics yields the same result, a fact that is said to be “accidental”[21]. The

Rutherford DCS is better recognized by introducing the parameter $\mu_0 = \cos\theta_0$ and using the trigonometric identity $\sin^4(\theta) = (1-\cos(2\theta))^2/4$. The resulting form after identifying $\sigma_e \equiv d\sigma_e/d\Omega$ becomes

$$\sigma_e(\mu_0) = \frac{a^2}{(1-\mu_0)^2} = \left(\frac{Z_t Z_i e^2}{2E}\right)^2 \frac{1}{(1-\mu_0)^2} \tag{3.7}$$

This DCS corresponds to a bare point charge deflecting off of another bare point charge. The result is a DCS that is singular at a scattering cosine of unity. This suggests the very singular nature of the process itself since we would expect scattering angles to be small and scattering events to be frequent. In reality, nuclear fields do not behave like this because their field is gradually screened at long distances by the atomic electrons.

Rossi notes that a lower bound on θ can be set if one accounts for the finite size r_a of the nucleus[16] given by

$$\theta_1 = \frac{Z^{1/3}\alpha m_e c}{p}, \tag{3.8}$$

where α is the fine structure constant. This bound is found by analyzing the ratio of the wavelength of the particle λ to the atomic radius r_a and identifying the point at which it becomes too small. Independent of this analysis, Goudsmit and Saunderson found an approximate DCS by using a potential of the form $V(r) = V_0(r)\exp(-r/r_a)$ where $V_0(r)$ is given by Eq.(3.1)[12, 13]. The resulting DCS is

$$\sigma_e(\theta) = \frac{a^2}{4(\sin^2(\theta/2) + \sin^2(\theta_1/2))^2}, \tag{3.9}$$

and using the small angle approximation for the second term in the denominator, one obtains the usual form taken by the screened Rutherford DCS.

$$\sigma_e(\mu_0) = \left(\frac{Z_t Z_i e^2}{2E}\right)^2 \frac{1}{(1-\mu_0+2\eta)^2} \tag{3.10}$$

Here we have introduced the screening parameter $\eta = \theta_1^2$. More accurate formulas for η can be found in certain cases. Notably, there is the formula due to Moliere[14] based on a partial wave analysis of the Klein-Gordon equation and a Thomas-Fermi model of the nucleus.

$$\eta = \left(\frac{\alpha Z^{1/3}}{(0.75\pi)^{2/3}}\right)^2 \frac{1}{\tau(\tau+2)}\left[1.13 + 3.76\left(\frac{\alpha Z_t}{\beta}\right)^2\right] \tag{3.11}$$

The dimensionless parameter $\tau = E/m_e c^2$. There is no reason to believe that this is a more accurate value of η for particles other than electrons. In fact, it is known not to be better for positrons. For this reason, and to keep consistent with Rossi's analysis which is important for comparisons with MCNPX, we will continue to use $\eta = \theta_1^2$ unless specifically noted otherwise. Rossi also gave an upper bound on θ for Rutherford scattering given by

$$\theta_2 = 280 M_t^{-1/3} \frac{m_e c}{p} \tag{3.12}$$

This parameter enters into his theory of multiple scattering, which will be discussed further in the next chapter. It is often set to unity when it becomes greater than unity.

All of the differential cross sections given in this section are for collisions in the center of mass frame. In order to compute the scattering angle in the lab frame, we must use a relationship from the kinematics. From a completely classical analysis of elastic scattering, we get

$$\tan(\theta_L) = \frac{\sin(\theta)}{\alpha + \cos(\theta)}, \quad \alpha = M_i/M_t \tag{3.13}$$

Figure 3.2 is a graphical depiction of this relationship. We see immediately that the lower bound on the scattering cosine in the lab frame when $\alpha > 1$ is

$$\mu_{L,min} = \frac{\sqrt{\alpha^2 - 1}}{\alpha} = \frac{\sqrt{M_i^2 - M_t^2}}{M_i^2} \tag{3.14}$$

Thus, if $M_i >> M_t$, then $\theta_L \approx 0$ for all center of mass scattering angles. Therefore, we see that for protons and heavier particles scattering off electrons with $\alpha \approx 1836$, the angular redistribution is negligible.

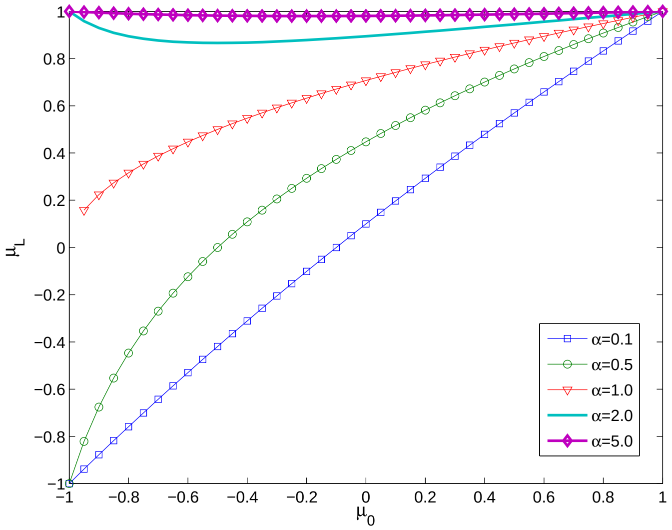

Figure 3.2: Lab frame scattering cosine as a function of the center of mass frame scattering cosine for various $\alpha = M_i/M_t$.

The screened Rutherford cross section can been extended to relativistic energies for particles heavier than electrons by replacing E with βpc. It has been demonstrated that the screened Rutherford DCS is correct at energies above $\approx$ 1 MeV for protons and heavier particles but deviates significantly below this energy[22]. For this research, the energy ranges for which screened Rutherford scattering is correct for these particles will be the only ones considered.

It is well known, however, that electrons scatter by a law that is very different than the screened Rutherford law even at high energies. An approximate DCS given by Mott[16] using Born's approximation is

$$\sigma_{e,M1} = \frac{Z_t Z_i e^2 r_e^2}{4} \left(\frac{m_e c}{\beta p}\right)^2 \frac{1 - \beta^2 \sin^2(\theta/2)}{(\sin^4(\theta/2))} \tag{3.15}$$

This DCS still isn't quite suitable for many problems. An exact solution to the Dirac equation using a partial wave expansion yields an appropriate DCS for electrons scattering off atomic nuclei for a larger range of energies and target nuclei. As this form is very complicated, the Mott DCS is usually written in terms of the screened Rutherford DCS multiplied by a ratio of the two.

$$\sigma_{e,M2}(\mu_0, E) = \sigma_{e,R}(\mu_0, E) f(\mu_0, E) \tag{3.16}$$

$$f(\mu_0, E) = 1 + \frac{Z\beta\pi\alpha}{\sqrt{2}} \cos\gamma (1 - \mu_0 + 2\eta)^{1/2} + h(\mu_0) \tag{3.17}$$

$$\cos\gamma = RE \left[\frac{\Gamma\left(\frac{1}{2} - i\frac{Z_t}{137\beta}\right)\Gamma\left(1 + i\frac{Z_t}{137\beta}\right)}{\Gamma\left(\frac{1}{2} + i\frac{Z_t}{137\beta}\right)\Gamma\left(1 - i\frac{Z_t}{137\beta}\right)} \right] \tag{3.18}$$

The function $h(\mu_0)$ is a tabulated function often approximated by a set of trigonometric interpolants. The ratio $f(\mu_0, E)$ has been tabulated extensively. Figure 3.3 shows this ratio for a few energies for electrons impinging on both lead (bottom) and carbon (top) based on data from Spencer and Doggett[1].

From the figure we see that the largest discrepancy between the Mott and Rutherford DCS is in large angles and for large nuclei. The Mott DCS is still very peaked near $\mu = 1$ suggesting that there is still no relief from the singular behavior of the DCS at small angles. The screened Rutherford cross section will be enough for testing the methods of approximation that will be given in the next few chapters. This DCS embodies all of the difficulties of charged particle transport as many theories only perturb the Rutherford cross section for low energies or for certain scattering ranges. On the other hand, it is simple to analyze making it an ideal test bed for approximation methods.

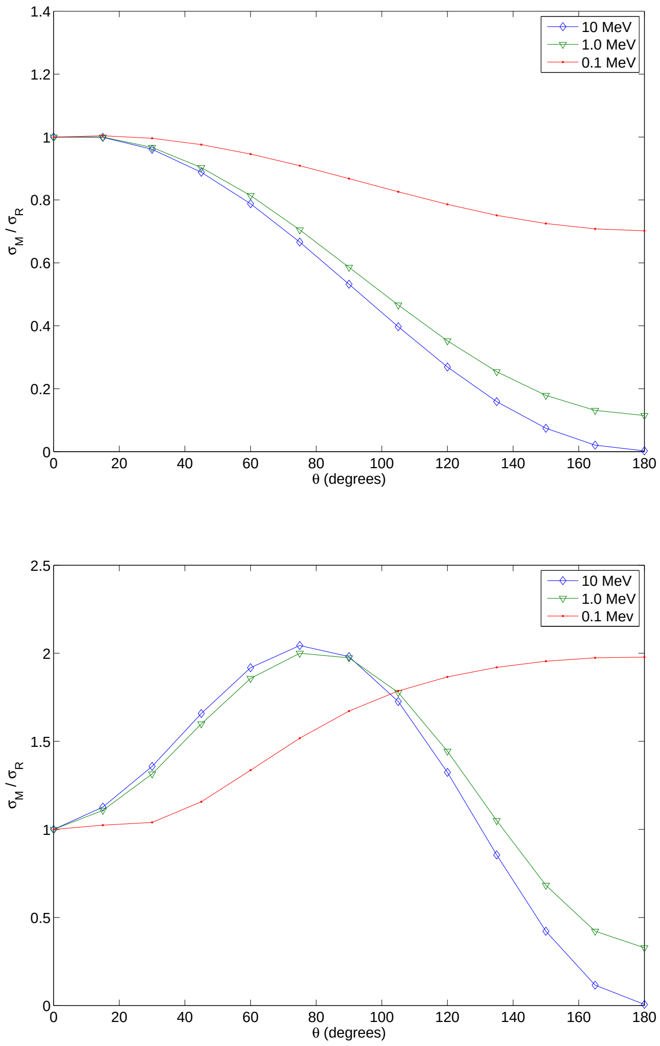

Figure 3.3: Ratio of the Mott DCS σ_M to the Rutherford DCS σ_R for carbon and lead [1].

3.2 Inelastic Scattering of Charged Particles off Atomic Electrons

An incident particle will frequently interact with atomic electrons as it passes through a medium. These collisions are often of such high energies that the electron's binding energy is negligible compared to the energy transferred. In this case, the electron appears to be a free particle, thus greatly simplifying the analysis. Collisions for which this approximation is true are known as hard collisions. When these assumptions are not true, the collisions are considered soft. With soft collisions, an atomic electron must be treated as bound, and energy transfers must be treated as discrete. The resulting relationships are very complicated and very difficult to model. Soft collisions will not be considered further in this thesis. For this reason, ranges will be reported larger and stopping powers smaller for many of the example cases. This discrepancy is known and has no effect on the methods that are being researched.

Hard collisions of charged particles incident on electrons are as simple to model as the elastic collisions in the previous section. We identify the energy lost with

$$Q = \frac{1}{2} m_e v_e^2 = \frac{1}{2} \left(\frac{4 M_r^2 v_i^2}{m_e} \right) \sin^2(\theta/2) \tag{3.19}$$

where M_r is the reduced mass of the system[19]. The differential of this equation becomes

$$dQ = 2 \frac{M_r^2 v_i^2}{m_e} \sin(\theta/2) \cos(\theta/2) d\theta \tag{3.20}$$

We may solve this equation for $\cos(\theta/2) d\theta$ and substitute into Eq.(3.6) to obtain the energy loss DCS $\sigma_{in}(Q, E) \equiv d\sigma_{in}/dQ$.

$$\sigma_{in}(Q, E) = \frac{2\pi Z_t Z_i e^4 r_e^2}{\beta^2} \frac{1}{Q^2} \tag{3.21}$$

Before proceeding further, we discuss an important point about the nature of charged particle transport calculations. We purposely did not elaborate on the energy transferred due to elastic collisions in the previous section because energy losses in collisions with atomic nuclei are negligible when compared to the energy losses to atomic electrons. The proof of this statement is in Eq.(3.21) when an arbitrary mass is placed in the denominator for m_e. We see that electrons carry far more energy away after a collision then a much heavier particle because of its very small mass.

The previous discussion tells us that very little energy is lost in elastic scattering processes with the nucleus when compared to energy lost due to scattering with atomic electrons when the Rutherford DCS is valid. That is, we may neglect energy lost due to elastic scattering processes discussed in the previous section when the incident particle energy is sufficiently high (A_i keV). This will always be true for the research presented here.

Similarly, we see from Eq.(3.14) and Figure 3.2 that the angular redistribution due to inelastic scattering with electrons is negligible. We may simplify the analysis of many processes by exploiting these facts. Whereas in many transport calculations, the energy loss and angular distribution are correlated, this is not so in the case of high energy charged particle transport processes. This fact becomes useful when working with multiple scattering theories, which will be presented in the next chapter. In general, it allows us to more effectively analyze the behavior due to each type of process without regard to the other while still obtaining meaningful results.

A relativistic derivation of Eq.(3.21) with spin effects taken into account leads to a slightly more complicated formula. For heavy incident particles with spin 0, the formula becomes

$$\sigma_{in}(Q,E) = \frac{2\pi Z_t Z_i e^4}{\beta^2}\frac{1}{Q^2}\left(1-\beta^2\frac{Q}{Q_{max}}\right) \tag{3.22}$$

The formula for spin 1/2 particles reduces to Eq.(3.22) at the energy ranges of interest in this thesis[19]. As before, the electron obeys more complicated physics and the DCS for energy loss can be given by the Möller DCS[23]

$$\sigma_{in,M}(Q) = \sigma_{in,R}(Q)\left[1+\frac{Q^2}{(E-Q)^2}+\frac{Q^2}{(E+m_ec^2)^2}+\frac{Qm_ec^2(2E+m_ec^2)}{(E-Q)(E+m_ec^2)^2}\right] \tag{3.23}$$

Again we see that the more accurate DCS can be written as a generalization of the Rutherford DCS $\sigma_{in,R}$ given in Eq.(3.21), much the same as what we've seen with the Mott DCS given in Eq.(3.15).

The maximum energy loss in a single collision is simple to calculate. The general formula for arbitrary particles with mass M striking atomic electrons according to Evans[19] is

$$Q_{max} = E\left[\frac{1 + 2Mc^2/E}{1 + (M + m_e)^2c^2/2m_eE}\right] \tag{3.24}$$

This reduces to the two important special cases

$$2m_ec^2\beta^2\gamma^2 \quad M >> m_e \tag{3.25}$$

$$Q_{max} = E \quad M = m_e \tag{3.26}$$

This corresponds to backscattering in the center of mass frame. These two formulas cover almost all cases since the lightest particle other than electrons that we consider is a proton with $M/m_e \approx 1836$. For electron scattering, the incoming particle is indistinguishable from the target particle so that it is impossible to tell which particle to track for the transport calculation. The standard solution to this problem is to track the higher energy particle, giving a maximum energy loss of

$$Q_{max} = \frac{E}{2}, \quad M = m_e \tag{3.27}$$

The minimum energy transfer in an atomic collision is difficult to evaluate. This is especially the case since we are neglecting soft collisions. One proposed cutoff is the ionization potential given by Turner in electron-Volts[24].

$$Q_{min} = \begin{cases} 19.0 & : \quad Z_t = 1 \\ 11.2 + 11.7Z_t & : \quad 2 \leq Z_t \leq 13 \\ 52.8 + 8.71Z_t & : \quad Z_t > 13 \end{cases} \tag{3.28}$$

Since these energies represent a measure of the average binding energy of atomic electrons, the minimum energy loss for hard collisions cannot be below these values. Soft collisions can have energy losses extending far below the ionization potential leading to a much more highly peaked DCS, just one of the reasons why soft collisions are so difficult to model.

The differential cross sections presented in these sections are sufficient for the purpose of this thesis. Although more complicated cross sections have been found, the forward peaked nature of charged particle transport processes remains. What we mean by this will be explored shortly. For the present, we simply point out that the difficulty in computing solutions to the transport equation with electrons, protons, and heavier ions is completely embodied within the simple formulas given here.

3.3 Transport Equation for Charged Particles

In the absence of electric and magnetic fields and inelastic nuclear interactions (i.e. spallation and fragmentation), the steady state transport equation for a highly collimated monoenergetic beam is

$$\begin{aligned}\Omega \cdot \nabla\psi(\mathbf{r},\Omega,E) = \int_{4\pi} \Sigma_e(\mathbf{r},E,\mu_0)\psi(\mathbf{r},\Omega',E)d\Omega' - \Sigma_{e,t}(\mathbf{r},E)\\ + \int_{Q_{min}}^{Q_{max}} \Sigma_{in}(E,Q)\psi(\mathbf{r},\Omega,E+Q)dQ - \Sigma_{in,t}(\mathbf{r},E) \qquad (3.29)\\ \psi(\mathbf{r}_b,\Omega,E) = \delta(\mathbf{r}-\mathbf{r}_0)\delta(\Omega\cdot\Omega_0 - 1)\delta(E-E_0) \qquad (3.30)\end{aligned}$$

Compare this to Eq.(2.1) where we see that the scattering integral on the right hand side is over both energy and angle. As mentioned earlier, the angular component and the energy component of the scattering decouple due to the physics of charged particle transport. Also, we have an explicit representation for the boundary condition. In many applications, and particularly in medical physics applications, the monoenergetic beam problem is predominant for charged particles. However, one may consider any boundary condition as a sum of monoenergetic beams, and using this form explicitly does not subtract from the generality of the methods presented in the next chapter.

As we are considering the screened Rutherford DCS as sufficient for our investigations for the time being, all elastic scattering kernels σ_e will be for screened Rutherford scattering from Eq.(3.10) and all inelastic scattering kernels σ_{in} will be for Rutherford scattering from Eq.(3.22) unless otherwise noted. We will also use Eq.(3.28) and Eq.(3.26) for Q_{min} and Q_{max} respectively for heavy particles (i.e. protons and larger) and Eq.(3.28) and Eq.(3.27) for electrons. For clarification, we note that the macroscopic cross section given by Σ is related to the microscopic cross section given by σ using the formula

$$\Sigma = \frac{\rho N_A}{A_t}\sigma \tag{3.31}$$

where ρ is the material density, A_t is the atomic number of the particles in the medium and N_A is Avogadro's number.

Thus, our transport problem is fully specified, and a deeper discussion of the scattering kernels is in order. For elastic scattering, the DCS can be written

$$\Sigma_e(\mu_0, E) = \frac{K(E)}{(1 + 2\eta(E) - \mu_0)^2} \tag{3.32}$$

where the energy and particle dependent parameters have been grouped into the variable $K(E)$. Thus we see that there are only two parameters needed to discuss the behavior of this DCS. Figure 3.4 shows the energy dependence of these parameters using their explicit forms given by Eq.(3.10) and Eq.(3.8) and recalling that $\eta(E) = \theta_1(E)^2$. These figures were generated for three different incident particles on tungsten metal. For the electron data, a more accurate form for $\eta(E)$ was used based on the formula of Moliere given in Eq.(3.11). The unitless parameter τ is given by

$$\tau = \frac{E}{M_i c^2} \tag{3.33}$$

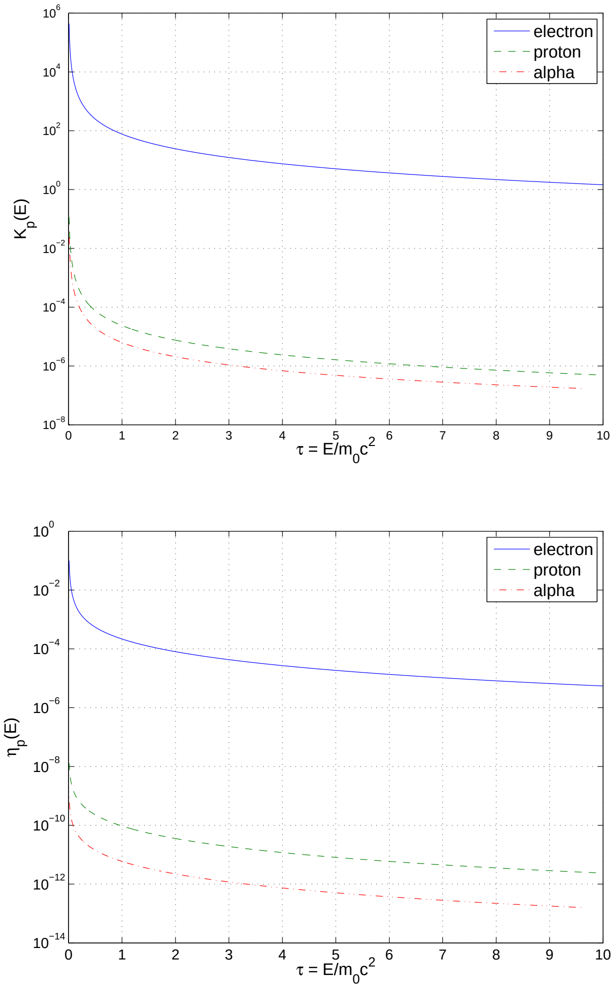

Figure 3.4: Screened Rutherford parameters $K(E)$ and $\eta(E)$ for charged particles on tungsten metal

To see the significance of Fig.(3.4), we consider two important integrals of the DCS. First, the total cross section is given by

$$\Sigma_t(E) = \frac{1}{\overline{\lambda}(E)} = \frac{K(E)}{2\eta(E)(\eta(E)+1)} \tag{3.34}$$

We see that the total cross section, which is the inverse of the mean free path, is unbounded as $\eta \rightarrow 0$. From the figure, we see that this is an important limit for all incident particle types. Furthermore, the dependence on the target particle, not depicted on these plots, is only $O(\rho Z_t/M_t)$ so the change in magnitude of the parameters is typically $O(1)$ for most target particles in many applications.

The other important integral is the transport cross section given by

$$\Sigma_{tr} = \int_{-1}^{1}(1-\mu_0)\Sigma_e(\mu_0,E) = K(E)\left(\ln\frac{\eta(E)+1}{\eta(E)} - \frac{1}{\eta(E)+1}\right) \tag{3.35}$$

This is a measure of the average deviation of the particle from the forward direction per unit distance. In the limit of extremely forward peaked scattering, we can write

$$\begin{aligned}
&\Sigma_{tr} \equiv \Sigma_t\left(\overline{1-\mu_0}\right)\\
&\approx \frac{\left(\overline{1+\mu_0}\right)\left(\overline{1-\mu_0}\right)}{2} = \frac{\left(\overline{1-\cos^2(\theta_0)}\right)}{2} = \frac{\overline{\sin^2(\theta_0)}}{2}\\
&\approx \frac{\overline{\theta_0^2}}{2}
\end{aligned} \tag{3.36}$$

Thus, the transport cross section is approximately equivalent to the mean square angle of scattering. This value is often used in multiple scattering distributions that are used in medical physics codes.

We see that, since the natural log is a slowly varying function, the magnitude of Σ_{tr} is not sensitive to changes in the screening parameter when η is nearly zero. Therefore, we see that the variation in the transport cross section is highly dependent on the parameter $K(E)$. Since this parameter is small for high energy charged particles, the magnitude of Σ_{tr} is very small for all energies of interest. A plot of these two integrals of the DCS are shown in Fig.(3.5).

Many of the arguments just made are completely analogous to the energy loss DCS $\Sigma_{in}(E,Q)$. This is expected since the inelastic DCS is derived from the elastic DCS in the limit of vanishing mass of the target particle. Explicitly, we can make the correspondence $(1-\mu_0+2\eta) \rightarrow Q$ and write the elastic scattering DCS as

$$\Sigma_e(E,Q) = \frac{K(E)}{Q^2} \qquad 2\eta(E) \leq Q \leq 2+2\eta(E) \tag{3.37}$$

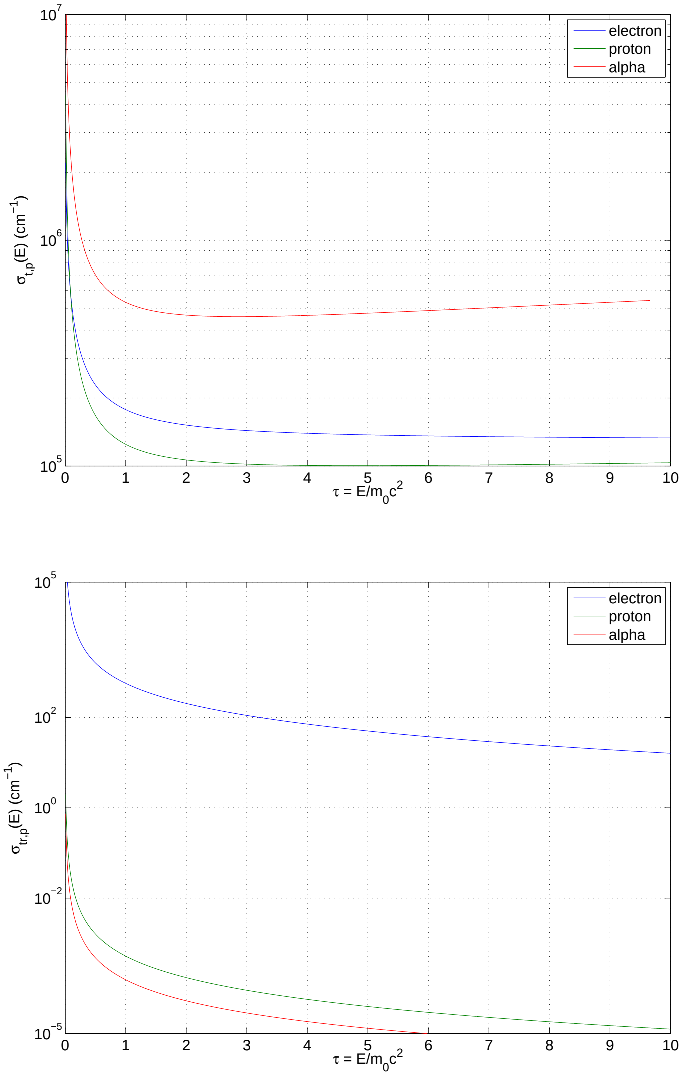

Figure 3.5: Total cross section and transport cross section for particles incident on tungsten metal.

This form is identical to Eq.(3.21) solidifying the belief that the inelastic DCS and elastic DCS have similar behavior. The biggest difference between the two is the magnitude of Q_{min}. In the case of elastic scattering, the effective minimum Q is several orders of magnitude below what is given in Eq.(3.28). This fact will be important when we investigate the moment preserving methods.

It is worth noting that the two important moments of the inelastic DCS are the stopping power $S(E)$ and the straggling parameter $T(E)$.

$$S(E) = \int_{-1}^{1} Q\Sigma_{in}(E,Q)dQ \tag{3.38}$$

$$T(E) = \int_{-1}^{1} Q^2\Sigma_{in}(E,Q)dQ \tag{3.39}$$

The stopping power is completely analogous to the transport cross section. However, it is typically of much larger magnitude then what is depicted in Fig.(3.5) because the multiplicative constant is comparatively larger. The straggling acts as a measure of the spreading of the energy distribution. These two parameters play an important role in the theory of multiple scattering and other approximations.

Figures 3.4 and 3.5 give us intuition as to how ill behaved the cross section can be for high energy particle transport. To see how this affects the solution to the transport equation in Eq.(3.30), we consider the three methods discussed previously. For both the P$_N$ method and the S$_N$ method, we must specify the anisotropic scattering source as a sum over Legendre polynomials.

$$\Sigma_e(E,\mu_0) = \sum_{l=1}^{L} \Sigma_{e,l}(E)P_l(\mu_0) \tag{3.40}$$

$$\Sigma_{e,l}(E) = \int_{-1}^{1} \Sigma_e(E,\mu_0)d\mu_0 \tag{3.41}$$

Figure 3.6 is a comparison of the first four Legendre polynomials and the elastic scattering DCS with $K = 1$ and $\eta = 1 \times 10^{-4}$. Obviously, it is hard to represent the nearly singular DCS on the left with the smooth functions on the right. Therefore, a large expansion order L must be used for these problems. Even at large order, the peaked portion of the DCS leads to overcorrection and oscillatory behavior. It is very difficult to make this behavior disappear completely, even for large order expansions.

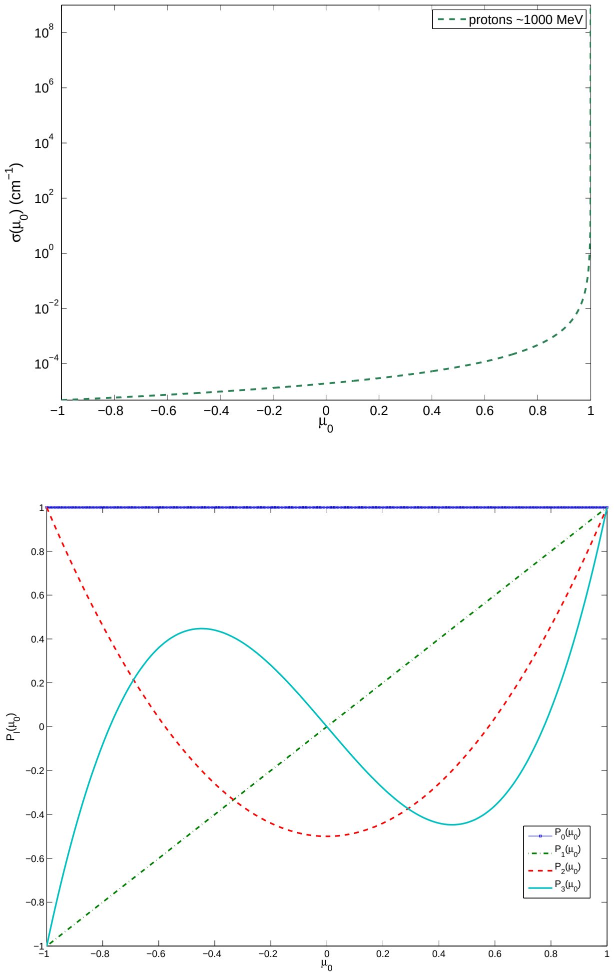

Figure 3.6: Comparison of the elastic scattering DCS given by Rutherford to the first four Legendre polynomials

A problem we see specifically with the discrete ordinates method is the problem with ray effects. We mentioned this briefly in the first chapter as artifacts appearing in the spatial solution as a result of solving the problem only along discrete rays. For this particular transport problem, the number of rays required to eliminate ray effects is much higher than in neutral particle transport problems because of the many small angle scatters required to get the large deviations macroscopically. Also, a very fine spatial grid would be needed to maintain positivity with many of the discretization schemes that are used in solving the S$_N$ equations. The P$_N$ equations become far too numerous to be solved efficiently when using the analog DCS given in this chapter also. In addition, a singular boundary condition poses a difficulty in P$_N$ methods since we only have half as many unknowns as boundary conditions to satisfy. Approximating a delta function with only half of the basis functions of the angular domain becomes impossible even in principle.

The Monte Carlo suffers from difficulties as well. While the difficulties are not numerical like we saw with S$_N$ and P$_N$ methods, the underlying problem is still an exhaustion of computing resources. Consider Eq.(2.22) with $\overline{\lambda}$ given by Eq.(3.34). We see that the mean free path is $O(\eta/K)$ which is typically $O(10^{-4})-O(10^{-7})$. For a problem domain where the length scales are $O(1)$ in the same units, we will have $O(10^4)-O(10^7)$ collisions per particle.

Suppose we required 10^7 collisions to simulate one particle in a given problem. Typically, about a million particle trajectories are needed to get a low statistical error. Even if we could process a collision with a single floating point operation, we would need about 10^{13} floating point operations to complete the calculation. A typical processor can do about 10^9 floating point operations per second so about 3 hours is required to finish the problem.

To make matters worse, we have the basic result from the central limit theorem concerning the convergence of the mean of a finite sample to the true mean of a population.

$$\frac{\epsilon_n}{\epsilon_N}=\frac{\mu-\overline{x}_n}{\mu-\overline{x}_N}=\sqrt{\frac{N}{n}} \tag{3.42}$$

This means that statistical errors in Monte Carlo calculations, where we are using a finite number of samples to approximate the true mean, converges slowly with the number of samples. Thus, if one wanted to get a factor 10 increase in accuracy, they would need to simulate 100 times as many particles. From the above discussion, this could make a 3 hour runtime turn into a 12.5 day calculation. This is completely unacceptable from a design standpoint, where hundreds or thousands of these calculations are required.

3.4 Characterizing a "Forward Peaked" Differential Cross Section

Many of the difficulties identified in the previous section have been addressed in other contexts. For instance, the diffusion equation arises when one needs to treat small mean free paths in neutron transport theory. However, since the diffusion equation is derived from a P_1 approximation, it is essential that the angular flux and scattering kernels are nearly isotropic. Treating charged particle transport processes with a continuum description is a very difficult problem. We will attempt to identify the additional difficulties before proceeding with the different approximations. The knowledge gained here will aid us in explaining the results obtained in the next few chapters.

Rather than working with the DCS itself, it will be more transparent if we use the distribution function defined by

$$p(\mu_0) \equiv \frac{\Sigma_e(\mu_0)}{\Sigma_{e,t}} = \frac{\eta(\eta+1)}{(1+2\eta-\mu_0)^2} \tag{3.43}$$

From this we identify other key properties of the physics. For instance, we can get the average cosine of scattering

$$\overline{\mu}_0 = \int_{-1}^{1} \mu_0 p(\mu_0) d\mu_0 = 2\eta(\eta+1)\ln\frac{\eta}{\eta+1} + 2\eta + 1 \tag{3.44}$$

or sometimes it is more beneficial to have the average deviation of μ_0 from 1 given by

$$\overline{1-\mu_0} = 1 - \overline{\mu}_0 = 2\eta(\eta+1)\ln\frac{\eta+1}{\eta} - 2\eta \tag{3.45}$$

From this we see explicitly that the scattering cosine is just under unity for very small η. This is one way of characterizing the forward peaked nature of the DCS. However, it doesn't tell the whole story. For instance, we may ask why not treat all problems below a certain threshold in η as straight-ahead. More appropriately, why not treat the elastic scattering as a process that happens continuously at a certain average rate.

In fact, both of these methods have been developed over the years and are in many cases the state of the art in high energy charged particle transport. However, it is well known that there is still significant deviation between a solution that accounts only for the average scattering and the exact solution to the problem[25]. There have been various explanations of this phenomena and only a few that put it into mathematical terms. In each explanation, the underlying theme is that the "occasional" large angle scattering cannot be neglected, but there is seldom a transparent formalism that supports this claim.

To study this claim, we consider an ensemble of particles which scatter by a process that has a fixed, small but non-zero mean free path λ. Furthermore, they redistribute in polar angle $\theta = \cos^{-1}(\mu_0)$ according to Eq.(3.43) and in azimuthal angle ϕ uniformly. We would like to know the probability that a particle has had an event with $\mu_0 < \mu^*$ where we define this reference by

$$p(\mu_0 < \mu^*) = \int_{-1}^{\mu^*} p(\mu_0)d\mu_0 = p \tag{3.46}$$

$$p = \frac{2\eta(1+\eta)}{1-\mu^*+2\eta} - \eta \tag{3.47}$$

with p chosen to be arbitrarily small. Then we have a binary outcome space and the probability of n scattering events with $\mu_0 < \mu^*$ in m collisions follows a binomial distribution.

$$P(n|m) = \frac{m!}{n!(m-n)!}p^n(1-p)^{m-n} \tag{3.48}$$

Since the transport process is Markovian, and since we know the mean number of collisions per unit distance Σ_t, we may express the probability of having m collisions in distance z using a Poisson distribution.

$$G(m|z) = \frac{(\Sigma_t z)^m \exp(\Sigma_t z)}{m!} \tag{3.49}$$

Therefore, the probability of having exactly n collisions with $\mu_0 < \mu^*$ in distance z becomes

$$\begin{aligned} H(n|z) &= \sum_{m=n}^{\infty} P(n|m)G(m|z) \\ &= \frac{\exp(-\Sigma_t z)p^n}{n!} \sum_{m=n}^{\infty} \frac{(\Sigma_t z)^m (1-p)^{m-n}}{(m-n)!} \\ &= \frac{(\Sigma_t z p)^n \exp(-\Sigma_t z)}{n!} \sum_{m=0}^{\infty} \frac{[\Sigma_t z(1-p)]^m}{m!} \\ &= \frac{(\Sigma_t z p)^n}{n!} \exp(-\Sigma_t z p) \end{aligned} \tag{3.50}$$

This gives the probability density function for the number of events n at a distance z. However, we would like the probability of $n \geq 1$ collisions occurring with $\mu_0 < \mu^*$. This is given by summing over the probability density $H(n|z)$.

$$\begin{aligned} H(n \geq 1|z) = \sum_{n=1}^{\infty} H(n|z) &= \sum_{n=1}^{\infty} \frac{(\Sigma_t z p)^n}{n!} \exp(-p\Sigma_t z) \\ &= 1 - \exp(-p\Sigma_t z) \end{aligned} \tag{3.51}$$

We see that this probability exponentially approaches unity for arbitrarily small but fixed p. This is a direct result of the very small mean free path. Thus, the occasional collisions only become important because of the very large number of collisions. To put this in perspective, we have plotted $H(n \geq 1|z)$ for 1700 MeV protons incident on tungsten metal for various $\theta^* = \cos^{-1}(\mu^*)$ in Fig.(3.7). In this problem, $\eta = 4.0 \times 10^{-11}$ and $\Sigma_t = 2.2 \times 10^5$. We see that relatively large angle scatters have a high probability of occurring within distances comparable to the proton range in tungsten at 1700 MeV ($\approx$ 130 cm). This of course assumes that the parameters stay fixed over the range. However, the particles slow down as they penetrate a medium and the parameters will adjust in favor of more scattering and larger scattering angles. Figure 3.8 shows how the probability varies for the three scattering angles in Fig.(3.7) with decreasing energies. This is very similar to how Σ_t varies in Fig.(3.5). From these two plots, we see that in fact the probability of a scattering event with $\mu_0 < \mu^*$ approaches unity much faster than exponentially as the particle penetrates a medium due to the effect of slowing down on the mean number of collisions and the probability of large angle scatter.

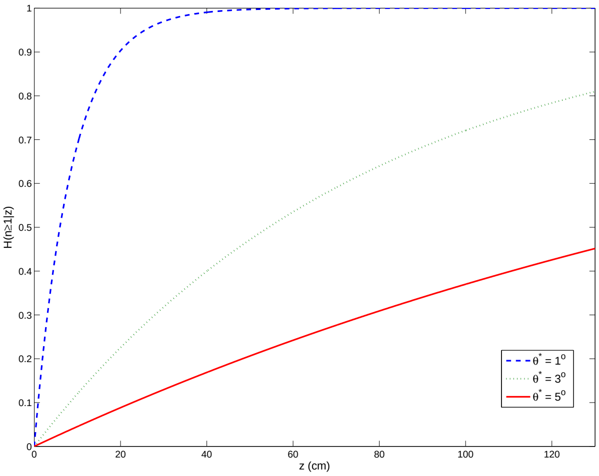

Figure 3.7: Probability of a particle having at least on scattering event with $\theta > \theta^*$ for 1700 MeV protons incident on tungsten metal.

From the arguments presented here, it seems that there is no hope of capturing the behavior of high energy charged particles with simple continuum descriptions.

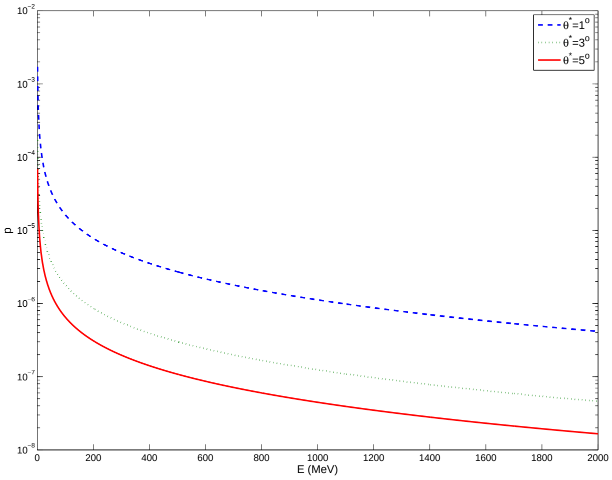

Figure 3.8: Variation of the probability p for fixed μ^* for the relatively large angle scatters and problem specification given in Fig.(3.7)

These descriptions necessarily preserve only average behavior, but we've seen that the small probability events will necessarily take place at random points within the medium. These small probability events will have a large effect on the solution because they tend to push energy and charge to other points within the medium. Again, there are similar arguments to be made for the energy redistribution kernel. In that case, the small probability events tend to deposit large amounts of energy at random points in the medium. Once again, this important outcome cannot be captured with a simple averaging of the behavior in a continuum.

These facts were recognized early on in high energy charged particle transport research. However, computing resources were even more scarce when these problems were discovered than at present. For this reason, researchers had to settle for approximation schemes that were known to be faulty so that some solution could be found to their problems. Unfortunately, little progress has been made to replace these older algorithms. Comparatively more effort has been made in fixing the methods to work better for specific problems. For this reason, a brief discussion of the older methods must precede the developments made during this research.

Chapter 4

Fokker-Planck and Fermi Approximations

We will investigate the most widely used approximations for charged particle transport processes in this chapter. Much of what is presented here is a very brief summary of a very large body of work that started in the early twentieth century. Emphasis will be placed on the aspects of the theories that was addressed in the research done for this thesis. These include theoretical indications of when these methods fail and experimental verification of their failure.

As in the previous chapter, we note that all elastic scattering theories are based on the screened Rutherford DCS except when specifically noted otherwise. Also, Σ_e represents the macroscopic elastic cross section and Σ_{in} represents the macroscopic inelastic cross section. More emphasis will be placed on elastic scattering since it poses the same challenges as inelastic scattering but adds additional challenges of its own. The differences are elaborated in the first few sections and general results for inelastic scattering will be given in future chapters. To keep the arguments simple and clear, all of the theories for elastic scattering will be presented for the special case of monoenergetic particles.

4.1 Notes on the Transport Cross Section

Before delving into the approximations of high energy charged particle transport, a brief discussion of the parameter Σ_{tr} given by Eq.(3.35) is needed. This parameter shows up often in the theories that were researched because it is synonymous to the stopping power given in Eq.(3.38). The stopping power has an obvious physical interpretation; it is the average amount of energy lost by a particle per unit of distance traversed. Continuous slowing down algorithms rely on the stopping power to handle particle energy dependence deterministically.

The physical interpretation of Σ_{tr} is more difficult to visualize. It can be thought of as an average increase in deviation of the cosine of the particles direction from the original forward direction per unit distance. However abstract this may seem, it follows the same intuition as that followed in interpreting the stopping power. On the other hand, it is not immediately clear that this quantity is even useful at all. The particle energy is monotonically decreasing on the real line ideally from some maximum energy to zero. The randomness is only in how much energy is lost in the discrete collisions that occur within an interval of distance. The particle direction, however, follows a random walk on the unit sphere[26].

To see why this parameter is useful, we consider an arbitrary scattering law with transport cross section Σ_{tr}. Azimuthal angles of scattering are uniformly distributed in the interval $[0, 2\pi)$. Each scattering event generates the two parameters μ_0 and ϕ. For simplicity, the scattering angles are all chosen with respect to the particle's local z-axis. The transformation of a particle's trajectory in the fixed frame using these angles and assuming that the center of mass frame is the same as the lab frame is given by

$$u' = \mu_0 u + \frac{\sqrt{1-\mu_0^2}}{\sqrt{1-w^2}}(uw\cos\phi - v\sin\phi) \tag{4.1}$$

$$v' = \mu_0 v + \frac{\sqrt{1-\mu_0^2}}{\sqrt{1-w^2}}(vw\cos\phi + u\sin\phi) \tag{4.2}$$

$$w' = \mu_0 w + \sqrt{1-\mu_0^2}\sqrt{1-w^2}\cos\phi \tag{4.3}$$

To simplify the following analysis, we consider a problem where all particles have the initial trajectory given by $(u, v, w) = (0, 0, 1)$. Any other problem can be considered as an integrated source over such incident beams with a global change of coordinates. Thus, the analysis here remains valid for the general case.

We wish to know what the average z-component of a particle's trajectory is after moving a distance s in a material. The distance s is not the same as the z-coordinate of the particle. This matter is given separate consideration in many multiple scattering theories. For the present problem, we seek the intermediate result: what is the average z-component of scattering of a particle who has had n collisions with the $2n$ random variables (μ_1, ϕ_1), (μ_2, ϕ_2), ... (μ_n, ϕ_n) to describe the scattering of the particle into states with z-component of the trajectory equal to $w^{(1)}$, $w^{(2)}$, ... $w^{(n)}$ respectively. We shall prove by induction that the answer is $\overline{w}^{(n)} = \overline{\mu}_0^n$ with

$$\overline{\mu}_0 = \int_{-1}^{1} \mu_0 P(\mu_0) d\mu_0 = \int_{-1}^{1} \mu_0 \frac{\Sigma_e(\mu_0)}{\Sigma_{t,e}} d\mu_0. \tag{4.4}$$

By Eq.(4.3), the states can be recursively computed with

$$w^{(k)} = \mu_k w^{(k-1)} + \sqrt{1-\mu_k^2}\sqrt{1-(w^{(k-1)})^2}\cos\phi_k. \tag{4.5}$$

given the random variables μ_k and ϕ_k. The distribution function for a given state k will be written $P_k(w^{(k)})$ and is not known a priori for $k > 0$. For $k = 0$, the distribution is given by $P_0(w^{(0)}) = \delta(w^{(0)} - 1)$ by definition of the problem. The base case is simple to compute.

$$\begin{aligned}\overline{w}^{(1)} &= \int_0^{2\pi} d\phi_1 \int_{-1}^{1} d\mu_1 \int_{-1}^{1} dw^{(0)} P_0(w^{(0)}) P(\mu_1) P'(\phi_1) \\ &\quad \times \left[\mu_1 w^{(0)} + \sqrt{1-\mu_1^2}\sqrt{1-(w^{(0)})^2}\cos\phi_1\right] \\ &= \int_0^{2\pi} d\phi_1 P'(\phi_1) \int_{-1}^{1} d\mu_1 \mu_1 P(\mu_1) \\ &= \overline{\mu}_0 \end{aligned} \tag{4.6}$$

The induction hypothesis can be written explicitly

$$\overline{\mu}_0^{n-1} = \overline{w}^{(n-1)} = \int_{-1}^{1} dw^{(n-1)} w^{(n-1)} P_{n-1}(w^{(n-1)}) \tag{4.7}$$

To compute the average of $w^{(n)}$ we have

$$\begin{aligned}\overline{w}^{(n)} &= \int_0^{2\pi} d\phi_n \int_{-1}^{1} d\mu_n \int_{-1}^{1} dw^{(n-1)} P_{n-1}(w^{(n-1)}) P(\mu_n) P'(\phi_n) \\ &\quad \times \left[\mu_n w^{(n-1)} + \sqrt{1-\mu_n^2}\sqrt{1-(w^{(n-1)})^2}\cos\phi_n\right] \\ &= \int_{-1}^{1} d\mu_n \mu_n P(\mu_n) \int_{-1}^{1} dw^{(n-1)} w^{(n-1)} P_{n-1}(w^{(n-1)}) + \underbrace{\left[\int_0^{2\pi} d\phi_n P'(\phi_n)\cos\phi_n\right]}_{=0} \\ &\quad \times \int_{-1}^{1} d\mu_n P(\mu_n)\sqrt{1-\mu_n^2} \int_{-1}^{1} dw^{(n-1)} P_{n-1}(w^{(n-1)})\sqrt{1-(w^{(n-1)})^2} \\ &= \overline{\mu}_0 \overline{w}^{(n-1)} \;=\; \overline{\mu}_0^n \end{aligned} \tag{4.8}$$

We also have as a corollary to this result that $1 - \overline{w}^{(n)} = 1 - \overline{\mu}_0^n$. This gives the average "accumulation" of $1 - \mu_0$ for a set number of collisions. To get the average after distance s, we fold the previous result with the Poisson distribution which gives the distribution of the number of collisions n for a given average collision "rate" Σ_t.

$$\begin{aligned}\overline{1-w} &= \sum_{n=0}^{\infty}(1-\overline{\mu}_0^n)\frac{(\Sigma_t s)^n \exp(-\Sigma_t s)}{n!} \\ &= 1 - \exp[-\Sigma_t s(1-\overline{\mu}_0)] \end{aligned} \tag{4.9}$$

By definition we have $\Sigma_{tr} \equiv \Sigma_t(1-\overline{\mu}_0)$. Substituting this identity into Eq.(4.9) gives

$$\overline{1-w} = 1 - \exp(-\Sigma_{tr} s) \tag{4.10}$$

This is independent of the details of the scattering law including the azimuthal angle dependence and the complicated transformation from local to global reference frames. The interpretation from this analysis is that any two DCSs with the same transport cross section will have the same average deviation from the forward direction. Furthermore, when $\Sigma_{tr} s$ is small, the expression in Eq.(4.10) simplifies to

$$\overline{1-w} \approx 1 - (1 - \Sigma_{tr} s) = \frac{s(\overline{1-\mu_0})}{\overline{\lambda}} = \overline{N}_c(s)(\overline{1-\mu_0}) \tag{4.11}$$

where the average number of collisions in distance s, $\overline{N}_c(s)$, has been introduced. Therefore, the average deviation from the forward direction tends to accumulate with each collision in this limit, much like energy loss accumulates in the inelastic scattering formalism. The difference is that this limit will not hold for large penetration depths, and the average accumulation asymptotically approaches zero for elastic scattering.

4.2 The Fokker-Planck Operator

The Fokker-Planck approximation is the most widely used continuum description of high energy charged particle transport. It is also the basis for other more sophisticated approximations. The Fokker-Planck approximation represents an asymptotic equivalence of the Boltzmann scattering operator and the spherical Laplacian operator. We give a brief summary of its derivation here which follows the work of Larsen and Leakes[27]. A more rigorous derivation is given by Pomraning[28].

4.2.1 Derivation of the Fokker-Planck Operator for Forward-Peaked Transport

Recall that the elastic scattering DCS can be expanded as a series of spherical harmonics,

$$\Sigma_e(\mu_0) = \sum_{l=0}^{\infty} \Sigma_{e,l} \sum_{m=-l}^{l} Y_l^m(\Omega) Y_l^{*m}(\Omega') \tag{4.12}$$

$$\Sigma_{e,l} = 2\pi \int_{-1}^{1} \Sigma_e(\mu_0) P_l(\mu_0) d\mu_0 \tag{4.13}$$

and the Boltzmann scattering operator given by

$$L_B\psi(\Omega) = \int_{4\pi} \Sigma_e(\mu_0)\psi(\Omega')d\Omega' - \Sigma_{e,0}\psi(\Omega) \tag{4.14}$$

where

$$\psi(\Omega) = \sum_{l=0}^{\infty} \sum_{m=-l}^{l} \psi_{lm} Y_l^m(\Omega) \tag{4.15}$$

can also be expanded in spherical harmonics,

$$L_B\psi(\Omega) = \sum_{l=0}^{\infty} (\Sigma_{e,l} - \Sigma_{e,0}) \sum_{m=-l}^{l} \psi_{lm} Y_l^m(\Omega) \tag{4.16}$$

For high energy charged particles, we can assume that $\Sigma_e(\mu_0)$ is peaked near 1, thus allowing a Taylor expansion of the Legendre polynomials in Eq.(4.13) about $\mu_0 = 1$. That is,

$$\begin{aligned} \Sigma_{e,l}(\mu_0) &= \int_{-1}^{1} d\mu_0 \Sigma_e(\mu_0) \left[P_l(1) + (\mu_0 - 1)P_l'(1) + O\left((1-\mu_0)^2\right)\right] \\ &= \Sigma_{e,t}P_l(1) - \Sigma_{tr}P_l'(1) + O\left(\Sigma_{e,t}\overline{(1-\mu_0)^2}\right) \end{aligned} \tag{4.17}$$

From the basic properties of Legendre polynomials, we have $P_l(1) = 1$ and $P_l'(1) = l(l+1)/2$. Substituting these identities into Eq.(4.17) and substituting that into

Eq.(4.16) gives

$$L_B\psi(\Omega) = \frac{\Sigma_{tr}}{2}\sum_{l=0}^{\infty} -l(l+1)\sum_{m=-l}^{l}\psi_{lm}Y_l^m(\Omega) + O\left(\Sigma_{e,t}\overline{(1-\mu_0)^2}\right) \tag{4.18}$$

The spherical harmonics are also eigenvalues of the spherical Laplacian operator, also known as the angular momentum operator in physics applications. This operator satisfies the eigenvalue equation

$$\nabla_\Omega^2 Y_l^m(\Omega) = -l(l+1)Y_l^m(\Omega) \tag{4.19}$$

This allows us to write

$$\begin{aligned} L_B\psi(\Omega) \quad &= \frac{\Sigma_{tr}}{2}\sum_{l=0}^{\infty}\sum_{m=-l}^{l}\psi_{lm}\nabla_\Omega^2 Y_l^m(\Omega) + O\left(\Sigma_{e,t}\overline{(1-\mu_0)^2}\right) \\ &= \frac{\Sigma_{tr}}{2}\nabla_\Omega^2\left(\sum_{l=0}^{\infty}\sum_{m=-l}^{l}\psi_{lm}Y_l^m(\Omega)\right) + O\left(\Sigma_{e,t}\overline{(1-\mu_0)^2}\right) \\ &= \frac{\Sigma_{tr}}{2}\nabla_\Omega^2\psi(\Omega) + O\left(\Sigma_{e,t}\overline{(1-\mu_0)^2}\right) \end{aligned} \tag{4.20}$$

Thus we see that, to leading order, the Boltzmann operator is equivalent to a spherical Laplacian when scattering is sufficiently forward peaked. That is,

$$\begin{aligned} L_B\psi(\Omega) &\longrightarrow \frac{\Sigma_{tr}}{2}\nabla_\Omega^2\psi(\Omega) \\ = \frac{\Sigma_{tr}}{2}&\left[\frac{\partial}{\partial\mu}(1-\mu^2)\frac{\partial\psi}{\partial\mu} + \frac{1}{1-\mu^2}\frac{\partial^2\psi}{\partial\phi^2}\right] \end{aligned} \tag{4.21}$$

as $\overline{\mu}_0 \rightarrow 1$ and $\Sigma_{e,t} \rightarrow \infty$ such that $\Sigma_{tr} \equiv \Sigma_{e,t}(1-\overline{\mu}_0)$ remains finite.

The value of this approximation is immediately clear. We transform an integro-differential equation into a partial differential equation which is much easier to solve. The Fokker-Planck approximation for inelastic scattering has an analogous derivation and can be written as

$$\int_{-1}^{1}\Sigma_{in}(E,Q)\psi(E+Q)dQ = \frac{\partial}{\partial E}[S(E)\psi(E)] + \frac{1}{2}\frac{\partial^2}{\partial E^2}[T(E)\psi(E)] + O(Q^3) \tag{4.22}$$

The interpretation is that angular spreading happens at a continuous rate given by Σ_{tr} on the unit sphere and that energy loss happens at a constant average rate $S(E)$ with a deterministic straggling of energies determined by $T(E)$. We see now explicitly the fundamental differences in the interpretations needed for energy loss and angular spreading of beams.

4.2.2 Accuracy of the Fokker-Planck Approximation

The caveat to the Fokker-Planck approximation is that it is a weak equivalence. For the scattering to be sufficiently forward-peaked, we require that higher moments given by

$$\Sigma_{e,n} = \int_{-1}^{1} (1 - \mu_0)^n \Sigma_e(\mu_0) d\mu_0 \tag{4.23}$$

$$\Sigma_{in,m} = \int_{Q_{min}}^{Q_{max}} Q^m \Sigma_{in}(Q) dQ \tag{4.24}$$

are vanishingly small for $n > 1$ and $m > 2$. However, this is not the case for differential cross sections of the Rutherford type. Figure 4.1 shows how the magnitudes of the moments of both the inelastic and the elastic scattering cross sections vary with increasing n for protons incident on tungsten metal at various energies. We see in Fig.(4.1) that the moments may initially decrease with n but they will eventually start increasing at some sufficiently large value of n.

Individual moments tend to stabilize asymptotically at high energies. Figure 4.2 is a plot of the first four moments of both the inelastic and the elastic scattering DCS for protons incident on tungsten. We see that the magnitudes of the moments maintain a nearly constant separation at higher energies. Also, they change relatively little in the range between about 100 and 1000 MeV. Therefore, the criterion that the moments fall off very rapidly seems to go unsatisfied for this case. Also, this

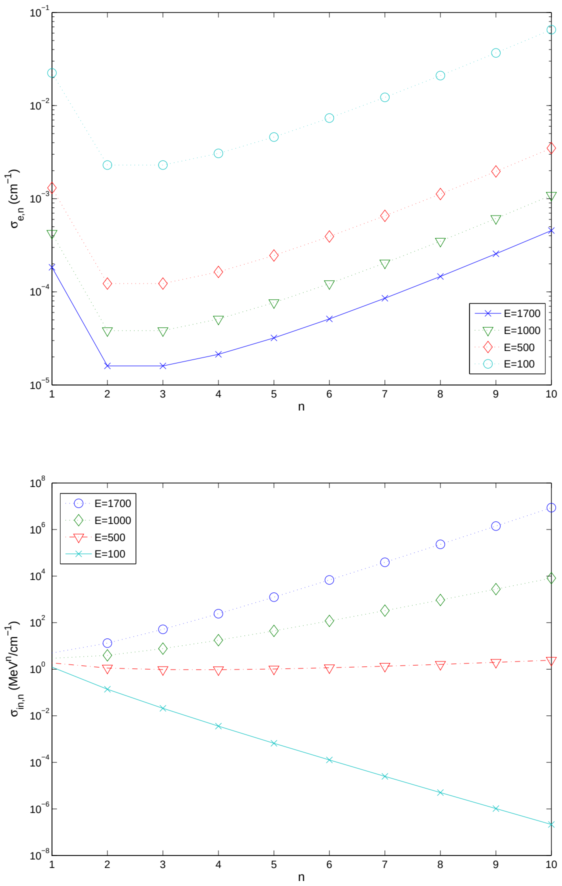

Figure 4.1: Moments of the elastic and inelastic DCS for protons incident on tungsten at various energies.

example provides a good indication of a more general trend for all high energy charged particles since the form of the DCS remains nearly the same.

We have seen that the criteria for the validity of the Fokker-Planck approximation are not necessarily met in applications. However, it is still not clear that the error is significant from this analysis. Indeed the approximations made in deriving the Fokker-Planck approximation seemed plausible. However, the following analysis drives out any doubt that the Fokker-Planck approximation, by itself at least, is not good enough for simulating high energy charged particles.

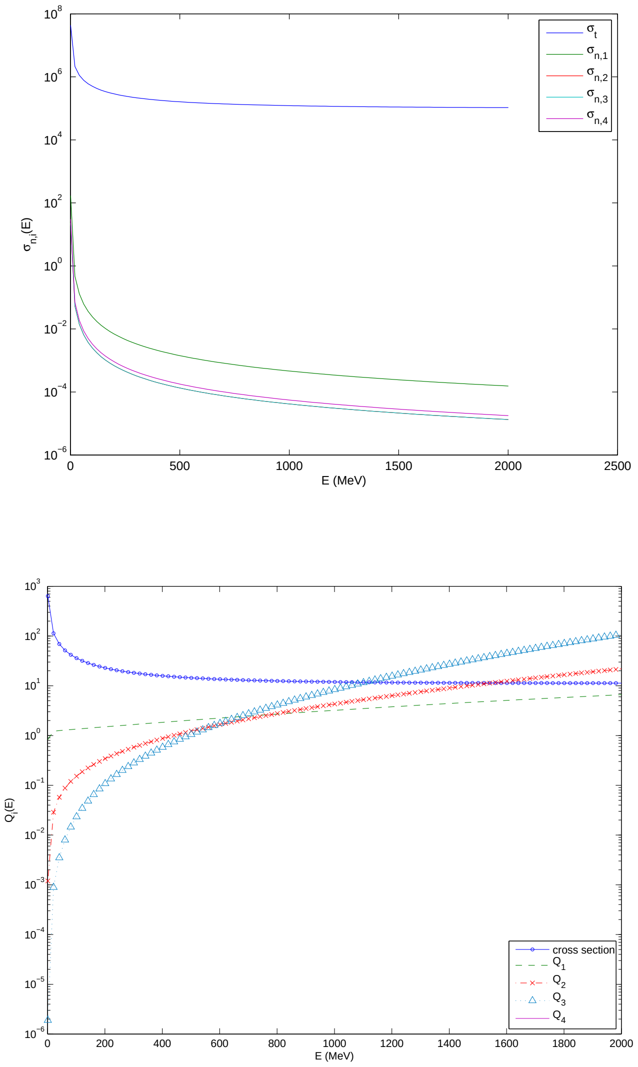

Figure 4.2: Energy dependence of the first four moments and the total cross section of the elastic and inelastic DCS for protons incident on tungsten.

Larsen and Börgers showed that screened Rutherford scattering and Mott scattering lie on the verge of validity of the Fokker-Planck approximation[25]. In their analysis, they identified the condition which must be satisfied by any differential cross section that is to be approximated by the Fokker-Planck operator.

$$\lim_{\overline{\mu}_0 \to 1} \frac{\mathrm{var}(\mu_0)}{1-\overline{\mu}_0} = 0 \tag{4.25}$$

This is equivalent to

$$\lim_{\overline{\mu}_0 \to 1} \frac{\Sigma_2}{\Sigma_1} = 0 \tag{4.26}$$

The latter condition could have been deduced from the analysis already done. However, the technique used by Larsen and Börgers explcitly gives the leading order error generated by using the Fokker-Planck operator. This solidifies our earlier analysis.

The condition of Larsen and Börgers is not automatically satisfied for scattering kernels whose value is peaked near unity. In fact, they showed that

$$\int_{-1}^{1} \frac{C(\alpha,\eta)\psi(\Omega)}{(1+2\eta-\mu_0)^{\alpha}} d\mu_0 - \Sigma_t \psi(\Omega) \xrightarrow{\overline{\mu}_0 \to 1} \frac{\Sigma_{tr}}{2} \nabla^2_{\Omega} \psi(\Omega) \text{ if and only if } \alpha \geq 2 \tag{4.27}$$

Therefore, we would expect that screened Rutherford scattering converges very slowly to a Fokker-Planck description. We see that this is true using their explicit formula for screened Rutherford scattering.

$$\frac{\mathrm{var}(\mu_0)}{1-\overline{\mu}_0} = \frac{-2}{\ln(1-\overline{\mu}_0)} + O\left(\frac{1}{\ln(1-\overline{\mu}_0)^2}\right) \tag{4.28}$$

Figure 4.3 shows graphically how the leading order error trends with $1-\overline{\mu}_0$. We see that the leading order error term tends toward zero logarithmically slowly. This analysis is independent of particle type and thus holds for electrons and ions alike. The only difference is that a typical value for $1-\overline{\mu}_0$ for electrons is $10^{-3} - 10^{-5}$ while for protons and alphas it is $10^{-8} - 10^{-10}$. There is a tendency to assume that this "super forward-peaked" behavior for heavier charged particles makes the Fokker-Planck model more accurate for ion transport applications. However, from Fig.(4.3) we see that there is essentially no difference in the leading order error term in this range of values of Σ_{tr}.

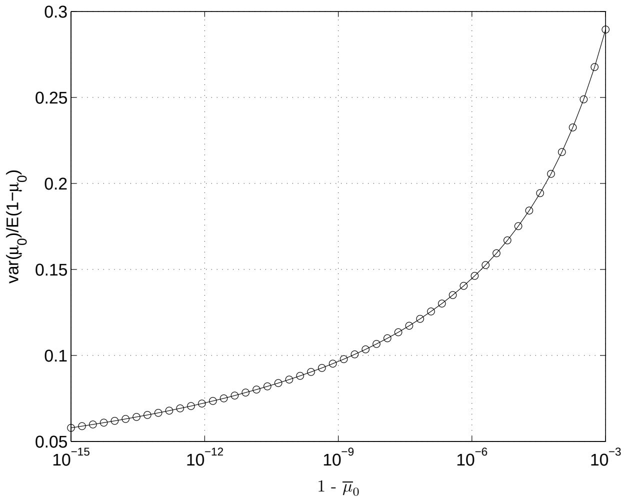

Figure 4.3: Leading order term for the error in using a Fokker-Planck approximation in place of screened Rutherford scattering.

4.2.3 Delta Function Representation of the Fokker-Planck Operator

We still have not seen the true error in using the Fokker-Planck approximation. Instead we have seen how slowly the error tends to zero as $\overline{\mu}_0 \to 1$ which is a fixed parameter due to the physics. In order to study the error due to the Fokker-Planck approximation, we need a way to simulate a Fokker-Planck scattering operator using Monte Carlo methods. Of course, the Fokker-Planck operator can be easily implemented into a deterministic framework, but the comparison with an analog Monte Carlo scheme would not be as transparent. Therefore, we introduce a representation of the Fokker-Planck operator using deterministic scattering angles[25].

$$\frac{\Sigma_{tr}}{2}\nabla^2_{\Omega}\psi(\Omega) = \lim_{\mu^*\to 1} L^*\psi(\Omega)$$

$$\equiv \lim_{\mu^*\to 1} \frac{\Sigma_{tr}}{2\pi(1-\mu^*)}\left(\int_0^{2\pi} d\phi \int_{-1}^{1} d\mu\,\delta(\mu-\mu^*)\psi(\Omega) - 2\pi\psi(\Omega)\right) \tag{4.29}$$

This equivalence can be shown easily if we recognize that L^* is an operator in the same form as the Boltzmann operator. Then we know that L^* has a complete set of eigenfunctions in $Y_l^m(\Omega)$ and the eigenvalue equation becomes

$$L^*Y_l^m(\Omega) = (\Sigma^*_{e,l} - \Sigma^*_{e,0})Y_l^m(\Omega) \equiv \lambda_l Y_l^m(\Omega) \tag{4.30}$$

$$\Sigma^*_{e,l} = \frac{\Sigma_{tr}}{1-\mu^*}\int_{-1}^{1} d\mu P_l(\mu)\delta(\mu-\mu^*) = \Sigma_{e,0}P_l(\mu^*) \tag{4.31}$$

Then, taking the limit, using L'Hospital's rule, and recognizing that $P_l'(1) = l(l+1)/2$, we obtain

$$\begin{aligned} \lim_{\mu^*\to 1} L^*Y_l^m(\Omega) &= \lim_{\mu^*\to 1} \frac{P_l(\mu^*)-1}{1-\mu^*}\Sigma_{tr}Y_l^m(\Omega) \\ &= -\frac{\Sigma_{tr}}{2}l(l+1)Y_l^m(\Omega) \;=\; \frac{\Sigma_{tr}}{2}\nabla^2_\Omega Y_l^m(\Omega) \end{aligned} \tag{4.32}$$

Therefore, these two operators are equivalent since they have the same eigenvalues and eigenvectors. Furthermore, we may quantify the error by expanding

$$P_l(\mu^*) = 1 - \frac{l(l+1)}{2}(1-\mu^*) + \frac{l(l+1)(l+2)(l-1)}{16}(1-\mu^*)^2 + O\left((1-\mu^*)^3\right) \tag{4.33}$$

Substituting Eq.(4.33) into Eq.(4.32) without taking the limit we obtain

$$L^*Y_l^m(\Omega) = \Sigma_{tr}\left[-\frac{l(l+1)}{2} + \frac{l(l+1)(l+2)(l-1)}{16}(1-\mu^*)\right] + O\left((1-\mu^*)^2\right) \tag{4.34}$$

The relative error in the lth eigenvalue becomes

$$\begin{aligned} \epsilon_l &\equiv \left|\frac{\lambda_l - \Sigma_{tr}l(l+1)/2}{\Sigma_{tr}l(l+1)/2}\right| + O\left((1-\mu^*)^2\right) \\ &= \frac{(l+2)(l-1)}{8}(1-\mu^*) + O\left((1-\mu^*)^2\right) \end{aligned} \tag{4.35}$$

The error increases with higher Legendre moments and decreases as μ^* approaches 1. Table 4.1 shows the error in using the discrete representation to model the Fokker-Planck operator for various values of $1-\mu^*$ and for $l = 5, 10, 15,$ and 20.

Legendre Moment	**Error** $\epsilon_l(\mu^*)$			
$1-\mu^*$	1×10^{-3}	1×10^{-4}	1×10^{-5}	1×10^{-6}
$l=5$	0.0035	0.0004	3.5×10^{-5}	3.5×10^{-6}
$l=10$	0.0135	0.0014	1.35×10^{-4}	1.35×10^{-5}
$l=15$	0.0298	0.0030	2.98×10^{-4}	2.98×10^{-5}
$l=20$	0.0522	0.0052	5.23×10^{-4}	5.23×10^{-5}

Table 4.1: Error in the lth eigenvalue from using a delta function representation with $\mu^* \neq 1$.

In practice, this becomes a very simple means of simulating the Fokker-Planck operator. The first step is to select a μ^* that is very close to unity. Then, we randomly sample the distance between collisions using

$$s = \frac{\mu^* - 1}{\Sigma_{tr}} \ln(\xi) \tag{4.36}$$

where ξ is a uniformly distributed random number in the unit interval. At each collision, the scattering angle is deterministic by construction of the DCS and $\mu_0 = \mu^*$ each time. The azimuthal angle is still sampled uniformly in the interval $[0, 2\pi)$, so the actual spreading of the particle beam is still random at each collision. The real difficulty is in choosing μ^* sufficiently close to 1. This requires the user to iterate over μ^* until the solution converges. However, in practice an iteration is seldom necessary as μ^* can be set very close to 1 and left alone for many applications.

The convergence of this representation is plotted in Fig.(4.4) for $\Sigma_{tr} = 1/(1000L)$ and $\Sigma_{tr} = 1/(10000L)$ where L is the thickness of the medium. For each case, μ^* was chosen such that $\lambda^* = (1-\mu^*)/\Sigma_{tr}$ was $L/10$, $L/100$, and $L/1000$. Further increase of λ^* beyond $L/10$ leads to discrete artifacts due to the deterministic nature of sampling the scattering angle. From the figure, we can see that the largest mean free path is not quite converged while the two smaller mean free paths seem to be converged. Furthermore, the convergence seems to be independent of Σ_{tr}. Though

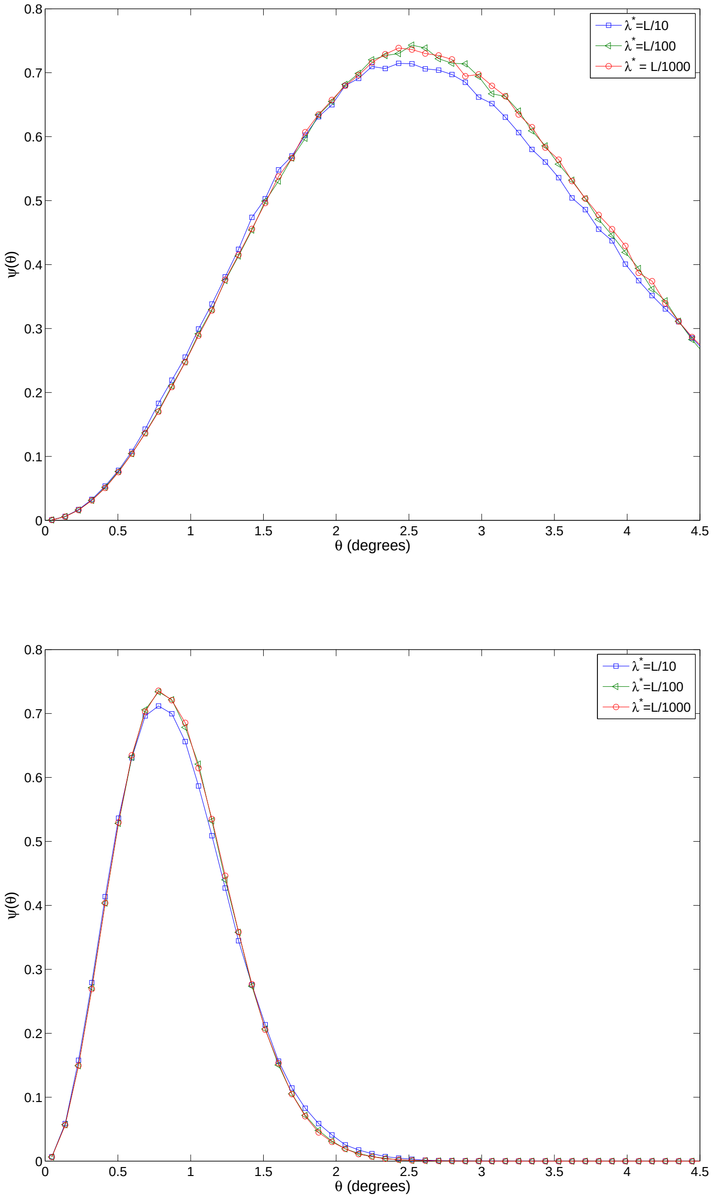

Figure 4.4: Fokker-Planck convergence with λ^* for $\Sigma_{tr} = 1/(1000L)$ and $\Sigma_{tr} = 1/(10000L)$.

this is not rigorous, it does imply that convergence to the Fokker-Planck operator can be nearly achieved by setting μ^* such that $\lambda^* \approx X_{min}/100$ where X_{min} is the minimum length scale in the problem. That is, we let

$$\mu^* = 1 - \frac{\Sigma_{tr} X_{min}}{100} \tag{4.37}$$

The run times required to obtain the results in Fig.(4.4) are shown in Table 4.2. All runtimes are in units of per million particle histories and were obtained using $L = 1$. It is conceivable that a problem could have a much smaller length scale, and the runtime would scale as X_{max}/X_{min}. Therefore, these runtimes can be deceiving as to how fast this method works. For instance, one may be simulating particles in a geometry where the particles are incident on several small layers. Getting the results correct in each of the small layers separately would be tantamount to shrinking λ^* to values that would render the method useless.

Length Scale	**Runtimes**		
	$\lambda^* = L/10$	$\lambda^* = L/100$	$\lambda^* = L/1000$
$\Sigma_{tr} = 1/(1000L)$	2.58 s	23.2 s	227 s
$\Sigma_{tr} = 1/(10000L)$	2.51 s	23.0 s	227 s

Table 4.2: Runtime comparison for obtaining the data in Fig.(4.4)

4.2.4 Exponential Representation of the Fokker-Planck Operator

The delta function representation of the Fokker-Planck operator is one of the easiest ways to simulate a forward peaked scattering operator in a Monte Carlo setting. The reason why we are allowed to use it in a Monte Carlo simulation is because it is an operator of the Boltzmann type. Indeed, we may form a valid transport problem around this particular scattering kernel. Thus, it is plausible to conceive of other Boltzmann-like representations of the Fokker-Planck operator that we may use in Monte Carlo codes. We've seen, however, that the very definition of the Fokker-Planck operator involves a limiting process. Thus, a rigorous and exact Boltzmann representation of the Fokker-Planck operator is most likely impossible.

On the other hand, the Fokker-Planck approximation is based only on the first moment of the elastic scattering DCS. For this reason, we may relax the condition that the Fokker-Planck operator is equivalent to the Boltzmann-like scattering operator, but instead require

$$\lim_{\mu^*\to 1}\int_{-1}^{1}(1-\mu)f(\mu;\mu^*)d\mu = \Sigma_{tr} \tag{4.38}$$

with the auxiliary condition

$$\lim_{\mu^*\to 1}\int_{-1}^{1}(1-\mu)^n f(\mu;\mu^*)d\mu = 0 \quad n > 1 \tag{4.39}$$

Then the criteria of Larsen and Börgers are satisfied and the Fokker-Planck representation is appropriate for $f(\mu;\mu^*)$. To this end, we introduce the scattering kernel

$$\Sigma^*(\mu) = \frac{\Sigma_{tr}}{(1-\mu^*)^2}\exp\left(-\frac{1-\mu}{1-\mu^*}\right) \tag{4.40}$$

It is not difficult to show that Eq.(4.38) and Eq.(4.39) are both satisfied. Furthermore, we can set μ^* as in Eq.(4.37) if we assume that $\exp(-2/(1-\mu^*))$ is vanishingly small. This seems plausible and it can be shown that Eq.(4.37) is in fact appropriate if $\Sigma_{tr}\lambda^* << 1$. In a Monte Carlo setting, μ can be sampled using

$$\mu = 1 + (1-\mu^*)\ln\xi \tag{4.41}$$

The value of this representation is that μ is now a random variable. To see how this effects the solution, the method was tested and the results compared to the results in Fig.(4.4) for $\Sigma_{tr} = 1/(10000L)$. This is shown in Fig.(4.5). We see that the two methods are nearly identical for $\lambda^* = L/100$ demonstrating that the two representations are nearly equivalent. For $\lambda^* = L/5$, the delta function representation has discrete artifacts rendering the results useless. However, the exponential representation, though erroneous, is a smooth approximation to the solution.

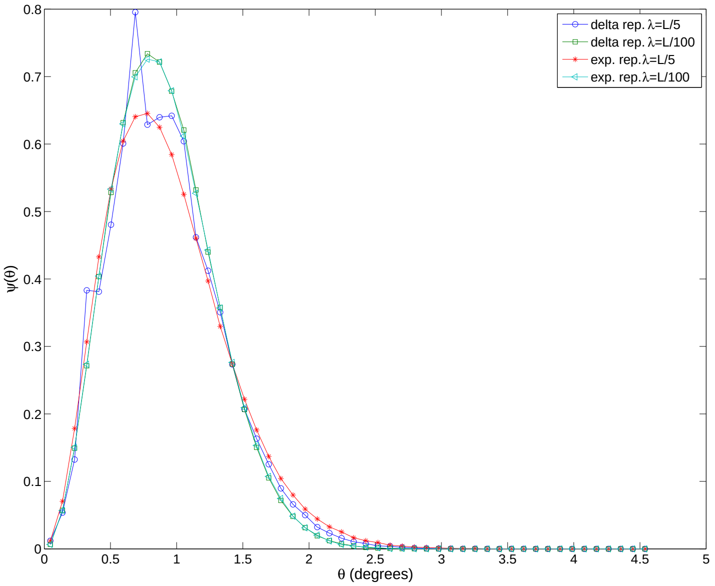

Figure 4.5: Comparison of the results obtained from the delta function and exponential representations of the Fokker-Planck operator

4.2.5 Arbitrary Approximate Representations of the Fokker - Planck Operator

The prescription given previously provides an easy means for checking the validity of a representation of a Fokker-Planck operator. As stated before, there is no known rigorous and exact Boltzmann representation of the Fokker-Planck operator, nor do we expect it to exist since the Fokker-Planck operator is singular by its very definition. However, a great number of approximate Boltzmann-like representations can exist where the approximation can be made arbitrarily close to the actual Fokker-Planck representation.

To construct these approximate representations, one may use delta sequences as a starting point. A delta sequence is defined in the theory of distributions as any smooth function $\delta_a(x)$ such that

$$\lim_{a\to 0}\int_R \delta_a(x)\phi(x)dx = \phi(0) \tag{4.42}$$

where $\phi(x)$ is in the space of test functions and R is any compact space. For our purposes, $R = [-1,1]$ meets this criterion. It is proven that any function $f(x/a)/a$ with

$$\int_R f(x)dx = 1 \tag{4.43}$$

is a delta sequence[29]. This theorem gives us an infinite supply of delta sequences. We also have the elementary result

$$\lim_{a\to 0}\int_R \delta_a(x-x_0)\phi(x)dx = \phi(x_0) \tag{4.44}$$

To construct approximate representations, we may use any function of the form

$$f(\mu;\mu^*) = \frac{\Sigma_{tr}C(a,\mu^*)}{1-\mu^*}\delta_a(\mu-\mu^*) \tag{4.45}$$

with $a << 1$. Clearly Eq.(4.38) and Eq.(4.39) are satisfied in the limit as $a \to 0$ with $C(a;\mu^*) \equiv 1$ since this is equivalent to the delta function representation. However, we may choose $C(a,\mu^*)$ such that

$$C(a,\mu^*) = \frac{1-\mu^*}{\int_{-1}^{1}\delta_a(\mu-\mu^*)(1-\mu)d\mu} \tag{4.46}$$

to satisfy Eq.(4.38) for $a \neq 0$ as long as

$$\int_{-1}^{1}\delta_a(\mu-\mu^*)(1-\mu)d\mu \neq 0 \tag{4.47}$$

$$\lim_{\mu^*\to 1} C(a,\mu^*) < \infty \tag{4.48}$$

If these conditions are met, then Eq.(4.39) can be written for any $n > 1$

$$\lim_{\mu^* \to 1} \frac{1}{1-\mu^*} \int_{-1}^{1} \delta_a(\mu - \mu^*)(1-\mu)^n d\mu = 0 \tag{4.49}$$

From Eq.(4.44) and by definition of a limit, we may write

$$\int_{-1}^{1} \delta_a(\mu - \mu^*)(1-\mu)^n d\mu = (1-\mu^*)^n + \epsilon_a \tag{4.50}$$

where ϵ_a is a number that can be made arbitrarily small by appropriate choice of a. Then Eq.(4.49) becomes

$$\lim_{\mu^* \to 1} \frac{\epsilon_a}{1-\mu^*} + (1-\mu^*)^{n-1} = 0 \tag{4.51}$$

For fixed a, ϵ_a is fixed and this condition cannot be satisfied rigorously in most cases. However, since we are not constructing an equivalent operator to the Fokker-Planck operator, this condition can be nearly satisfied in practice if a is chosen such that $\epsilon_a << 1 - \mu^*$. An ad hoc method for achieving this is to let $a = (1-\mu^*)^m$ with m chosen appropriately for the given delta sequence. Typically, the construction of the representation will suggest an appropriate m.

For example, consider the delta sequence given by

$$\delta_a(\mu - \mu^*) = \begin{cases} \frac{1}{a} & : \quad \mu^* - a < \mu < \mu^* + a \\ 0 & : \quad \mu < \mu^* - a, \quad \mu > \mu^* + a \end{cases} \tag{4.52}$$

Integration of this function weighted by $(1-\mu)^n$ gives

$$\begin{aligned} \int_{\mu^*-a}^{\mu^*+a} \frac{(1-\mu)^n}{a} d\mu &= \frac{(1-\mu^*+a)^{n+1} - (1-\mu^*-a)^{n+1}}{a(n+1)} \\ &= 2(1-\mu^*)^n + O(a^2) \end{aligned} \tag{4.53}$$

From this we see that $C(a, \mu^*) \equiv 1/2$ from Eq.(4.46) and $a = 1 - \mu^*$ is sufficient for meeting the condition in Eq.(4.51). Then, the representation is given by

$$f(\mu; \mu^*) = \begin{cases} \frac{\Sigma_{tr}}{2(1-\mu^*)^2} & : \quad 2\mu^* - 1 < \mu < 1 \\ 0 & : \quad \mu < 2\mu^* - 1 \end{cases} \tag{4.54}$$

and

$$\int_{-1}^{1} f(\mu;\mu^*)d\mu = \frac{\Sigma_{tr}}{1-\mu^*} \tag{4.55}$$

We've seen that the Fokker-Planck operator can be simulated using a Monte Carlo framework using various representations of the Fokker-Planck operator. In each case, we see that additional error is generated by truncating the limit processes involved. In many cases, one does not use Fokker-Planck because multiple scattering theories can be made more robust. The first of these that will be explored can be derived from the Fokker-Planck approximation. However, it will also be shown to exist independent of the Fokker-Planck approximation.

4.3 Gaussian Distributions and the Fermi approximation

One of the most widely used simplifications in high energy charged particle transport is the Gaussian distribution. The reason is that it gives an analytical result for the spreading of a beam of particles traversing a certain thickness of material. This becomes useful if one needs to correlate the position of particles, say measured by an array of detectors, by their source. One application that uses this approximation is muon tomography[30], where particles are measured at two detectors with some item to be imaged in between. The high energy muons are then assumed to be scattered in the intermediate region by way of a Gaussian, and the amount of spreading is assumed proportional to the mass of the target atoms in the material. In this way, high mass materials can be imaged and isolated in a border control process.

An approximation that gives a Gaussian distribution to the spreading of a beam of charged particles is often called the Fermi approximation. This is because Enrico

Fermi was one of the first to recognize that the approximation could be used and he developed one of the first derivations. However, the approximation can be derived in many ways. Two methods of deriving the approximation will be discussed here and the accuracy of the Fermi approximation will be examined afterwards.

4.3.1 Derivation of Fermi's Approximation from the Fokker-Planck Equation

The first derivation of the Gaussian approximation can be traced back in the literature to the earliest charged particle transport approximations. It is a robust formulation because many of its properties can be easily traced back to the Boltzmann transport equation. We will use the method employed by Prinja and Pomraning[31] to derive the approximation here. For this purpose, we find it convenient to change variables from μ and ϕ to

$$\eta = \sqrt{1-\mu^2}\cos\phi \tag{4.56}$$

$$\xi = \sqrt{1-\mu^2}\sin\phi \tag{4.57}$$

Then Eq.(4.21) can be rewritten in terms of the new independent variables.

$$\begin{aligned}&\sqrt{1-\eta^2-\xi^2}\frac{\partial\psi}{\partial z}+\eta\frac{\partial\psi}{\partial x}+\xi\frac{\partial\psi}{\partial y}\\&=\frac{\Sigma_{tr}}{2}\left[\frac{\partial}{\partial\eta}(1-\eta^2)\frac{\partial\psi}{\partial\eta}-2\eta\xi\frac{\partial^2\psi}{\partial\eta\partial\xi}+\frac{\partial}{\partial\xi}(1-\xi^2)\frac{\partial\psi}{\partial\xi}\right]\end{aligned} \tag{4.58}$$

A change of dependent variable from ψ to

$$\Psi(x,y,z,\eta,\xi)=\frac{\psi(x,y,z,\eta,\xi)}{\sqrt{1-\eta^2-\xi^2}} \tag{4.59}$$

allows us to rewrite Eq.(4.58) as

$$\frac{\partial \Psi}{\partial z} + \eta \frac{\partial \Psi}{\partial x} + \xi \frac{\partial \Psi}{\partial y} = \frac{\Sigma_{tr}}{2}\left[\frac{\partial^2 \Psi}{\partial \eta^2} + \frac{\partial^2 \Psi}{\partial \xi^2}\right] + C \tag{4.60}$$

$$\Psi(x, y, 0, \eta, \xi) = \delta(x)\delta(y)\delta(\eta)\delta(\xi) \tag{4.61}$$

$$\begin{aligned} C = (1 - \sqrt{1 - \eta^2 - \xi^2})\frac{\partial \Psi}{\partial z} - \frac{\Sigma_{tr}}{2}\Bigg[\eta^2 \frac{\partial^2 \Psi}{\partial \eta^2} + 4\eta \frac{\partial \Psi}{\partial \eta} \\ +2\eta\xi \frac{\partial^2 \Psi}{\partial \eta \partial \xi} + 2\Psi + 4\xi \frac{\partial \Psi}{\partial \xi} + \xi^2 \frac{\partial^2 \Psi}{\partial \xi^2}\Bigg] \end{aligned} \tag{4.62}$$

A simple scaling $\eta \rightarrow \epsilon\eta$ and $\xi \rightarrow \epsilon\xi$ proves that Eq.(4.62) is $O(1)$ while Eq.(4.60) is $O(1/\epsilon^2)$. Also, by Eq.(4.56) and Eq.(4.57), we see that the limit $\epsilon \rightarrow 0$ is clearly justified as long as the beam stays forward directed. Therefore, we set $C = 0$ to obtain the Fermi approximation. Also, since η and ξ resemble independent variables in Cartesian space, we will allow for these variables to be defined on the extended real line $(-\infty, \infty)$.

Using these assumptions, Eq.(4.60) has an analytic solution that can be derived by using Fourier transform methods. It is given by [32],

$$\psi(x, y, z, \eta, \xi) = \frac{3}{\pi^2 \Sigma_{tr}^2 z^4} \exp\left[-\frac{2}{\Sigma_{tr}}\left(\frac{3(x^2 + y^2)}{z^3} - \frac{3(\eta x + \xi y)}{z^2} + \frac{(\eta^2 + \xi^2)}{z}\right)\right] \tag{4.63}$$

For the purposes of this thesis, a simpler version of this solution is appropriate. If we integrate over the x and the y-variables, then we get the angular distribution at penetration z given by,

$$\Theta(\eta, \xi, z) = \frac{1}{2\pi\Sigma_{tr} z} \exp\left[-\frac{(\eta^2 + \xi^2)}{2\Sigma_{tr} z}\right] \tag{4.64}$$

We see now why it is justified to allow η and ξ to extend over the real line. When Σ_{tr} is small, an assumption that is always valid in these applications, this Gaussian distribution falls off very rapidly in these variables. A more more suitable form may be obtained by substituting for η and ξ using Eq.(4.56) and Eq.(4.57),

$$\Theta(\mu, z) = \frac{1}{2\pi\Sigma_{tr} z} \exp\left[-\frac{(1 - \mu^2)}{2\Sigma_{tr} z}\right] \tag{4.65}$$

An intuitive justification of this process can be given by a simple geometric picture. The scattering process happens on the unit sphere. The Fokker-Planck approximation for forward peaked transport treats the scattering as random motion on the unit sphere near $\mu_0 = 1$. The Fermi approximation treats this random motion as if it were on a plane, an assumption that is justified if the particle's motion does not allow it to stray too far from $\mu = 1$. Since the planar picture is not practical for use in transport codes, we use the definitions of the variables η and ξ to cast the approximation back onto the unit sphere.

A distribution for the scattering angle can be obtained by substituting $\mu = \cos\theta$ and using $\sin\theta \approx \theta$ in the small angle approximation to obtain

$$\Theta(\theta, z) = \frac{1}{2\pi\Sigma_{tr} z} \exp\left[-\frac{\theta^2}{2\Sigma_{tr} z}\right] \tag{4.66}$$

A convenient formula for the radial spreading of an initially collimated beam can also be derived from Eq.(4.63). It is given by[25]

$$\phi(r, z) = \frac{3}{2\pi\Sigma_{tr} z} \exp\left[-\frac{3r^2}{2\Sigma_{tr} z}\right] \tag{4.67}$$

This seems like a long ways from the Fokker-Planck equation. However, it can be demonstrated that the discrepancy between the Fokker-Planck approximation and the Fermi approximation is very small[25]. We will give examples demonstrating this fact soon. However, it is interesting to see that there is another way of obtaining Eq.(4.66) based on first principles and the assumption of small angle scattering.

4.3.2 Rossi's Formulation of the Gaussian Approximation

The derivation here follows the work of Rossi[16] and is originally due to Fermi. In Rossi's work, the Rutherford scattering kernel takes the form

$$\Sigma_e(\theta) = \frac{K}{(\theta^2 + \theta_1^2)^2} \tag{4.68}$$

where K is the same energy dependent constant as in Eq.(3.32) and $\theta_1 = \sqrt{\eta}$ which is given in Eq.(3.8). We note that this approximation is equivalent to Eq.(3.32) in the small angle approximation. We introduce the angles θ_x and θ_y which are the xz and yz planar angles between the particles projected trajectory and the z-axis. A graphical depiction is shown for the angle θ_x in Fig.(4.6). We also introduce the projected differential scattering probability $\xi(\theta_x)d\theta_x$ and $\xi(\theta_y)d\theta_y$; the probability per unit path length of scattering into a projected angle in the xz and yz plane in the intervals $[\theta_x, \theta_x + d\theta_x]$ and $[\theta_y, \theta_y + d\theta_y]$ respectively. When the small angle approximation is justified, we may write

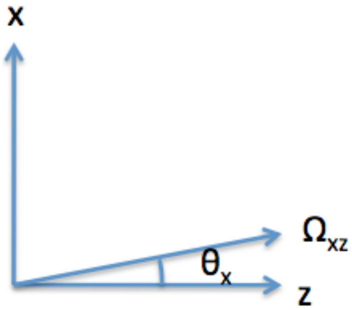

Figure 4.6: Graphical depiction of θ_x to the geometry of the transport problem.

$$\theta^2 \approx \theta_x^2 + \theta_y^2 \tag{4.69}$$

$$\xi(\theta_{x,y}) = \int_{-\theta_2}^{\theta_2} \Sigma_e \left(\sqrt{\theta_x^2 + \theta_y^2} \right) d\theta_{y,x} \tag{4.70}$$

θ_2 is given in Eq.(3.12) and is the upper bound to the validity of the DCS given by Rossi[16]. From the physics, it is clear that all arguments that hold for the xz plane hold for the yz plane as well. We will consider how the transport of a particle evolves in the xz plane only. We introduce the probability density function $P(x, z, \theta_x)$ of finding a particle in the interval $[x, x + dx]$ and $[\theta_x, \theta_x + d\theta_x]$ after traversing a thickness z. A simple balance can be obtained by equating the change in particle density to the in-scatter and out-scatter to obtain,

$$\frac{dP}{dz} = -\theta_x \frac{\partial P}{\partial x} + \int_{-\theta_2}^{\theta_2} [P(x, z, \theta_x + \theta'_x) - P(x, z, \theta_x)]\xi(\theta'_x)d\theta'_x \tag{4.71}$$

Since Σ_e and hence ξ are highly forward peaked functions, we assume that $P(x, z, \theta_x + \theta'_x)$ can be approximated by a Taylor series in θ'_x for the purpose of evaluating the integral. Then, keeping the first two terms gives

$$\begin{aligned} &\int_{-\theta_2}^{\theta_2} [P(x, z, \theta_x + \theta'_x) - P(x, z, \theta_x)]\xi(\theta'_x)d\theta'_x \\ \approx &\frac{\partial P}{\partial \theta_x} \int_{-\theta_2}^{\theta_2} \theta'_x \xi(\theta'_x)d\theta'_x + \frac{1}{2}\frac{\partial^2 P}{\partial \theta_x^2} \int_{-\theta_2}^{\theta_2} \theta'^2_x \xi(\theta'_x)d\theta'_x \end{aligned} \tag{4.72}$$

The first integral is zero since the integrand is odd. The second integral is given the value $\theta_s^2/2$ with

$$\theta_s^2 = \int_{-\theta_2}^{\theta_2} \theta^2 \Sigma_e(\theta)d\theta \tag{4.73}$$

The factor of $1/2$ comes from the symmetry between θ_x and θ_y. Then the equation for P is given by

$$\frac{dP}{dz} = -\theta_x \frac{\partial P}{\partial x} + \frac{\theta_s^2}{4}\frac{\partial^2 P}{\partial \theta_x^2} d\theta'_x. \tag{4.74}$$

This equation is similar to Eq.(4.60) and indeed the normalized solution is

$$P(x, z, \theta_x) = \frac{2\sqrt{3}}{\pi}\frac{1}{\theta_s^2 z^2} \exp\left[-\frac{4}{\theta_s^2}\left(\frac{\theta_x^2}{z} - \frac{3x\theta_x}{z^2} + \frac{3x^2}{z^3}\right)\right]. \tag{4.75}$$

Again, the angular distribution at z can be obtained through integration over the x variable to obtain

$$\Theta_x(z, \theta_x) = \frac{1}{\sqrt{\pi z}\theta_s} \exp\left(-\frac{\theta_x^2}{\theta_s^2 z}\right) \tag{4.76}$$

Multiplying this by the same distribution obtained for θ_y and using Eq.(4.69) gives

$$\Theta(z, \theta) = \frac{1}{\pi z \theta_s^2} \exp\left(-\frac{\theta^2}{\theta_s^2 z}\right) \tag{4.77}$$

We see that Eq.(4.77) is equivalent to Eq.(4.66) if we can equate $\theta_s^2/2$ to Σ_{tr}. An explicit formula for $\theta_s^2/2$ is given by Rossi using the screened Rutherford DCS.

$$\frac{1}{2}\theta_s^2 = K\left[\ln\left(\frac{\theta_1^2+\theta_2^2}{\theta_1^2}\right)-1\right] \tag{4.78}$$

This is equivalent to Eq.(3.35) if we take $\eta = \theta_1^2$, $1+\eta \approx 1$, and $\theta_2 = 1$. The first condition is satisfied by the definitions given in chapter 2. The second condition is clearly satisfied from previous arguments also given in chapter 2. The third condition is not always satisfied in high energy, heavy charged particle transport applications. However, it is noted by Rossi that $\theta_2 = 1$ when the formula in Eq.(3.12) increases above 1. This only happens at sufficiently low energies however. Thus, we see that the two formulations are indeed equivalent at lower energies, but they deviate slightly from each other at very high energies.

4.3.3 Accuracy of the Fermi Approximation

Based on the first derivation of the Fermi approximation, we see that it can never be more accurate than the Fokker-Planck approximation. Therefore, we will discuss only the accuracy of the Fermi approximation with respect to the Fokker-Planck approximation and all results obtained for the latter will apply to the limiting case of the former. This will simplify our analysis later as it won't be necessary to carry around separate results for the two different approximations. We will now see numerical evidence that the Fermi approximation is indeed as good as the Fokker-Planck approximation for the accuracy that is needed in many calculations.

We consider first the Fermi approximation as it is given in Eq.(4.66) where the parameter of interest is Σ_{tr} as it is given in Eq.(3.35). Very often the Fermi approximation is used in a condensed history setting where the particle is moved a fixed step s, and the particles scattering angle is sampled from the distribution in Eq.(4.66) as discussed in section 2.3. Obviously, there will be additional error due to the sampling interval, so several cases of varying s will be examined.

The first test case is a 10 cm thick slab with $\Sigma_{tr} = 2.0 \times 10^{-5}$ and $\Sigma_t = 44000$. The Fokker-Planck approximation as given by the delta function representation is observed to converge at $\lambda^* = 0.01$. The Fermi distribution was used with step sizes as shown in the figures. We see from Fig.(4.7) that the angular distribution due to the Fermi approximation is not significantly different from the angular distribution due to the Fokker-Planck approximation. However, the peak scattering angle is still very small in this test case, so the Fermi approximation is valid even when the step length is 5 cm.

The second test case is identical to the first except that $\Sigma_{tr} = 2.0 \times 10^{-3}$. In this case, there is much more scattering, and the beam is expected to spread much more than in the previous test case. The results are shown in Fig.(4.8). However, we see that the two approximations are nearly identical still, even for large step sizes. For both cases, the error for the largest two step sizes is shown. We see that the error is of the same order of magnitude in each case indicating that the effect of raising Σ_{tr} is negligible when considering a step size since $\Sigma_{tr}\Delta s << 1$. If this quantity becomes large, then we expect to see a large deviation between Fokker-Planck and Fermi since the approximation of the unit sphere with a plane near $\mu = 1$ would then cease to be justified.

In many condensed history codes, a correction to the particles radial displacement from the forward direction is not directly sampled at the end of a step. For this reason, the step sizes are made small so that the trajectory may be accounted for over very small distances. The reason for this is that many Monte Carlo codes allow for very complicated geometry specifications, and condensed history methods require special handling near these interfaces. Therefore, a proper treatment of the radial redistribution near an interface becomes exceptionally difficult.

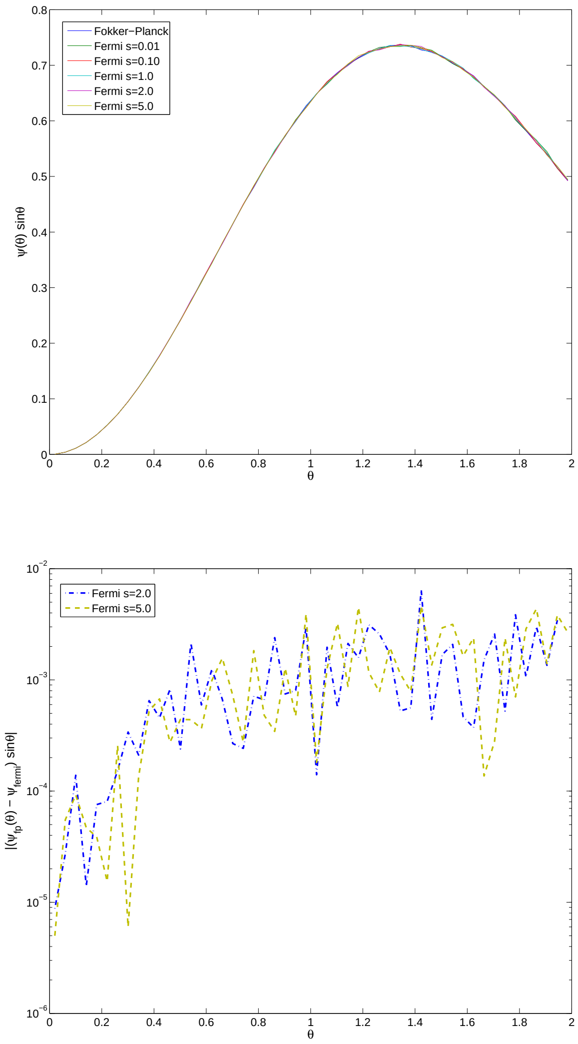

Figure 4.7: Angular distributions for the Fokker-Planck approximation and the Fermi approximation with varying step sizes for $\Sigma_{tr} = 2.0 \times 10^{-5}$

Radial distributions for the previous two test cases were generated with no radial displacement sampling. The results are shown in Fig.(4.9) for the first case and Fig.(4.10) for the second case. The distributions are noticeably erroneous for step sizes equal to or greater than 1 cm for both test cases. Furthermore we see that the error is more pronounced for the first test case. This is not surprising since the

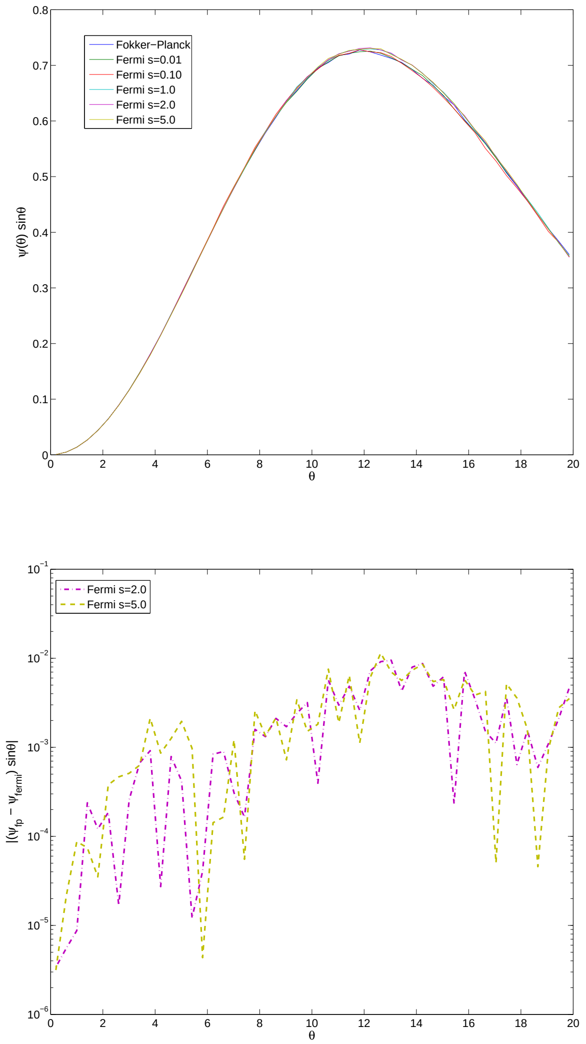

Figure 4.8: Angular distributions for the Fokker-Planck approximation and the Fermi approximation with varying step sizes for $\Sigma_{tr} = 2.0 \times 10^{-3}$

distribution for that case is more peaked. However, we see that we are limited to very small step sizes in both cases in order to resolve the radial distribution at the end of the slab.

The numerical evidence demonstrates what is already well known; the Fermi

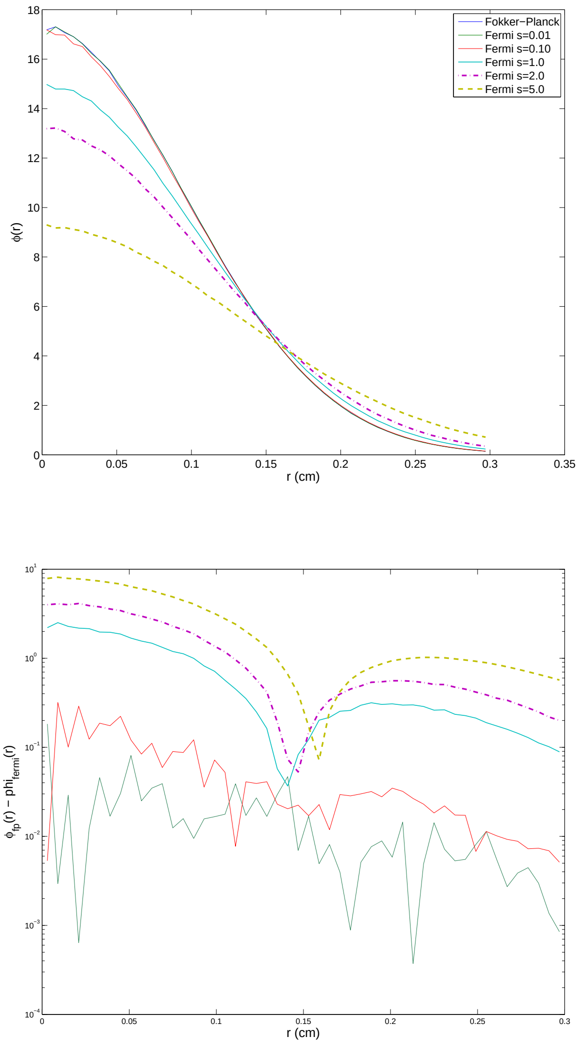

Figure 4.9: Radial distributions for the Fokker-Planck approximation and the Fermi approximation with varying step sizes for $\Sigma_{tr} = 2.0 \times 10^{-5}$

approximation is as good as the Fokker-Planck approximation when the sampling step sizes are made sufficiently small. The distribution of scattering angles due to Rossi is nearly identical to the one used in the previous test cases with one exception. He gives an upper bound to the limit of integration when computing the mean square of the scattering angle. This upper bound is energy dependent, and thus

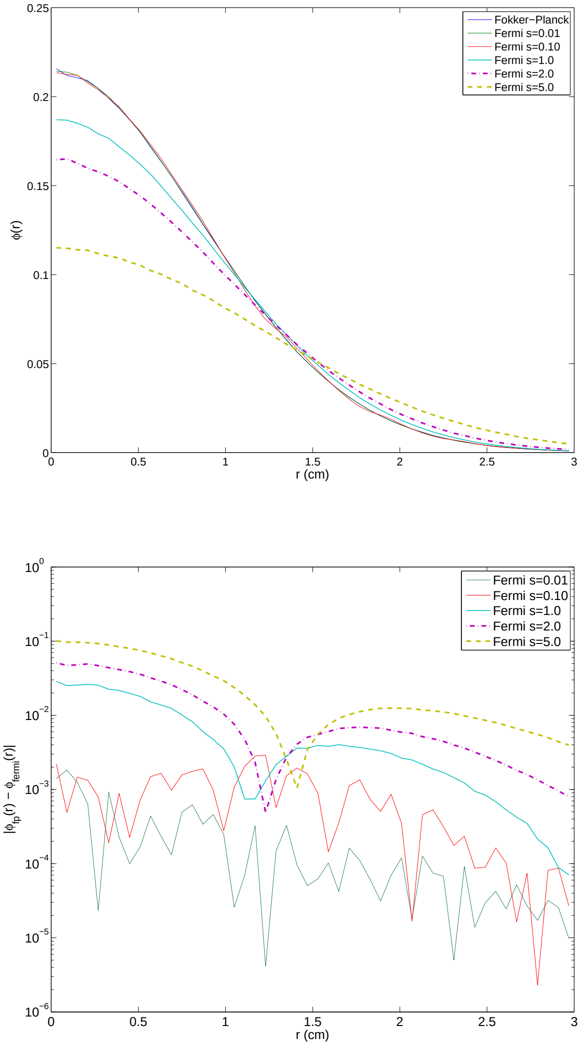

Figure 4.10: Radial distributions for the Fokker-Planck approximation and the Fermi approximation with varying step sizes for $\Sigma_{tr} = 2.0 \times 10^{-3}$

fairly complicated to discuss generally. To see the effect of the parameter θ_2, we consider protons and alpha particles incident on tungsten metal. A plot of θ_2 as given in Eq.(3.12) is shown in Fig.(4.11). The upper bound on this angle is unity as described in Rossi's work. For both particle types, we see that the angle tends toward zero like $1/\sqrt{E}$ after some initial region.

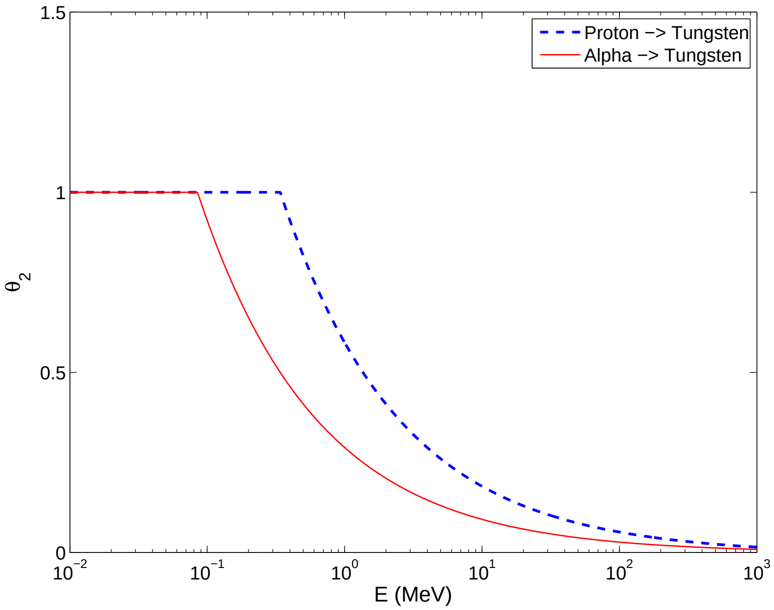

Figure 4.11: Rossi's upper bound θ_2 for the validity of a Rutherford scattering formula when used with a Gaussian formulation.

The initial region corresponds to the area where Rossi's derivation overlaps with the first derivation of the Fermi distribution. We note that the only relevant parameter to discuss in the two distributions is Σ_{tr} and $\theta_s^2/2$. A ratio of the value used in Rossi's distribution and Σ_{tr} is shown in Fig.(4.12) for protons and alphas incident on tungsten. Though the parameter θ_2 varies relatively quickly for the energy range given, the ratio of the mean square scattering varies slower. The interpretation is that Rossi's derivation cuts off larger angle scattering, thus reducing the mean square scattering angle. The overall effect is to shift angular distributions to the left and to make radial distributions more peaked.

Numerical evidence of this fact can be easily demonstrated. We consider 1000 MeV protons incident on tungsten metal with thickness 1.0 cm. Then the value of $\theta_s^2/2$ is about 0.62 from Fig.(4.12). We see the radial and angular distributions plotted

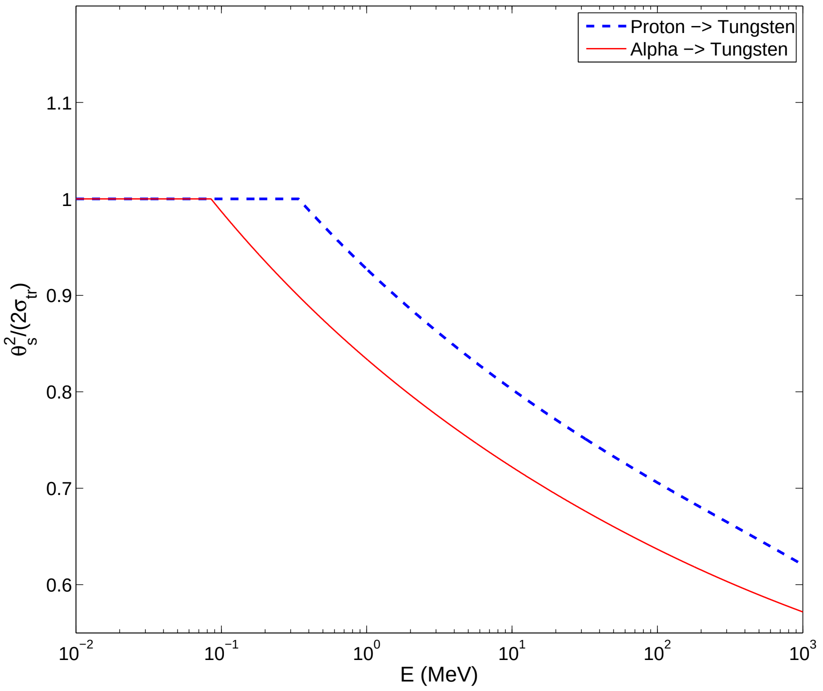

Figure 4.12: The ratio $\theta_s^2/(2\Sigma_{tr})$ in mean square scattering angles between the two derivations for the Fermi approximation.

in Fig.(4.13) for the Fokker-Planck approximation, both Fermi approximations, and the result obtained from running an analog Monte Carlo simulation. As expected, the distribution due to Rossi is more forward peaked then the distribution derived from the Fokker-Planck approximation. We see more evidence that the Fokker-Planck and Fermi approximations are identical for identical Σ_{tr}.

The interesting result is that, though the Fokker-Planck distribution is very bad at approximating the analog distribution, Rossi's approximation appears as a correction to the Gaussian since it is much closer to the analog distribution. This is the first indication of a very intuitive fact. Any theory that seeks to obtain results based on the first moment of the DCS will fail because the large angle scattering is only accounted for by an overall shift of the mean scattering angle away from 0. In Rossi's formulation, the large angle scattering is neglected in a systematic way such that the shift is less severe.

In this way, we can make the peak of the Gaussian result move close to the peak of the analog result by reducing Σ_{tr} giving the appearance of a better approximation. However, we know from section 3.4 that the large angle scattering should not be neglected. This conundrum leads to the conclusion that a Gaussian approximation can seldom be an accurate description of high energy charged particle transport processes.

4.4 Preliminary Conclusions

We have seen two highly favored approximations in the scattering angle distribution over macroscopic distances. We saw indications of the lack of accuracy of the Fokker-Planck approximations due to the slowly varying error term in Fig.(4.3). We note that, for a given problem, Σ_{tr} is fixed and this error cannot be reduced by brute force techniques such as the reduction of the mean free path in the delta function representation. Also, no other representation will give better accuracy either.

The tendency is to believe that a converging of the Fokker-Planck solution while adjusting λ^* in a representation is a convergence to a true solution. However, this is no more true than saying an iterative method for solving a system of equations due to the finite element approximation is converging to the analytic solution. The approximation of the methods still remain, and the error of solving the problem with the representation is being reduced. Unlike the finite element analogy, there is no way to fix the error of a Fokker-Planck approximation at runtime.

These facts may seem obvious, but their statement carries powerful conclusions.

Many real world applications still use these or similar approximations to compute charged particle densities. Much work is devoted to fixing up these approximations to make them more accurate. The random hinge approximation in the EGS5 code[9] and in Sandia National Laboratory's ITS code[10] are notable examples. In that approximation, a method of fixing up the radial distribution without using a radial distribution sampling at the end of a condensed history step is developed.

Energy straggling approximations are similar in form to the approximations presented here. Some of the same conclusions can be drawn for energy straggling approximations as what have been discussed here. The main difference is that the energy straggling is approximated much better by a Gaussian approximation. Though the error still exists, as we will see soon, it is less pronounced because energy redistribution occurs monotonically on the real line while angular distribution occurs as a random walk on the unit sphere. A good discussion of the effect of random motion on the sphere is given by Peterson[26].

Other, more accurate multiple scattering theories exist. Some will be discussed in chapters to come. However, the conclusions drawn here are a good lead into the research that has been conducted for this thesis. They are the moment preserving methods that were briefly introduced in section 2.4.

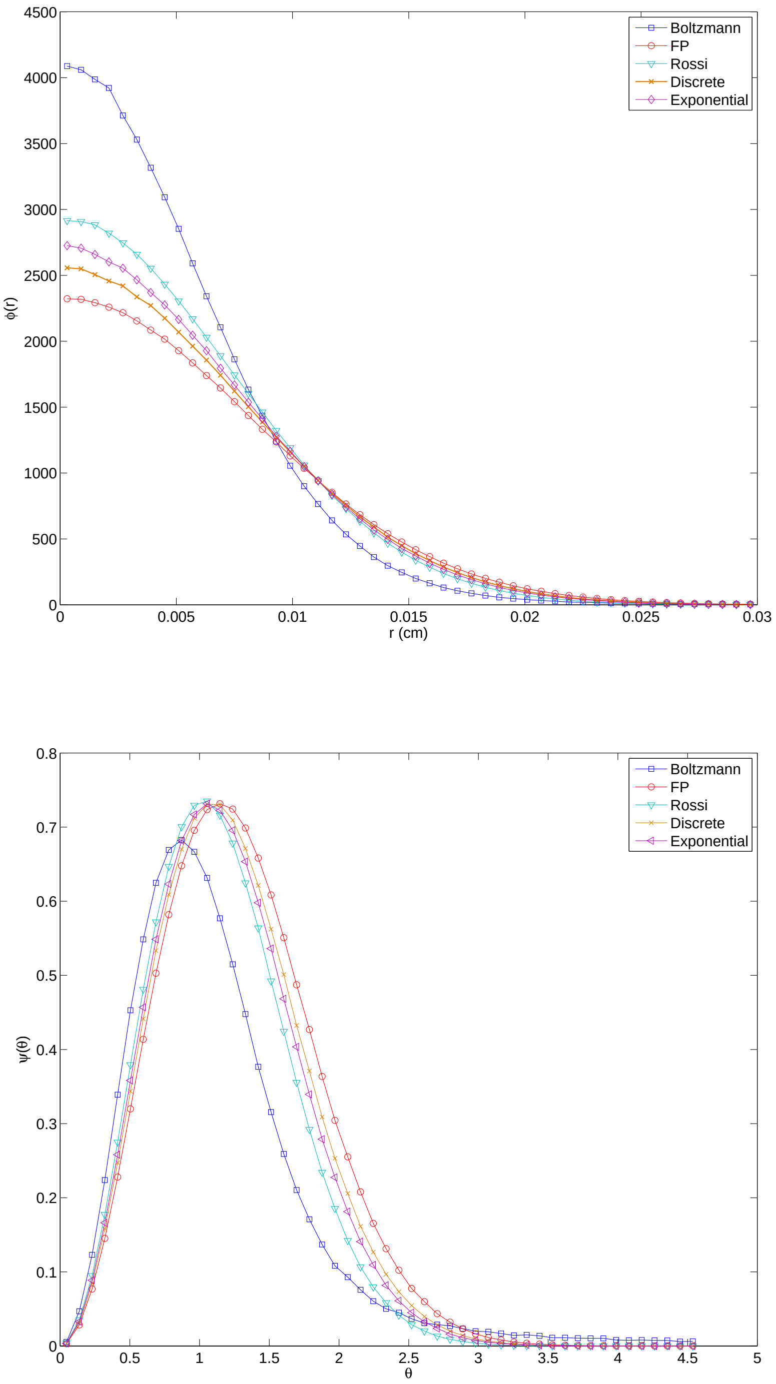

Figure 4.13: Comparison of the Fokker-Planck, Fermi, and Rossi derived approximations with an analog Monte Carlo simulation.

Chapter 5

Regularization and Moment Preserving Methods

So far we have seen how the singular nature of the elastic and inelastic DCS near zero energy loss and scattering angles allow us to approximate the behavior of a particle's trajectory smoothly over macroscopic distances. The Fokker-Planck approximation became a starting point for this analysis since it allowed us to replace the Boltzmann scattering integral with a smooth diffusion operator. However, the applicability of this approximation was shown to be very limited.

In formulating the Fokker-Planck approximation, we relied heavily on the transport cross section defined in Eq.(3.35). Though we were able to argue the physical significance of this parameter, it is no more than a moment of the elastic scattering DCS. A moment of a distribution $f(x)$ is typically defined as

$$f_n = \int_R x^n f(x) dx \tag{5.1}$$

The first moment is what we would normally consider to be the mean of the distribution $\overline{x}$. The central moments of a distribution are defined using the mean as

$$\chi_n = \int_R (x - \overline{x})^n f(x) dx \tag{5.2}$$

The second central moment is the variance and the third central moment is the skewness. The mean and the variance of a distribution are typically the two most important pieces of information about that distribution since they measure central tendency and scatter around the central tendency.

In a general sense, however, a smooth bounded function in a region can always be described by its moments with some complete set of basis functions, typically countably infinite in number. In quantum mechanics, this plays a central role in the description of particle states, and thus there has been a large body of work devoted to the subject. In our own context, we saw this with the Legendre expansion of the DCS in Eq.(2.7) when we attempted to simplify the transport equation, and in Eq.(2.11) and Eq.(2.12) when we wrote out the P_N approximation.

In the context of the work given here, the transport cross section is the first of a series of moments given by

$$\xi_{e,n} = \int_{-1}^{1} (1-\mu)^n \Sigma_e(\mu) d\mu = \Sigma_{e,0}\overline{(1-\mu)^n} \tag{5.3}$$

and the stopping power and straggling coefficient are the first and second moments of a series of moments given by

$$Q_n \equiv \xi_{in,n} = \int_{Q_{min}}^{Q_{max}} Q^n \Sigma_{in}(Q) dQ = \Sigma_{in,0}\overline{Q^n}. \tag{5.4}$$

The former will be known as the transport moments of the elastic cross section and the latter will be known as the energy-loss moments of the inelastic cross section. In section 4.2, the importance of these general moments were alluded to in the derivation of the Fokker-Planck approximation. We will now present the higher order Fokker-Planck expansion and further explore the importance that these moments have in simplifying the high energy charged particle transport equation.

5.1 Higher Order Fokker-Planck Expansion

The discussion of the higher order Fokker-Planck expansion will again follow the work of Larsen and Leakes primarily[27]. We consider an arbitrary expansion of the Legendre polynomials in Eq.(4.13) as follows.

$$\begin{aligned}\Sigma_{e,k}(\mu_0) = \int_{-1}^{1} d\mu_0 \Sigma_e(\mu_0) \sum_{j=0}^{J} \frac{P_k^{(j)}(1)}{j!}(\mu_0 - 1)^j \\ = \sum_{j=0}^{J} (-1)^j \frac{P_k^{(j)}(1)}{j!} \xi_{e,j}\end{aligned} \tag{5.5}$$

Then, it is conceivable to keep as many terms as we like. Consider a three term expansion, one more than the usual Fokker-Planck approximation, given by

$$\begin{aligned}\Sigma_{e,k}(\mu_0) \approx \xi_0 P_k(1) - \xi_1 P_k'(1) + \frac{\xi_2}{2} P_k''(1) \\ = \xi_0 - \frac{k(k+1)}{2}\xi_1 + \frac{[k(k+1)]^2 - 2k(k+1)}{16}\xi_2\end{aligned} \tag{5.6}$$

We again recognize the eigenvalues of the spherical Laplacian operator, $\lambda_k = k(k+1)$, in each term. We can specify the action of L_B on a spherical harmonic using the higher order expansion giving

$$L_B Y_l^m(\Omega) \approx \left(\frac{\xi_1}{2} + \frac{\xi_2}{8}\right) l(l+1) Y_l^m(\Omega) + \frac{\xi_2}{16}[l(l+1)]^2 Y_l^m(\Omega) \tag{5.7}$$

Then using the same correpsondance as before, we can rewrite this as

$$L_B Y_l^m(\Omega) \approx \left(\frac{\xi_1}{2} + \frac{\xi_2}{8}\right) \nabla_\Omega^2 Y_l^m(\Omega) + \frac{\xi_2}{16}[\nabla_\Omega^2]^2 Y_l^m(\Omega) \tag{5.8}$$

Therefore, we can write

$$L_B \psi = \left(\frac{\xi_1}{2} + \frac{\xi_2}{8}\right) \nabla_\Omega^2 \psi + \frac{\xi_2}{16}[\nabla_\Omega^2]^2 \psi + O(\xi_3) \tag{5.9}$$

We see that a higher order approximation is given by a higher order partial differential operator on the unit sphere. However, already we can see that the higher order approximation is not suitable. Consider the semi-infinite medium equation for monoenergetic charged particles given by

$$\frac{\partial\psi}{\partial s}(\Omega, s) = L_B\psi(\Omega, s) \tag{5.10}$$

$$\psi(\Omega, 0) = \delta(\mu - 1) \tag{5.11}$$

This system may be solved formally by using an eigenfunction expansion of ψ using spherical harmonics.

$$\psi(\Omega, s) = \sum_{l=0}^{\infty}\sum_{m=-l}^{l} \psi_{lm}(s)Y_l^m(\Omega) \tag{5.12}$$

$$\psi_{lm}(s) = \exp\left[-(\Sigma_{e,0} - \Sigma_{e,l})s\right] \tag{5.13}$$

For physically valid solutions, we must have $\psi(\Omega, s) \to 0$ as $s \to \infty$. Therefore, only solutions with $\Sigma_0 - \Sigma_l > 0$ are permitted. However, since we have

$$\Sigma_{e,l} = \int_{-1}^{1} d\mu_0 \Sigma_e(\mu_0)P_l(\mu_0) \tag{5.14}$$

with $P_0(\mu_0) \geq P_l(\mu_0)$ for $-1 \leq \mu_0 \leq< 1$ and all $l > 0$, then we must have

$$\Sigma_{e,l} < \Sigma_{e,0} \tag{5.15}$$

for every $l > 0$. This means that the condition is always satisfied for any scattering kernel used for L_B. However, the generalized Fokker-Planck operators are not Boltzmann operators. If one replaces L_B with $(\Sigma_{tr}/2)\nabla^2_\Omega$ in Eq.(5.10), then the Fokker-Planck approximation is obtained and the solution in Eq.(5.12) is the same except with

$$\psi_{lm}(s) = \exp\left[-\frac{\Sigma_{tr}}{2}l(l+1)s\right] \tag{5.16}$$

We again have only negative eigenvalues, so the Fokker-Planck approximation is a physically valid approximation to the Boltzmann transport operator. However, if we use Eq.(5.8) for the right hand side of Eq.(5.10), then we get the solution with

$$\psi_{lm}(s) = \exp\left[-\left(\frac{\xi_1}{2}+\frac{\xi_2}{8}\right)l(l+1)s + \frac{\xi_2}{16}[l(l+1)]^2 s\right] \tag{5.17}$$

The eigenvalues become positive for

$$l(l+1) > 2 + \frac{8\xi_1}{\xi_2} \tag{5.18}$$

This obviously will occur for some sufficiently large l. Therefore, we cannot use this approximation for highly forward peaked transport with general boundary conditions. This gives us the indication that obtaining higher order truncations of Eq.(5.5) is not a robust procedure for obtaining higher order approximation to the Boltzmann scattering operator. Pomraning showed that the procedure given above could be extended such that[33]

$$L_B\psi(\Omega) = \sum_{j=1}^{J} a_{j,J}(\nabla^2_\Omega)^j \psi(\Omega) + O(\xi_{J+1}) \tag{5.19}$$

However, there is no reason to believe that an arbitrary approximation will lead to stable solutions.

We recall that the Fokker-Planck approximation could be written in terms of arbitrary Boltzmann type operators such that $\Sigma_{tr} \equiv \xi_1$ was conserved and $\xi_n << \xi_1$. We now introduce a systematic method for doing the same thing for higher order Fokker-Planck approximations. The difference, however, is that a perfect equivalence between the higher order Fokker-Planck approximation is no longer desired as it was in the previous context. Instead, we wish to find general operators, and eventually Boltzmann type operators, that are equivalent to the higher order Fokker-Planck approximation. The remaining degrees of freedom, which are infinite in number, are used to stabilize the expansion while still maintaining an approximate equivalence to the unstable expansion.

5.2 Boltzmann Operator Regularization Procedures

To begin, we propose an operator L_n^* that will approximate the Boltzmann operator L_B up to nth order in ξ. For high energy charged particle applications, ξ_n is $O(\epsilon^{n-1})$ where $\epsilon << 1$. It is usual to construct the operator such that

$$L_n^* \psi = L_B \psi + O(\xi_{n+1}) \tag{5.20}$$

for any function ψ defined on the unit sphere. If this can be accomplished, then the two operators are equivalent up to $O(\epsilon^n)$. For this reason, the eigenvalues are also related by

$$\lambda_n^* = \lambda_{B,n} + O(\epsilon^n). \tag{5.21}$$

The importance of this result is due to the work of Lewis[34]. He showed that, in an homogeneous infinite medium with monoenergetic particles and bounded solution, preserving the first n eigenvalues of the scattering operator is equivalent to preserving the first n space angle moments of the solution. That is, the quantities

$$\int_R d\mathbf{r} \int_{4\pi} d\Omega \Omega_1^{n_1} \Omega_2^{n_2} \Omega_3^{n_3} r_1^{m_1} r_2^{m_2} r_3^{m_3} \psi(\mathbf{r}, \Omega) \tag{5.22}$$

with

$$\sum_{i=1}^{3} n_i + m_i = n \tag{5.23}$$

are conserved. In our case, these quantities are conserved up to some number n, and the remaining moments of the solution are conserved approximately with a leading order error depending on the order of truncation.

The relationship in Eq.(5.20) is often obtained through an intermediate approximation such as the higher order Fokker-Planck expansion in order to get a rigorous expansion in transport moments. However, this is not always the case as will be seen shortly. In any case, the operator L_n^* may be used to form the approximation itself, but often it is further shown to be equivalent to a Boltzmann type operator up to $O(\epsilon^n)$. We will explore this method further by way of some examples.

5.2.1 Regularization of Larsen and Leakes

Larsen and Leakes proposed the operator

$$L_2^* = \alpha L(I - \beta L)^{-1} \tag{5.24}$$

$$L \equiv \nabla_\Omega^2 \tag{5.25}$$

Expanding $(I - \beta L)^{-1}$ gives formally

$$(I - \beta L)^{-1} = \sum_{j=0}^{\infty} (\beta L)^j \tag{5.26}$$

and substituting this into Eq.(5.24) gives

$$L_2^* = \alpha L + \alpha\beta L^2 + O(\alpha\beta^2) \tag{5.27}$$

Preserving the first two terms in the expansion in Eq.(5.9) gives α and β in terms of ξ_1 and ξ_2 up to $O(\epsilon^2)$.

$$\alpha = \frac{\xi_1}{2} + \frac{\xi_2}{8} + O(\epsilon^2) \tag{5.28}$$

$$\beta = \frac{\xi_2}{8\xi_1} + O(\epsilon^2) \tag{5.29}$$

Then given the scaling described previously, α is $O(1)$ and β is $O(\epsilon)$. Using this combined with Eq.(5.27) results in the equivalence described in Eq.(5.20).

$$\begin{aligned} L_2^*\psi &= \alpha L\psi + \alpha\beta L^2\psi + O(\epsilon^2) \\ &= L_B\psi + O(\epsilon^2) \end{aligned} \tag{5.30}$$

Also, the eigenvalues of L_2^* can be computed using the full expansion of $(I-\beta L)^{-1}$.

$$\begin{aligned}
L_2^* Y_l^m(\Omega) &= \alpha L (I-\beta L)^{-1} Y_l^m(\Omega) \\
&= \sum_{j=0}^{\infty} \alpha L (-\beta L)^j Y_l^m(\Omega) \\
&= \sum_{j=0}^{\infty} -\alpha \beta^j [l(l+1)]^{j+1} Y_l^m(\Omega) \\
&= -\alpha l(l+1) \frac{1}{1+l(l+1)\beta} Y_l^m(\Omega)
\end{aligned}$$

The final equality holds for $l(l+1)\beta < 1$. Clearly this is the case for sufficiently small l since β is $O(\epsilon)$ and thus is much less than unity. This does not hold for very large l, however, but this poses no problem since $L_2^* = L_B$ is only an asymptotic equivalence anyhow. The constants α and β are given explicitly by preserving the first three eigenvalues of the Boltzmann scattering operator. They are

$$\alpha = \frac{1}{3} \frac{\Sigma_{a1}\Sigma_{a2}}{\Sigma_{a2}-\Sigma_{a1}} \tag{5.31}$$

$$\beta = \frac{1}{6} \frac{3\Sigma_{a1}-\Sigma_{a2}}{\Sigma_{a2}-\Sigma_{a1}} \tag{5.32}$$

$$\Sigma_{a1} = \xi_1 = \Sigma_{tr} \tag{5.33}$$

$$\Sigma_{a2} = 3\xi_1 - \frac{3}{2}\xi_2 \tag{5.34}$$

The previous analysis shows that the eigenvalues are all negative, so Eq.(5.24) provides a useful approximation to the Boltzmann scattering operator. In a deterministic setting, the operator can be used by letting

$$\psi_1 = (I-\beta L)^{-1}\psi_0 \tag{5.35}$$

and writing the transport equation as a coupled set of partial differential equations.

$$\begin{aligned}
\Omega \cdot \nabla \psi_0 + (\Sigma_t - \Sigma_{s0})\psi_0 &= \alpha L \psi_1 \\
\psi_1 - \beta L \psi_1 &= \psi_0
\end{aligned} \tag{5.36}$$

It can also be written as a Boltzmann type equation by using the following procedure. Rewrite L_2^* as

$$\begin{aligned} L_2^* &= \alpha L(I-\beta L)^{-1} \\ &= \frac{\alpha}{\beta}[I-(I-\beta L)](I-\beta L)^{-1} \\ &= \frac{\alpha}{\beta}[(I-\beta L)^{-1}-I]. \end{aligned}$$

This is a Boltzmann operator if $(I-\beta L)^{-1}$ can be written as an integral operator. This is, of course, possible since $I-\beta L$ is a second order partial differential operator. Thus, it is possible to find a Greens function $G(\Omega\cdot\Omega')$ such that

$$(I-\beta L)G(\Omega\cdot\Omega') = \delta(\Omega\cdot\Omega'-1) \tag{5.37}$$

and

$$(I-\beta L)^{-1}\psi = \int_{4\pi} d\Omega' G(\Omega\cdot\Omega')\psi(\Omega') \tag{5.38}$$

Explicitly, the Greens function for this operator is given by Larsen and Leakes as

$$G(\Omega\cdot\Omega') = \sum_{j=0}^{\infty}\frac{2j+1}{4\pi}\frac{P_j(\Omega\cdot\Omega')}{1+\beta j(j+1)} \tag{5.39}$$

This has been a demonstration of how the generalized Fokker-Planck expansion can be used to construct a regularized operator. It was also implicitly shown that the whole procedure could be done using only the first two transport moments of the DCS. The next example shows that the generalized Fokker-Planck expansion is not necessary for this process.

5.2.2 Generalized Fermi Expansion

The discussion here follows the work of Prinja[35]. In that work, it was shown that the Fermi approximation could be given by an expansion of the form

$$L_B\psi = \sum_{n=1}^{\infty} a_n \xi_n L_F^n \psi \tag{5.40}$$

$$\text{Ł}_F = \frac{\partial}{\partial \eta} + \frac{\partial}{\partial \xi} \tag{5.41}$$

where the a_n are positive coefficients in the expansion. Note that the first order approximation of L_B is the Fermi approximation given in Eq.(4.60). Higher order truncations of Eq.(5.40) give unstable solutions, much like the general Fokker-Planck expansion.

To proceed with the regularization procedure, we propose the approximate scattering operator

$$G\psi = \alpha \exp(\beta L_F)\psi - \alpha\psi \tag{5.42}$$

Then we may expand G using the Taylor series for the exponential function.

$$G\psi = \alpha\beta L_F\psi + \frac{\alpha\beta^2}{2} L_F^2\psi + O(\alpha\beta^3). \tag{5.43}$$

To get an asymptotic equivalence of $G\psi$ and $L_B\psi$, we require

$$\alpha = 2\frac{\xi_1^2}{\xi_2} \tag{5.44}$$

$$\beta = \frac{1}{4}\frac{\xi_2}{\xi_1} \tag{5.45}$$

Now we introduce the operator χ given by

$$\chi(s) = \exp(sL_F) \tag{5.46}$$

We can then write $G\psi = \alpha\chi(\beta)\psi - \alpha\psi$. Also, the following partial differential equation holds for χ.

$$\frac{\partial \chi}{\partial s} = L_F \chi \tag{5.47}$$

$$\chi(0) = I, \quad \lim_{\eta,\xi \to \infty} \chi\psi = 0 \tag{5.48}$$

This equation looks like a time dependent diffusion equation. Thus, the Greens function is well known, and the solution is

$$\chi(s)\psi = \frac{1}{4\pi s} \int_{-\infty}^{\infty} d\eta' \int_{-\infty}^{\infty} d\xi' \exp\left[-\frac{(\eta-\eta')^2 + (\xi-\xi')^2}{4s}\right] \psi(\eta',\xi') \tag{5.49}$$

Plugging this into the expression for G with $s = \beta$ gives the regularized operator.

$$L_B\psi \approx \frac{\alpha}{4\pi\beta} \int_{-\infty}^{\infty} d\eta' \int_{-\infty}^{\infty} d\xi' \exp\left[-\frac{(\eta-\eta')^2 + (\xi-\xi')^2}{4\beta}\right] \psi(\eta',\xi') - \alpha\psi(\eta,\xi) \tag{5.50}$$

We may write this in terms of the physical variable μ by using $1-\mu^2 = \eta^2 + \xi^2$ while noting that μ is nearly 1 and thus $1-\mu^2 \approx 2(1-\mu)$.

$$L_B\psi \approx \frac{\alpha}{4\pi\beta} \int_{4\pi} d\Omega' \exp\left[-\frac{1-\mu}{2\beta}\right] \psi(\Omega') - \alpha\psi(\Omega) \tag{5.51}$$

Note that this form is similar to the exponential representation of the Fokker-Planck operator. Though this is likely to be just a coincidence, it might explain why the exponential representation that we chose worked so well. In any event, we again see that the Boltzmann operator can be made asymptotically equivalent to a different operator of the Boltzmann type. However, the new operator is less singular since the scattering kernel is a smooth function at $\mu_0 = 1$.

5.3 Moment Preserving Methods

In the previous section, we saw how different operators could be made equivalent to the Boltzmann operator by equating coefficients in formal expansions. This can be a cumbersome procedure, especially if the expansions are of very high order. The moment preserving method prescribes a much easier method for making two operators equivalent up to an arbitrary order as long as the approximate operator is of the appropriate form.

5.3.1 The Exponential and Discrete Models

To be more concrete, suppose we have two operators that are of the Boltzmann type. We shall refer to them as L_{B1} and L_{B2}. If both operators are sufficiently forward peaked, then we may write

$$L_{B1}\psi = \sum_{n=1}^{N} a_n \xi_{1,n} L_F^n \psi + O(\epsilon_1^N) \tag{5.52}$$

$$L_{B2}\psi = \sum_{n=1}^{N} a_n \xi_{2,n} L_F^n \psi + O(\epsilon_2^N) \tag{5.53}$$

due to the generalized Fermi expansion. We see that, if $\epsilon_1 << 1$ and $\epsilon_2 << 1$, then these two operators are asymptotically equivalent provided $\xi_{1,n} = \xi_{2,n}$ for $n < N$. Naturally, we may let one of the operators be the Boltzmann scattering operator that we would like to approximate. The other operator could be of the same form as the approximation give in Eq.(5.51) since we already know that this form is appropriate. Then the condition for preserving the first two moments with the lower limit set approximately to $-\infty$ gives

$$\frac{\alpha}{2\beta}\int_{-\infty}^{1} d\mu \exp\left[-\frac{1-\mu}{2\beta}\right](1-\mu) = 2\alpha\beta = \xi_1$$
$$\frac{\alpha}{2\beta}\int_{-\infty}^{1} d\mu \exp\left[-\frac{1-\mu}{2\beta}\right](1-\mu)^2 = 8\alpha\beta^2 = \xi_2$$

The approximation of the lower limit poses no serious problem as long as the parameter β is found to be very small. Indeed, the solution to the two nonlinear equations given above gives,

$$\alpha = 2\frac{\xi_1^2}{\xi_2} \tag{5.54}$$

$$\beta = \frac{1}{4}\frac{\xi_2}{\xi_1} \tag{5.55}$$

which is the same solution as what was given by the renormalization procedure. This is a comforting result. Also, we see that β is $O(\epsilon)$ by our assumptions about the properties of the transport moments. Thus, setting the lower limit to $-\infty$ poses no serious problem, as expected.

From the delta function representation of the Fokker-Planck operator, we suppose that the delta function could also be of a suitable form for approximating the Boltzmann operator. Then, we have the representation

$$L_{B2}\psi = \int_{-1}^{1} d\mu\alpha\delta(\mu - (1-\beta))\psi \tag{5.56}$$

and the preservation of the first two moments gives

$$\alpha\beta = \xi_1 \tag{5.57}$$

$$\alpha\beta^2 = \xi_2 \tag{5.58}$$

and the solution to these equations is

$$\alpha = \frac{\xi_1^2}{\xi_2} \tag{5.59}$$

$$\beta = \frac{\xi_2}{\xi_1}. \tag{5.60}$$

It is interesting to see that, if we let $\xi_2 \rightarrow 0$, then we get the delta function representation of the Fokker-Planck operator. Again, this is a comforting notion.

These approximations work nicely if we only want to preserve two moments, but two moments may be inadequate. Consider two operators of the Boltzmann type

L_{B1} and L_{B2}. Then, by linearity, we may write

$$(L_{B1} + L_{B2})\psi \equiv L_{B3}\psi = \sum_{n=0}^{N} a_n(\xi_{1,n} + \xi_{2,n})L_F\psi + O(\epsilon_1^N + \epsilon_2^N) \tag{5.61}$$

$$\xi_{1,n} + \xi_{2,n} = \int_{-1}^{1} d\mu(1-\mu)^n \Sigma_{e,1}^{*} + \Sigma_{e,2}^{*} \equiv \xi_{3,n} \tag{5.62}$$

This gives us a means for stringing together an arbitrary number of approximate scattering operators. Then, we may use the same procedure as before to preserve moments with the combined operator and the Boltzmann scattering operator.

We see now that the only difference between a regularized scattering operator and the Boltzmann scattering operator is the pseudo-DCS in the integral. For the sake of transparency, we will speak only in terms of pseudo differential cross sections from here on. We introduce the exponential elastic scattering model of order $N = 2M$.

$$\Sigma_e^{*}(\mu) = \sum_{m=1}^{M} \frac{\alpha_m}{\beta_m} \exp\left[-\frac{(1-\mu)}{\beta_m}\right] \tag{5.63}$$

Also, there is the discrete elastic scattering model of order $N = 2M$.

$$\Sigma_e^{*}(\mu) = \sum_{m=1}^{M} \alpha_m \delta(\mu - (1-\beta_m)) \tag{5.64}$$

The order of the pseudo-DCS is the number of free parameters, and thus the number of moments that can be preserved. Based on the previous discussions, these models can be used to get arbitrarily high order smooth approximations to the Boltzmann scattering operator.

Since there is no change in the arguments made up to this point for the inelastic scattering DCS, then we may simply introduce the exponential and discrete inelastic scattering models of order N.

$$\Sigma^*_{in}(Q) = \sum_{m=1}^{M} \frac{\alpha_m}{\beta_m} \exp\left[-\frac{Q}{\beta_m}\right] \tag{5.65}$$

$$\Sigma^*_{in}(Q) = \sum_{m=1}^{M} \alpha_m \delta(Q - \beta_m) \tag{5.66}$$

Preserving the first $2M$ moments of the DCS using each of these representations gives the following system of $2M$ nonlinear equations to be solved.

$$\sum_{m=1}^{M} \alpha_m \beta_m^n = C(n)\xi_n \quad 1 < n < 2M \tag{5.67}$$

$$C(n) = \begin{cases} 1 & : \text{discrete} \\ 1/n! & : \text{exponential} \end{cases} \tag{5.68}$$

These equations are difficult to solve in general because they are very ill conditioned at high order. However, their solution can be linked to the classical quadrature problem. Using this idea, Sloan developed an algorithm for efficiently computing the solution to these equations for high orders[36]. For the purposes of this thesis, investigations beyond $N = 4$ will not be presented. Therefore, analytic solutions to Eq.(5.67) are known already, and Sloans algorithm is not needed. The analytic solution for $\omega_n = C(n)\xi_n$ for the elastic models and $\omega_n = C(n)Q_n$ for the inelastic models is

$$p = \frac{\omega_3 - \omega_2\omega_4/\omega_3}{-\omega_1 + \omega_2^2/\omega_3} \tag{5.69}$$

$$q = \frac{\omega_4 + \omega_2 p}{\omega_3} \tag{5.70}$$

$$\beta_1 = \frac{1}{2}\left(q + \sqrt{q^2 - 4p}\right) \tag{5.71}$$

$$\beta_2 = \frac{1}{2}\left(q - \sqrt{q^2 - 4p}\right) \tag{5.72}$$

$$\alpha_1 = \frac{\omega_1}{\beta_1} - \frac{\omega_2 - \beta_1\omega_1}{(\beta_2 - \beta_1)\beta_1} \tag{5.73}$$

$$\alpha_2 = \frac{\omega_1 - \alpha_1\beta_1}{\beta_2} \tag{5.74}$$

From the form of the exponential and discrete models, we can immediately deduce the transport physics. In each case, the total cross section becomes

$$\Sigma_t^* = \sum_{m=1}^{M} \alpha_m \tag{5.75}$$

In a Monte Carlo setting, the discrete model contains M discrete angles or energy losses that can be sampled randomly. The algorithm reduces to

$$1 - \mu,\ Q = \beta_m \quad \frac{\alpha_{m-1}}{\Sigma_t^*} < \xi < \frac{\alpha_m}{\Sigma_t^*} \tag{5.76}$$

When using the exponential model, the algorithm becomes

$$1 - \mu,\ Q = -\beta_m \ln \xi \quad \frac{\alpha_{m-1}}{\Sigma_t^*} < \xi < \frac{\alpha_m}{\Sigma_t^*} \tag{5.77}$$

In both cases, α_0 is taken to be 0 and ξ is a uniformly distributed random number in the unit interval.

These relationships give us some insight as to what the pseudo-transport physics looks like. Typically, Σ_t^* is much smaller than Σ_t. Therefore, there will be fewer collisions per unit distance in a moment preserving method. Since we have preserved transport or energy-loss moments of the DCS, we expect this to be compensated by a correspondingly larger average change of state per collision. We can quantify this by introducing the average energy loss $\overline{Q}$ and average deviation of the scattering cosine $\overline{1-\mu}$ both given by the formula

$$\overline{Q}, \quad \overline{1-\mu} = \frac{\sum\limits_{m=1}^{M} \alpha_m \beta_m}{\sum\limits_{m=1}^{M} \alpha_m} \tag{5.78}$$

To see our intuition in action, we consider the case of protons incident on a block of tungsten. Then we may compute the parameters for each of the models as a function of the proton's incident energy. Doing so gives us the data needed to compute the quantities given above. Figure 5.1 compares the mean free path obtained by using the analog DCS to the mean free path obtained by using a 4 moment exponential or a 4 moment discrete model with both elastic and inelastic scattering. From the figure, we see that there is a major increase in the mean free path for all moment preserving methods at high energies. At low energies, depending on the model and the DCS, the mean free path can actually shrink below the analog mean free path.

We can identify at least two problems in Fig.(5.1). On the one hand, inelastic pseudo differential cross sections become too large, resulting in very small mean free paths. This is culminated by α parameters actually becoming negative. We note that this doesn't happen with a two moment model, but the mean free paths will still shrink to very small values. On the other hand, elastic scattering pseudo-differential cross sections become too small, and the resulting mean free paths too large. This happens primarily because the moments of the DCS are much smaller in magnitude for elastic scattering than for inelastic scattering. Each of these difficulties will be considered in more depth soon. First, we look at the values for $\overline{Q}$ and $\overline{\theta} = \cos^{-1}(\overline{\mu})$. They are shown for both the analog DCS and the corresponding pseudo-DCS in Fig.(5.2).

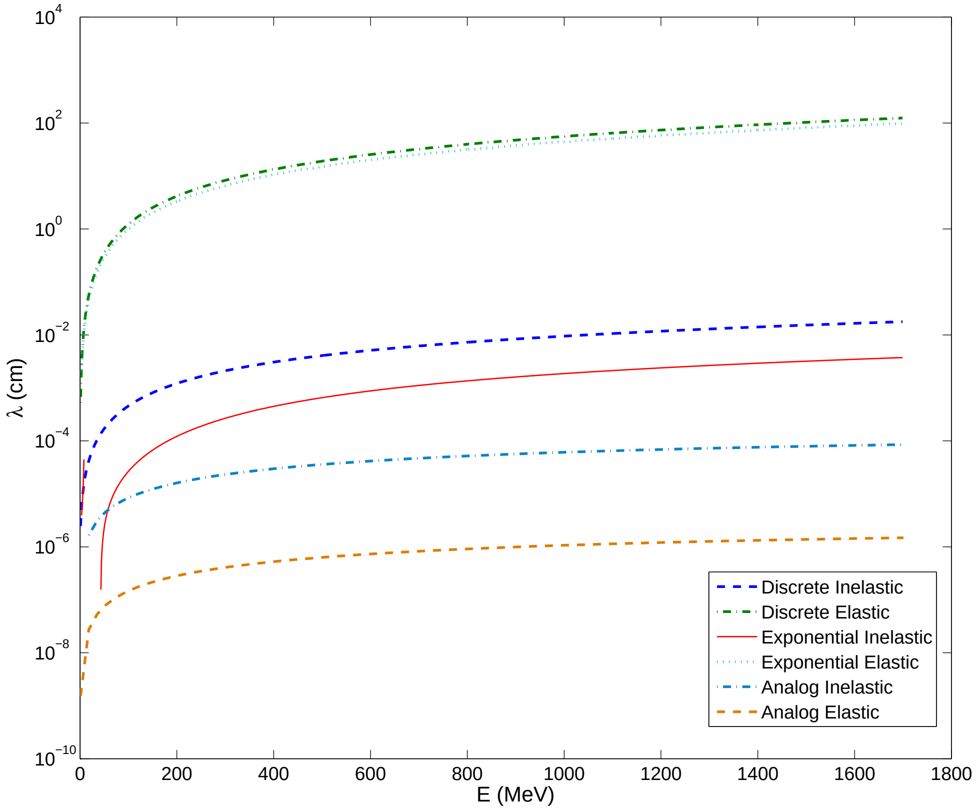

Figure 5.1: A comparison of the mean free path for the pseudo-DCS and the analog DCS for both elastic and inelastic scattering.

As was expected, the average change in the particle's state has increased for both types of scattering. Since the mean free path for elastic scattering has increased to very large values by using the pseudo differential cross section, the change in state is much larger. The scattering angles are about 10-20 degrees on average. This is much too large considering the scattering angles are about $0.01 - 0.1$ degrees per collision on average. For inelastic scattering, the energy losses per collision are also larger, but the values are physically realistic. However, at smaller energies, the average energy loss per collision decreases to the same level as is seen with the analog DCS.

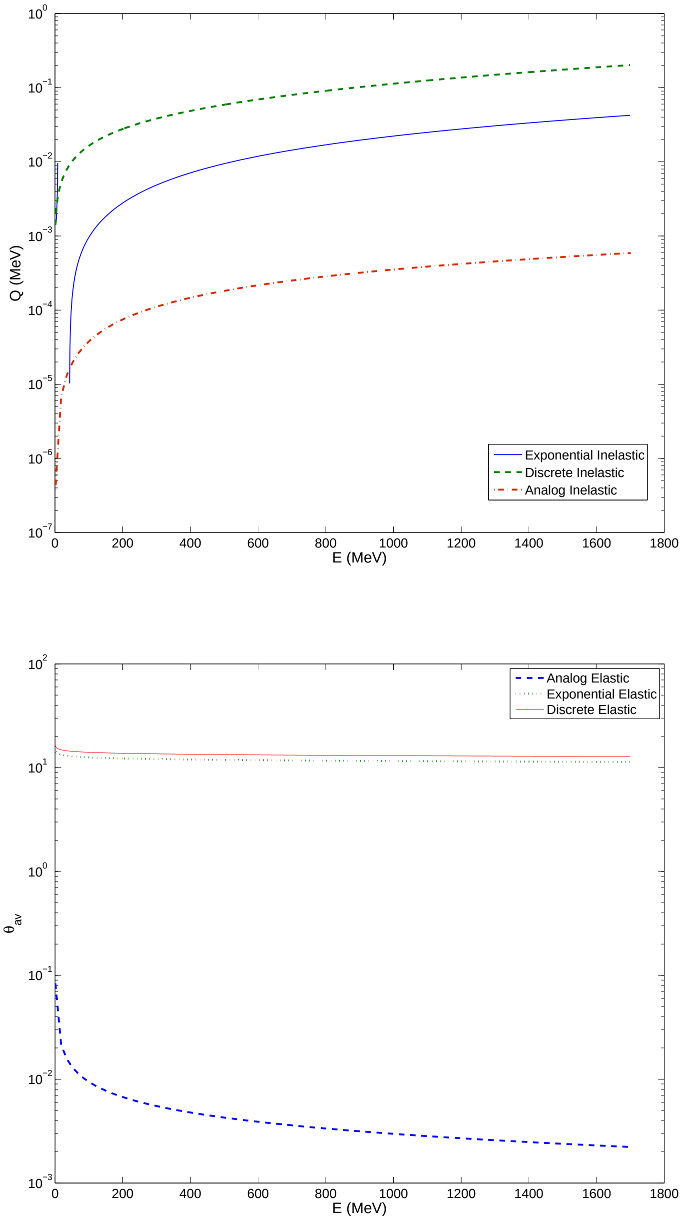

Figure 5.2: A comparison of the mean energy loss and mean scattering angle per collision for the pseudo-DCS and the analog DCS

One way to deal with the aforementioned difficulties is to use one of the equations in Eq.(5.67) to artificially set the mean free path of the approximation. In effect, for a model of order N, we may preserve the first $N-1$ moments. We consider a pseudo-differential cross section with a free parameter introduced such that

$$\alpha_M = \frac{1}{\lambda^*} - \sum_{m=1}^{M-1} \alpha_m \tag{5.79}$$

Then, we have explicitly,

$$\Sigma_e^*(\mu) = \sum_{m=1}^{M-1} \frac{\alpha_m}{\beta_m} \exp\left[-\frac{(1-\mu)}{\beta_m}\right] + \frac{1}{\beta_M}\left(\frac{1}{\lambda^*} - \sum_{m=1}^{M-1} \alpha_m\right) \exp\left[-\frac{(1-\mu)}{\beta_m}\right] \tag{5.80}$$

The last term is not of the proper form to be a renormalized cross section. Therefore, we have no rigorous backing to state that it can be used at all in the moment preserving method. Nonetheless, we may use the first $M-1$ terms to preserve the first $2M-2$ moments as usual. The next moment is also preserved, but it is done in such a way that the higher order moments may not be approximated quite as well. We will analyze this more in the next section.

The practical way to introduce a free parameter is to use Eq.(5.67) for $n < N$ and introduce the auxiliary equation

$$\sum_{m=1}^{M} \alpha_m = \frac{1}{\lambda^*} \tag{5.81}$$

We can again find an analytic solution for $M = 2$. It is

$$p = \frac{\omega_2^2 - \omega_1\omega_3}{\omega_1^2 - \omega_2/\lambda^*} \tag{5.82}$$

$$q = \frac{\omega_2 + p/\lambda^*}{\omega_1} \tag{5.83}$$

$$\beta_1 = \frac{1}{2}\left(q + \sqrt{q^2 - 4p}\right) \tag{5.84}$$

$$\beta_2 = \frac{1}{2}\left(q - \sqrt{q^2 - 4p}\right) \tag{5.85}$$

$$\alpha_2 = \frac{\omega_1 - \beta_1/\lambda^*}{\beta_2 - \beta_1} \tag{5.86}$$

$$\alpha_1 = \frac{1}{\lambda^*} - \alpha_2 \tag{5.87}$$

It is typically not useful to use this method with $M = 1$ since the degree of approximation is roughly equivalent to that of the Fokker-Planck approximation.

5.3.2 Relationship between Moment Preserving Methods and Renormalization of the DCS

Larsen and Leakes proposed a method to preserve eigenvalues of the DCS since the eigenvalues are the important player in Lewis's theorem. However, it is not difficult to show that the moment preserving method preserves eigenvalues also. Consider the eigenvalue equation for an arbitrary Boltzmann type operator.

$$L_B Y_l^m(\Omega) = \left(\Sigma_{s,l} - \Sigma_{s,0}\right) Y_l^m(\Omega) \equiv \lambda_{B,l} Y_l^m(\Omega) \tag{5.88}$$

Using the definition of $\Sigma_{s,n}$ with the finite Taylor expansion about $\mu = 1$ for $P_n(\mu)$, we get

$$\begin{aligned} \lambda_{B,l} &= \int_{-1}^{1} d\mu \left(\sum_{k=0}^{l} \binom{l}{k} \binom{-l-1}{k} \frac{1}{2^k} (1-x)^k - 1 \right) \Sigma_e(\mu) \\ &= \sum_{k=0}^{l} b_{k,l} \xi_k \end{aligned} \tag{5.89}$$

This tells us that preserving k transport moments of the DCS is equivalent to preserving k eigenvalues of the DCS.

This result is for arbitrary scattering kernels. This would imply that a wide range of pseudo-differential cross sections may be used if the higher order moments were not important. We saw in Fig.(4.1) that the higher order transport moments do not actually decay away very quickly, and in many cases they actually begin to increase for sufficiently high n.

The renormalization procedures that were introduced in the previous section help us approximate the remaining transport moments, and thus approximate the

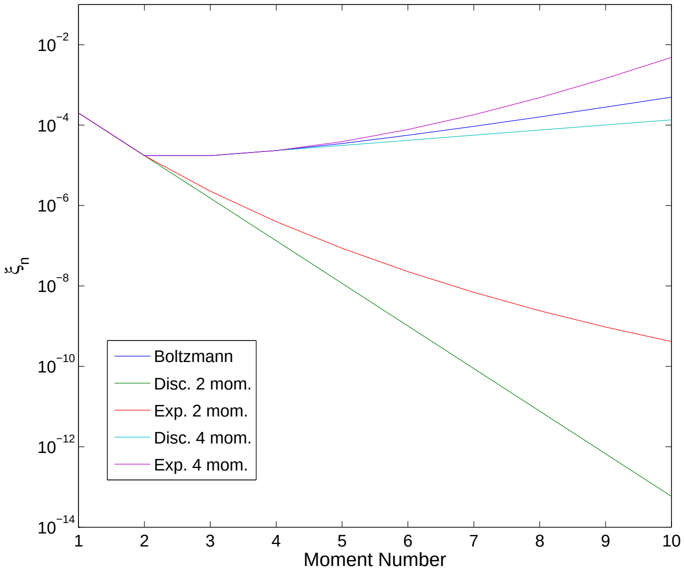

Figure 5.3: Comparison of the first ten moments of the Boltzmann DCS and the discrete and exponential model pseudo-DCS of order 2 and 4.

remaining unpreserved eigenvalues. The generalized Fokker-Planck expansion, for instance, gives a rigorous expansion of the Boltzmann operator in terms of the generalized transport moments as does the generalized Fermi expansion. The renormalized Boltzmann operator that results has expansion coefficients that approximate the true expansion coefficients for all orders greater than the order of the method N.

Figure 5.3 shows how the moments of the two moment and four moment discrete and exponential models compare to the moments of the Boltzmann operator for 1700 MeV protons incident on tungsten. We see that the unpreserved moments of our renormalized operators are indeed close to the Boltzmann moments for the four moment model. Also, the approximation of the unpreserved moments gets better for a higher order method in both cases. The higher order moments shrink to zero for the two moment models in both cases making these approximations less accurate.

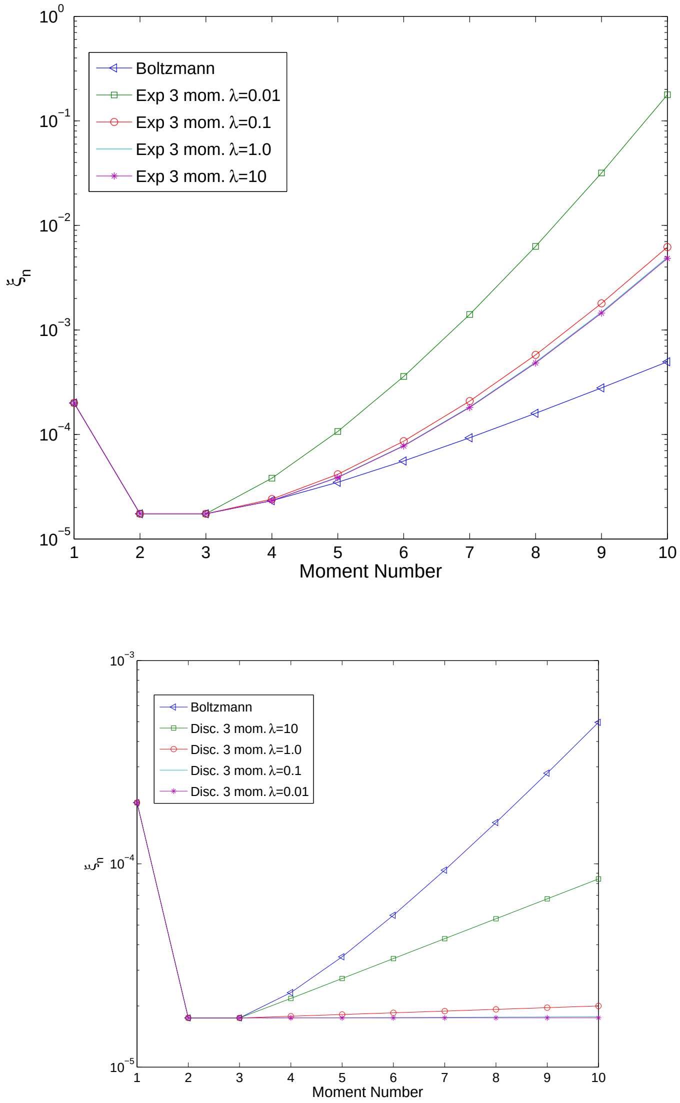

Figure 5.4: Comparison of the first ten moments of the Boltzmann DCS and the discrete and exponential model pseudo-DCS of order 3 with a varying mean free path.

It is then logical to ask how well we are approximating the higher order moments when we use the free parameter models. Figure 5.4 shows the same data as in the previous figure except with the exponential model of order 3 on the left and the discrete model of order 3 on the right with various mean free paths. With the exponential model, we see that the approximation becomes better as the mean free path is increased, thus bringing it closer to the four moment mean free path. For sufficiently large mean free paths, we see that the approximation can be worse than the two moment model approximation since it appears to cause the higher order moments to grow to arbitrarily large values when using the exponential model. This may result in unphysical properties of the three moment exponential model in the thin slab limit.

Curiously, we see that lowering the mean free path tends to make the unpreserved moments less approximate for the discrete model. On the other hand, we know that the four moment mean free path is very large. This may indicate that this model hasn't been properly renormalized. Nonetheless, it was chosen to take the form of the delta function representation of the Fokker-Planck approximation, and it will be left in this form throughout this thesis.

The relevant question becomes whether or not these higher order moments significantly effect the solution to a given problem. Recall the solution to the monoenergetic infinite medium problem given by Eq.(5.12). We see that the solution is a sum over orthogonal modes, the spherical harmonics, weighted by the exponentials

$$\psi_{lm}(s) = \exp(\lambda_l s) \tag{5.90}$$

$$\lambda_l = \Sigma_l - \Sigma_0 = -\sum_{k=1}^{l} \binom{l}{k} \binom{l+1}{k} \frac{1}{2^k} \xi_k, \quad l > 0 \tag{5.91}$$

and $\lambda_0 = 0$. The interpretation is that all initial conditions to this equation lead to an isotropic solution as $s \to \infty$. At intermediate ranges, we can analyze the relative magnitudes of the modes since a delta function source leads to equal weighting of each mode at $s = 0$. Figure 5.5 is a comparison of the eigenvalues of the discrete moment model at different orders to the Boltzmann operator eigenvalues. The eigenvalues of the Fokker-Planck operator are also included. Though all operators show at least a slow divergence in the spectra compared to the Boltzmann operator, we see that the higher order models can be very accurate up to fairly large eigenvalues.

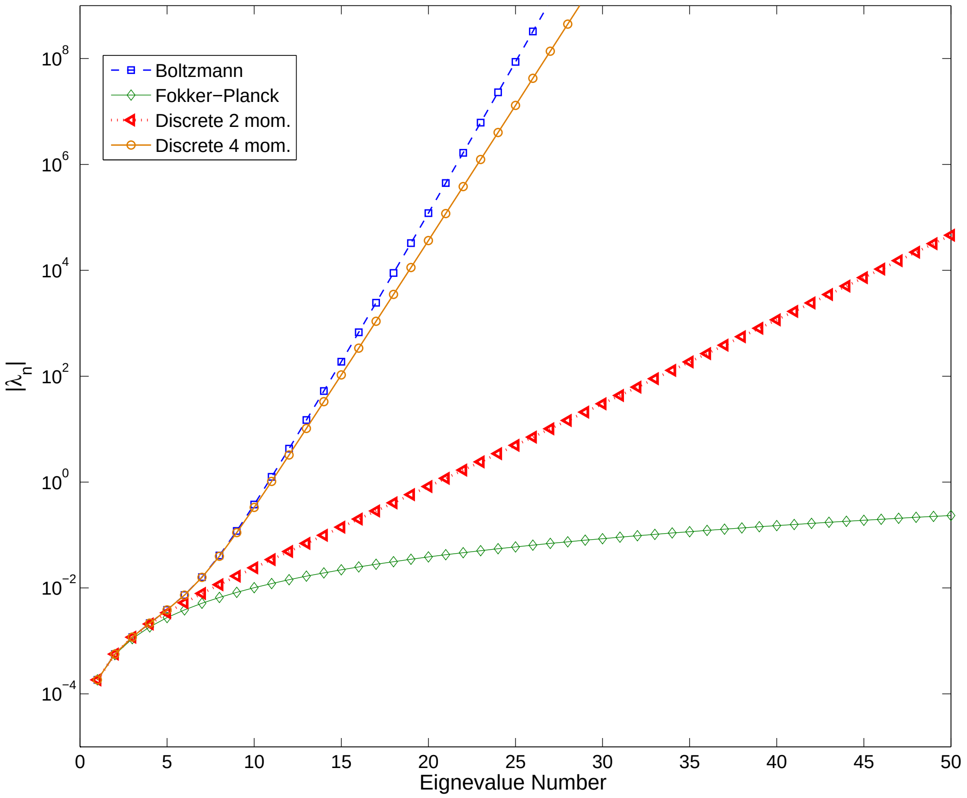

Figure 5.5: A comparison of the spectra of the various approximations to the Boltzmann operator.

As the magnitude of the eigenvalue gets larger, the corresponding mode becomes less important in the solution. To understand the error of each approximation, we can introduce the characteristic length scale of each mode defined by

$$s_n = \frac{5}{\lambda_n}. \tag{5.92}$$

This length scale assumes that the exponential has negligible value at five relaxation lengths (i.e. $e^{-5} \approx 0$). We can also define the number of important eigenvalues at a given penetration depth as

$$N(s) = n, \quad s_{n+1} < s < s_n. \tag{5.93}$$

Figure 5.6 shows how these two quantities vary for the different approximations. It is now very obvious that the Fokker-Planck model will never capture the transport physics over any reasonable range. Furthermore, the number of non-negligible modes is significantly higher at almost all length scales of interest for the 2 moment models. Only for penetrations that are on the order of the particle's range do the two moment models have similar mode contributions as the Boltzmann operator. The same arguments hold for the exponential model since the transport moments have a similar structure.

5.4 Numerical Experiments with Moment Preserving Methods

The results in this section can be broken down into three distinct categories. There are straight-ahead approximations where the angular redistribution is ignored. The corresponding transport equation for a semi-infinite medium becomes

$$\frac{\partial \psi(s,E)}{\partial s} = \int_{Q_{min}}^{Q_{max}} dQ \Sigma_{in}(Q, E+Q)\psi(s, E+Q) - \Sigma_{in,t}\psi(s,E) \tag{5.94}$$

$$\psi(0,E) = \delta(E - E_0) \tag{5.95}$$

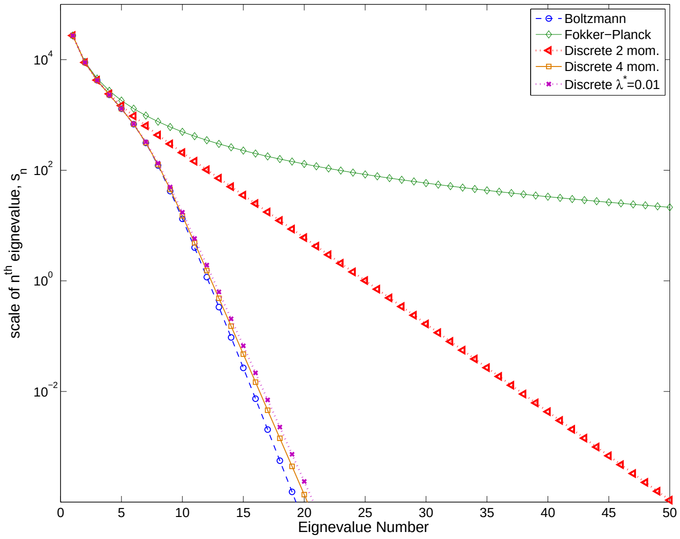

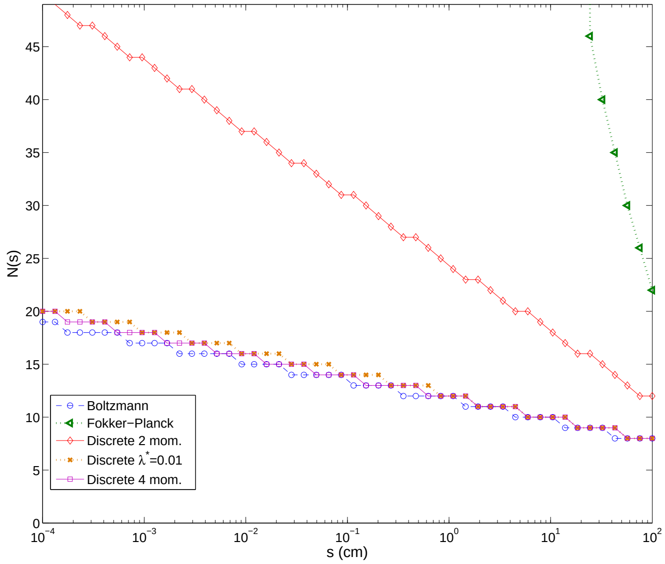

Figure 5.6: The length scale of each mode and the number of non-negligible modes for Fokker-Planck, discrete moment models, and the Boltzmann operator for 1700 MeV protons incident on tungsten.

There is also the monoenergetic approximation where the inelastic scattering is ignored. The equation is

$$\frac{\partial\psi(s,E)}{\partial s} = \int_{4\pi} d\Omega' \Sigma_e(\Omega\cdot\Omega')\psi(s,\Omega') - \Sigma_{e,t}\psi(s,\Omega) \qquad (5.96)$$

$$\psi(0,\Omega) = \delta(\mu-1) \qquad (5.97)$$

Then there is the full equation with angular redistribution and energy loss. These will each be studied in order. It should be noted that numerical experiments for electrons have been studied extensively by Harding[6, 37], Fichtl[38] and Franke[39]. Their conclusions are similar to the ones that I will give here. Thus, the focus in this section will be numerical experiments with protons.

5.4.1 Inelastic Scattering with Straight-Ahead Transport

We consider Eq.(5.94) for 1700 MeV protons incident on tungsten metal. We've used this test example for several of the figures so far, so we understand its behavior and how it relates to electrons and other ions. We first consider the very thin slab limit. Figure 5.7 compares the accuracy of each of the models when preserving both two and four moments. From the figure, we see that the two moment model gives very inaccurate results. The four moment exponential model is much more accurate, confirming our notion that the moment preserving methods work better when more moments are preserved. However, the error in the method is apparent even for the four moment model. Furthermore, the mean free path decreases when more moments are preserved. Further increasing the number of moments will lead to marginal gains but larger run times.

Also, the drawback of the discrete model is apparent in the thin slab limit. The discrete model cannot be used for thin slabs due to the appearance of discrete artifacts. They only show up due to the deterministic nature of the approximate

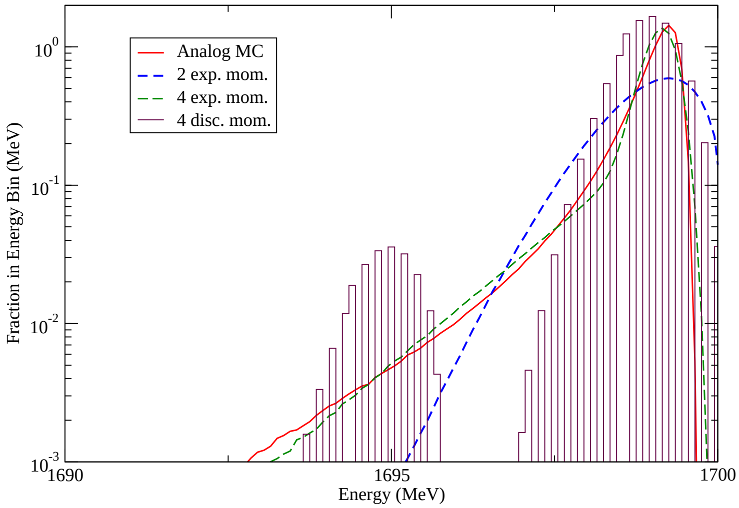

Figure 5.7: Results for exponential and discrete models of order 2 and 4 for a 0.1 cm thick medium.

scattering process. Fortunately, the discrete artifacts disappear when thicker media are encountered.

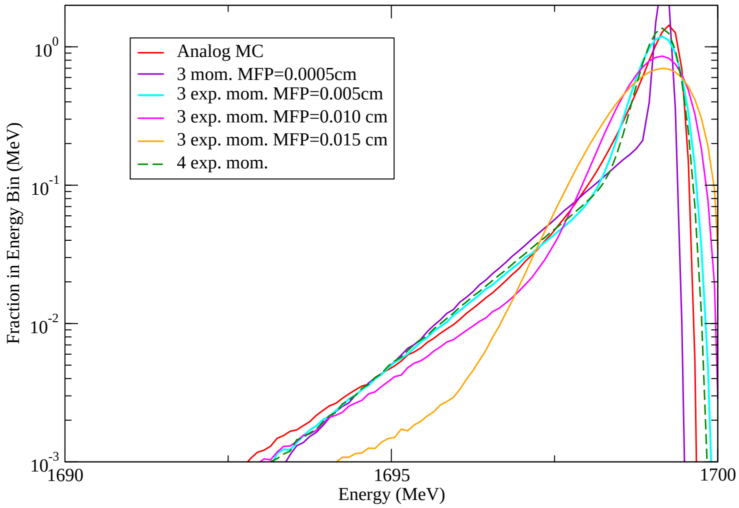

Figure 5.8: A comparison of the three moment models with varying mean free path for protons incident on 0.1 cm of tungsten.

Figure 5.8 shows the same test case for the three moment model with a free

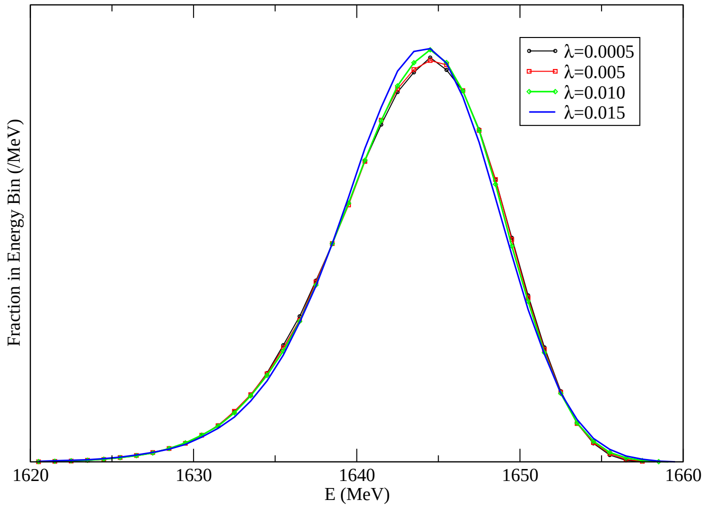

Figure 5.9: A comparison of the three moment models with varying mean free path for protons incident on 5.0 cm of tungsten.

parameter, dubbed simply the three moment model. We see that the accuracy of the model increases as the mean free path decreases toward 0.005 cm. As the method becomes more accurate, the solution tends toward the four moment model. Since this is a very thin penetration, we see that the inaccuracy of the higher order moments tend to give widely varying solutions based on the mean free path. From our earlier discussion, we would expect to see this variation disappear for larger penetrations. Indeed, Fig.(5.9) shows that the variation is mostly gone at a depth of 5 cm.

For deeper penetrations, the solutions tend toward the analog solution. This can be seen in Fig.(5.10) where the penetration depth is 5 cm on the bottom and 20 cm on the top. Only the 2 moment models fail to capture the solution over the interesting range of energies. The three moment model captures the solution well since it is close to a four moment model. We also see the exact solution to the Fokker-Planck energy loss model in the 20 cm case. It appears to coincide with the 2 moment model which is consistent since this model requires both the stopping power and straggling coefficient, Q_1 and Q_2.

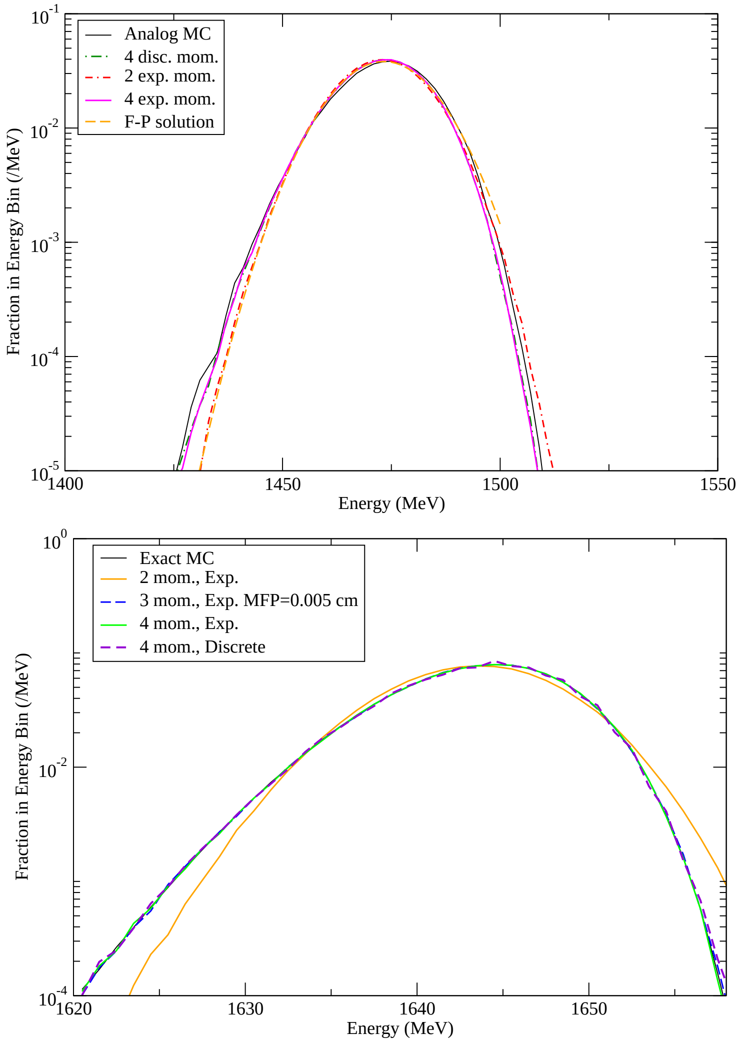

Figure 5.10: Results for exponential and discrete models of order 2 and 4 for a 5.0 cm and 20.0 cm thick media.

We've seen that two moment models appear to work better as the penetration depth increases. Since many applications only require knowledge of the dose distribution, it is logical to ask if the two moment model is sufficient for dose calculations. Figure 5.11 shows that this is indeed the case. The results are compared with a continuous slowing down run. We see that the CSD run leads to a very sharp peak while higher order approximations lead to a much smoother, less pronounced peak. The

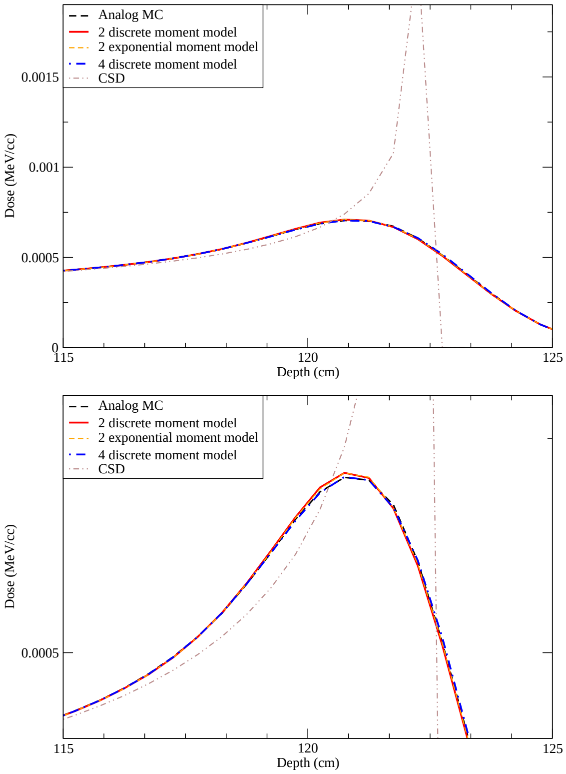

Figure 5.11: Dose results for protons incident on tungsten metal using a CSD approximation, moment preserving models, and an analog model.

moment preserving models all work well in reproducing the dose distributions. Only at the peak of the curve do the two moment models produce slight errors compared to the analog.

To analyze the relative efficiency of the moment preserving models over the analog method, we introduce the speedup defined by

$$\tau = \frac{t_{\text{approx.}}}{t_{\text{analog}}} \tag{5.98}$$

The speedup for each of the test cases shown so far are given in Table 5.1. The loss in speedup with larger penetration depths is clearly due to the sharp increase in mean free path. The worst case is found with the four moment exponential model, where the speedup is barely greater than one. This can be remedied by using a three moment model. However, at small energies, the three moment model can give negative parameters. Thus, we are left without a clear reliable method for keeping the mean free path from blowing up.

Test Case	**Speedup**			
	2 mom. disc.	2 mom. exp.	4 mom. disc.	4 mom. exp.
0.1 cm	647	488	485	152
5.0 cm	82.2	41.8	37.6	8.1
20.0 cm	63.9	37.3	33.1	8.1
Dose	24.2	11.9	11.5	1.4

Table 5.1: Speedup of moment preserving methods over the analog method for straight ahead transport.

5.4.2 Monoenergetic Elastic Scattering

Much like the straight ahead transport model, the monoenergetic elastic scattering transport model allows us to isolate the approximation and study its accuracy without the influence of the other physics. As mentioned earlier, the problems encountered when using a moment preserving methodology with elastic scattering is that the mean free paths become very large. We can see this by consider the mean free path for a two moment model from Eq.(5.54)

$$\lambda = \frac{\xi_2}{C(2)\xi_1^2}. \tag{5.99}$$

For inelastic scattering, this resulted in physically reasonable mean free paths at large energies, and very small mean free paths and small energies. Since Σ_{tr} is $O(10^{-4})$ and ξ_2 is $O(10^{-5})$ for the applications of interest to us, the resulting mean free path is very large. In fact, it is of the same order of magnitude as the proton's range for very high energy protons incident on tungsten based on data given by Janni[40].

The result of dealing with this difficulty is that we require the use of the free parameter model in order to generate physically reasonable results. On the other hand, we are using the model to tune the mean free path down instead of up. The extent of the difference between λ^* and the mean free path that preserves exactly four moments is large enough that we expect the three moment model to only preserve three moments rigorously.

Preliminary tests using the three moment model showed that adjusting the mean free path in the range of 0.001 up to 0.1 resulted in identical angular distributions. Therefore, the selection of the mean free path is mostly arbitrary up to this point, and λ^* was chosen to be 0.01 for all of the results presented here. Figure 5.12 and Figure 5.13 show how the angular and radial distributions converge with decreasing mean free path. The test cases for these figures were identical to the test cases used to do the similar study with the Fermi model shown in Fig.(4.7) to Fig.(4.10).

The total cross section for those two test cases was $\Sigma_t = 44000$ and the transport cross section was $\Sigma_{tr} = 2 \times 10^{-3}$ in the first case and $\Sigma_{tr} = 2 \times 10^{-5}$ in the second case. In both cases, the penetration distance was 10 cm. From Fig.(5.12) we see that the previous statement is confirmed. A significant discrepancy between the results doesn't occur until the mean free path of the moment preserving method rises above 0.1. The same result is obtained in the second case when angular and radial spreading is much smaller. The indication is that the convergence, like in the case of the Fermi distribution, depends more on the length scale of the problem and is nearly independent of the relative magnitude of the scattering parameters. Fig.(4.7) to Fig.(4.10).

Unlike the Fermi distribution, we see that the angular distribution convergence is highly correlated with the radial distribution convergence. The interpretation that will prevail over the course of this section is that the accuracy of the angular distribution is indicative of the accuracy of the radial distribution. The next few

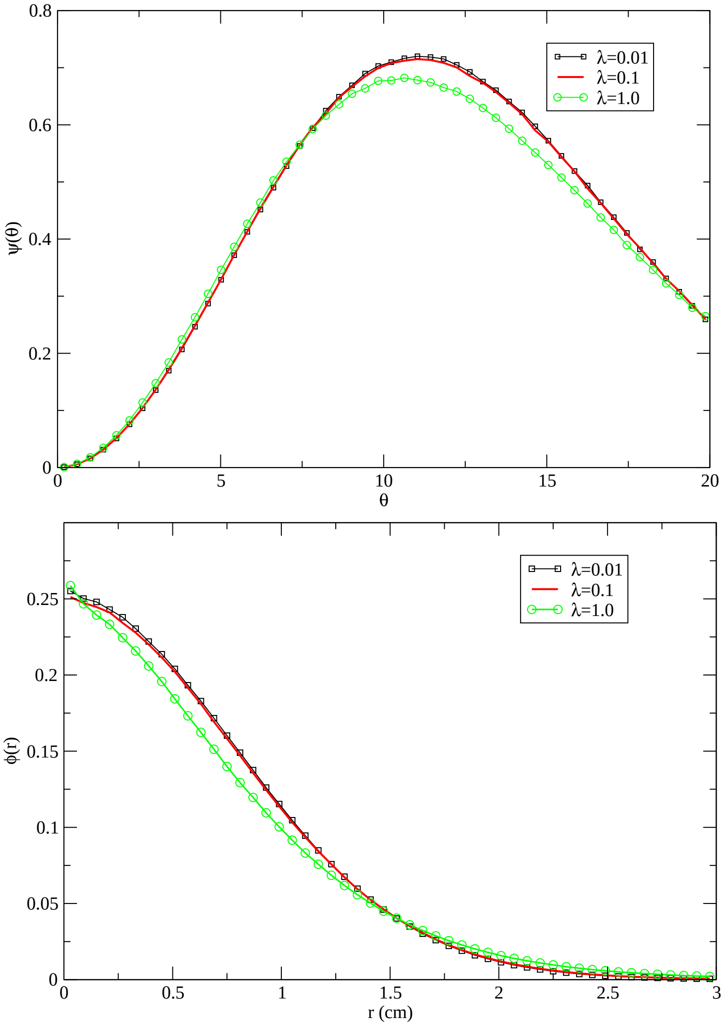

Figure 5.12: Convergence of the exponential model of order 3 for varying mean free path with $\Sigma_t = 44000$ and $\Sigma_{tr} = 2 \times 10^{-3}$

results will solidify this hypothesis. The intuitive reason why the moment preserving methods have correlated radial and angular distributions is that, when we preserve angular moments of the solution, we are preserving the same number of spatial moments of the solution too.

The same hypothesis does not hold for the Fermi distribution because of the fixed step that is introduced and the lack of radial correcting of the method that we have

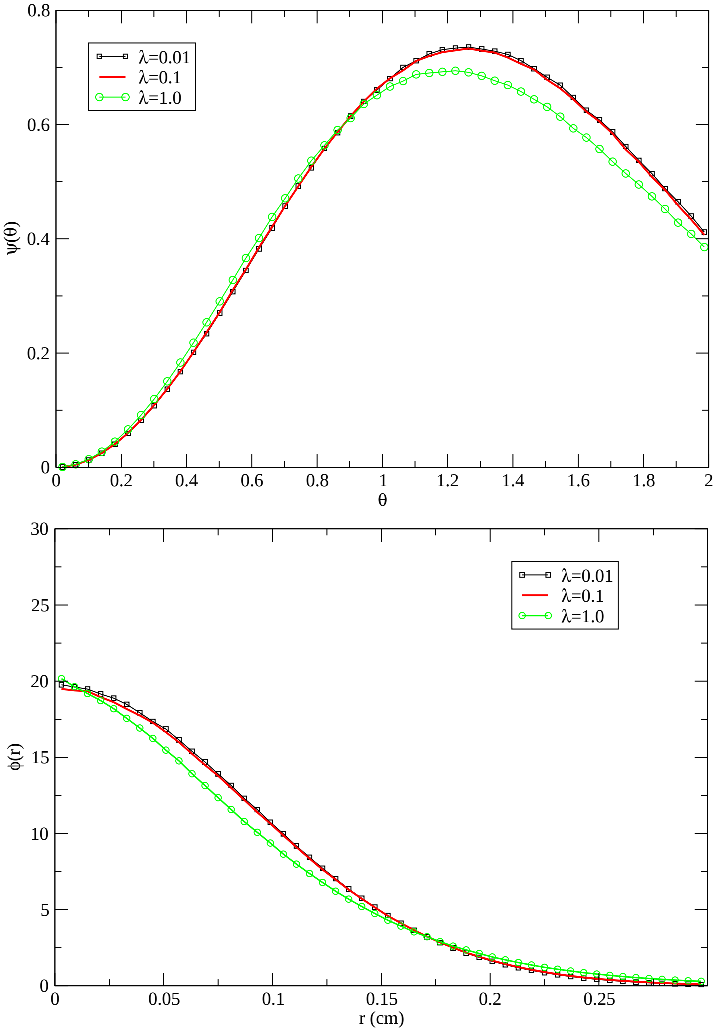

Figure 5.13: Convergence of the exponential model of order 3 for varying mean free path with $\Sigma_t = 44000$ and $\Sigma_{tr} = 2 \times 10^{-5}$

presented. In this context, it is much like the methods used in modern condensed history. The reliance is on the angular distribution being sampled often enough that the radial distribution is nearly correct over long distances. However, even in the absence of of other approximations, the Fermi model will have an increasing error with larger penetrations that is $O(\Delta s)$, much like a discretization error in deterministic methods.

The accuracy of the Fokker-Planck approximation was considered earlier, and much of the discussion stemmed from the work of Larsen and Börgers[25]. Their work became a benchmark on the accuracy of the code developed for this research. In their paper, they considered parameters typical of high energy electrons incident on a semi-infinite medium of water. Thus, they used $\Sigma_{tr} = 0.05$ and $\Sigma_t = 11000$. Working backwards, this corresponds to $K = 3.41 \times 10^{-3}$ and $\eta = 1.55 \times 10^{-7}$ in Eq.(3.32). The results that they obtained matched our results perfectly. They are shown in Fig.(5.14) along with the discrete and exponential models of order 3.

On the left, we have the radial distributions of particles from the center of the incident beam. On the right, we have the angular distribution normalized to the differential $\psi(\theta) = 2\pi \sin\theta \;\; \Theta(\theta)$. We see that the moment preserving methods give slightly better solutions for both distributions. This is implicitly due to Lewis's space-angle moments theorem. We preserve more moments of the solution by getting more eigenvalues correct indirectly through the transport moments of the DCS. It is no surprise that a two moment model correctly preserves more transport physics than the Fokker-Planck model.

The important thing to carry forward from the previous figure is that, for electron physics, the Fokker-Planck method has very poor accuracy, and the three moment models are only slightly better. The logical question to ask is if similar results are obtained for heavier charged particles. Figure 5.15 is a reproduction of Fig.(4.13) with the moment preserving results overlaid on the other results. We recall that this result was for 1000 MeV protons on 1 cm of tungsten metal.

We see that Fig.(5.15) is similar to Fig.(5.14) structurally. Again, the moment preserving methods do slightly better at approximating the analog solution than the Fokker-Planck method. However, now we see that the distribution due to Rossi is apparently better than the moment preserving methods. This apparent improvement is only due to the neglect of large angle scatter implicit in the Rossi distribution.

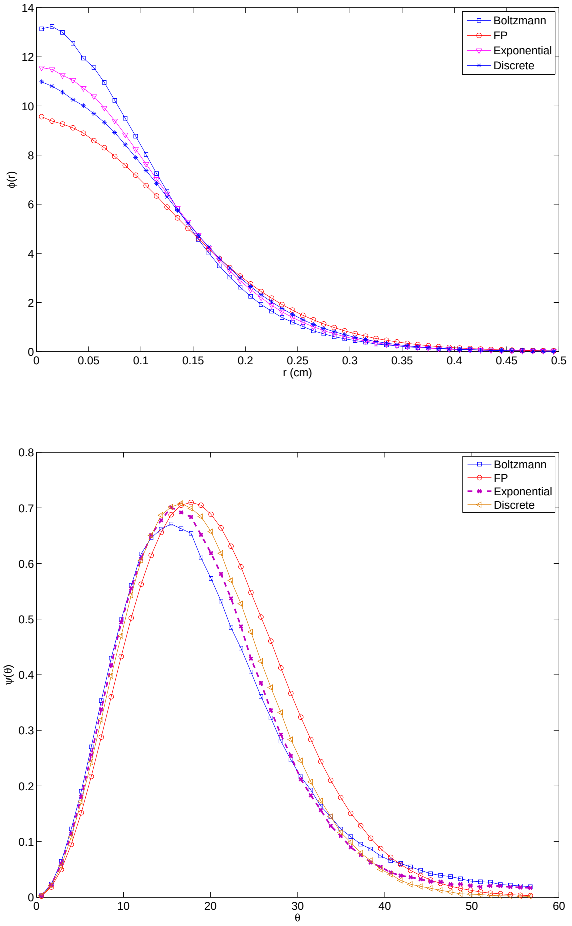

Figure 5.14: A comparison of the moment preserving methods with the Fokker-Planck model and the analog model for the benchmark problem.

Therefore, we artificially remove particles from the tail of the distribution and put them into the peak of the distribution. This procedure cannot possibly have the appropriate deep penetration solution because it is tantamount to setting the first moment, Σ_{tr} to a smaller value.

We consider successively deeper penetrations as a purely academic exercise. Obviously, the loss in energy due to inelastic collisions will render the results invalid since the energy effects of K and η will creep into the analog solution. However,

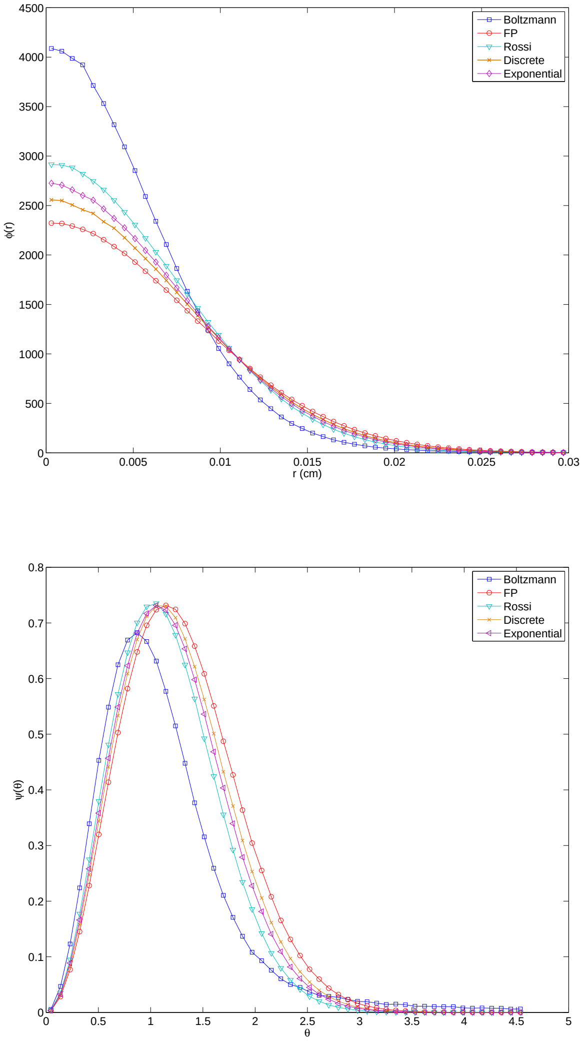

Figure 5.15: A comparison of the moment preserving methods with the Fokker-Planck model, Rossi's model, and the analog model for 1000 MeV protons incident on 1cm of tungsten.

it is a useful limiting case to consider. Figure 5.16 shows the angular distributions obtained for the moment preserving methods, the Fokker-Planck method and the analog method with a penetration of 20 cm. Figure 5.17 and Figure 5.18 are the results obtained for these methods as well as the method due to Rossi for depths of

100 cm and 200 cm respectively. Since the analog method is very expensive, its result was not obtained for the 200 cm penetration. It is not a stretch to believe that the moment preserving method is no worse at approximating the result for the 200 cm penetration then it is for the 100 cm penetration. In each case, we are considering 1700 MeV protons incident on tungsten.

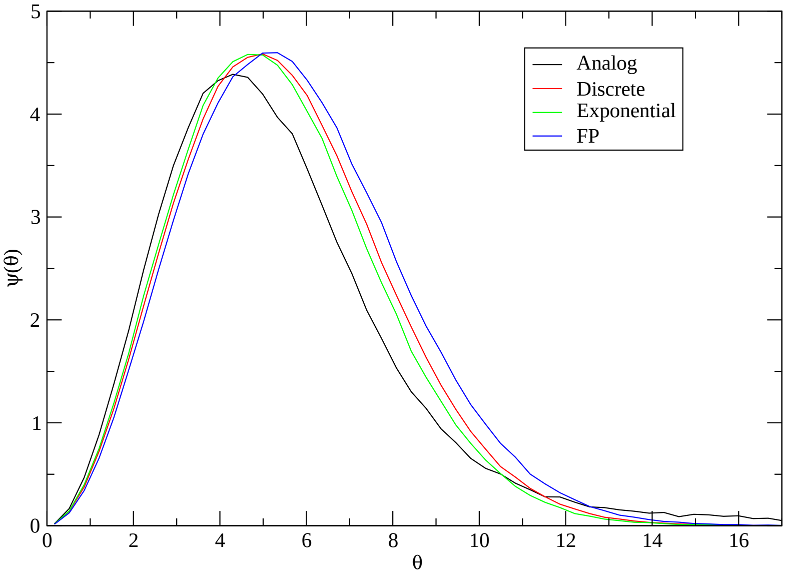

Figure 5.16: Analog and moment preserving results for 1700 MeV protons incident on 20 cm of tungsten.

As noted before, the Rossi distribution doesn't give accurate results for very deep penetrations because of its neglect of the large angle scattering. In Fig.(3.7), we see that the large angle scattering will play a role with most particles within 100 cm of penetration for the example problem given here. On the other hand, the moment preserving methods have the appropriate limit for large penetrations. However, there is still a significant discrepancy between the moment preserving solutions and the analog solution, even at 100 cm. Nevertheless, they are still much more accurate than the Fokker-Planck solution at the same depth.

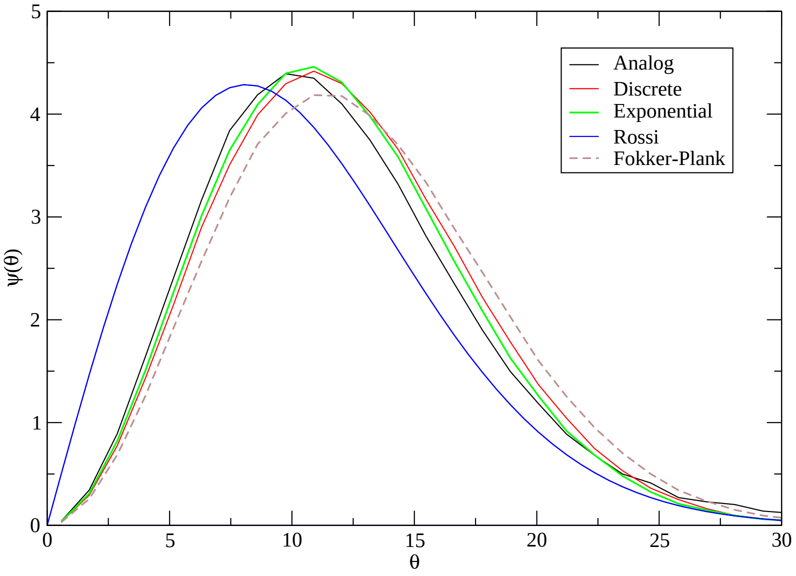

Figure 5.17: Analog and moment preserving results for 1700 MeV protons incident on 100 cm of tungsten.

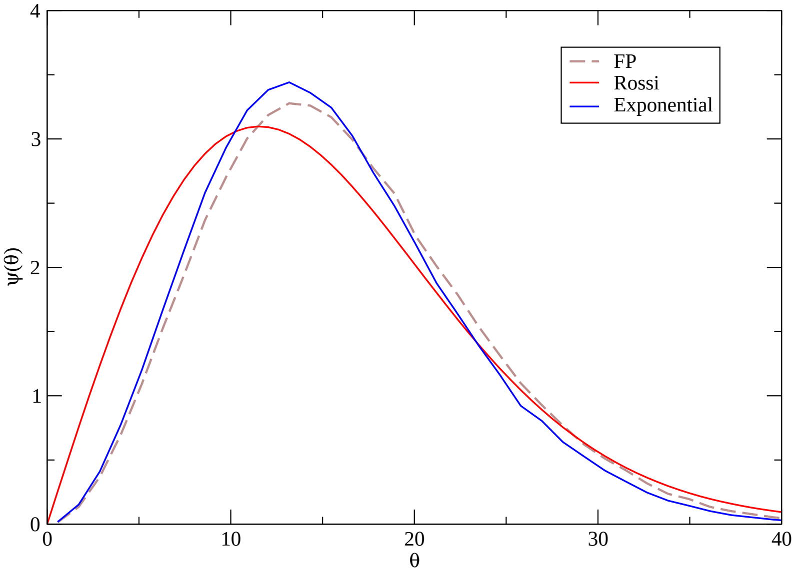

Figure 5.18: Moment preserving results for 1700 MeV protons incident on 200 cm of tungsten.

5.4.3 Results for Elastic and Inelastic Combined Scattering

Due to the decomposition of energy-loss and angular spreading, there are relatively few new issues to discuss for a combined treatment of inelastic and elastic scattering. The most important issue to address is the relative frequency of inelastic and elastic scattering. This issue is relevant to condensed history algorithms too. They have found empirically that roughly 100 angular redistribution substeps are required per energy straggling step in the MCNP5 handling of electron transport. We will investigate the necessity of this type of handling with moment preserving methods.

Assuming that the performance of the moment preserving methods holds for problems of different energy (while remaining monoenergetic problems), the whole problem can be thought of as streaming with scattering and no energy-loss covered by the discussions on monoenergetic transport and relatively infrequent energy-loss collisions. This interpretation assumes that elastic scattering is the dominant process. In Fig.(5.19), we see that this is the case since the ratio of the elastic to the inelastic total cross section is greater than 50 at all energies for protons and heavier particles. The ratio remains fairly constant for very large ranges of energies, and changes very little with the size of the incident ions. At lower energies, the ratio increases very sharply. However, we recall that at this range of energies, the Rutherford scattering model begins to lose its validity.

There is no reason to believe that we should preserve this ratio in our moment preserving approach since the total cross section doesn't enter anywhere into the theory. However, we see that elastic and inelastic scattering can be linked through the the spatial spreading of the beam. On the one hand, a decrease in energy tends to increase average scattering angles at discrete elastic collisions and thus spatial spreading of the beam over small distances. On the other hand, increased spatial spreading makes the effective path length of the particle grow as compared to the

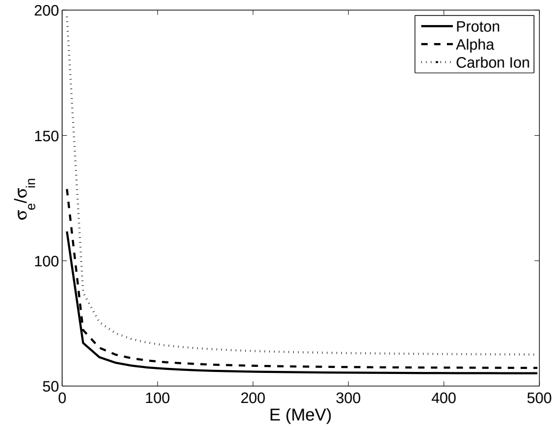

Figure 5.19: Ratio of elastic total cross section to inelastic total cross section for protons, alpha particles, and carbon ions for energies below 500 MeV.

straight-ahead transport model. This will lead to more inelastic collisions and hence more energy loss.

Unfortunately, the result due to Lewis that we've relied so heavily on thus far does not hold for the combined problem. We have seen that as λ^* gets very small for the three moment model in the elastic problem, the spatial distribution for the pseudo-transport problem converges to some distribution at a given penetration. We may also say that, in the limit as $\lambda_e \rightarrow 0$, for fixed λ_{in}, we arrive at a problem equivalent to monoenergetic transport in between inelastic collisions. Therefore, we conclude that we can resolve the appropriate spatial spreading between inelastic collisions if we at least let $\lambda_e^* << \lambda_{in}^*$. At this point, it becomes important to understand how small $\lambda_e^*/\lambda_{in}^*$ needs to be since smaller mean free paths lead to larger run times.

To study this effect, we consider the 5 cm penetration with both elastic and inelastic scattering. To keep consistent with the previous analysis of this problem, we will use a four moment discrete model for inelastic scattering and a three moment discrete model for elastic scattering. The energy spectrum results for varying $\lambda_e^*/\lambda_{in}^*$ are shown in Fig.(5.20) and the angular distributions are shown in Fig.(5.21).

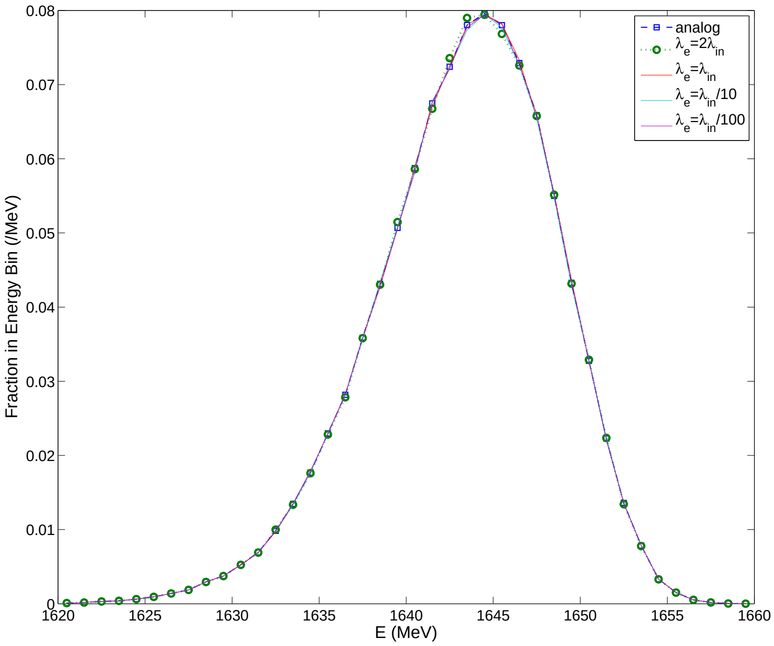

Figure 5.20: Energy spectra for 1700 MeV protons incident on 5 cm tungsten using the analog method and the discrete method of order 3 with varying $\lambda_e^*/\lambda_{in}^*$.

The surprising result is that the solution changes very little with varying λ_e^*. Only when the elastic mean free path increases above the inelastic mean free path does the angular distribution begin to deviate from the limiting distribution (i.e. distribution for $\lambda_e^* \rightarrow 0$). The energy distribution is less effected by the changing mean free path. This is likely due to the loose coupling between the inelastic cross section and the angular spreading effects. That is, the energy spectrum is effected by a larger effective range due to the radial spreading and this larger range is effected only slightly by the changing mean free path of the elastic scattering. We will consider the combined effect more in the next chapter. For now, it suffices to say that the mean free path of the elastic and inelastic scattering cross section is roughly uncorrelated at higher energies.

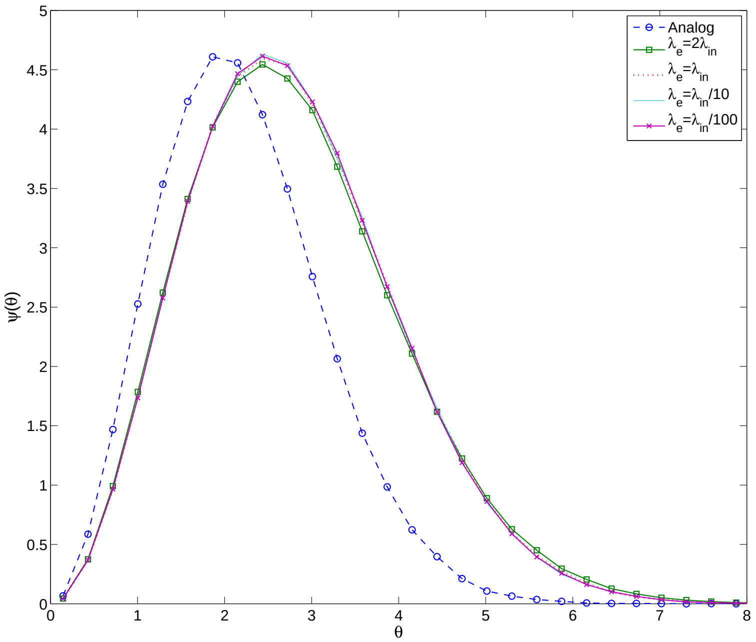

Figure 5.21: Angular spectra for 1700 MeV protons incident on 5 cm tungsten using the analog method and the discrete method of order 3 with varying $\lambda_e^*/\lambda_{in}^*$.

5.5 Moment Preserving Summary

We have seen that moment preserving methods can be a powerful way of simulating highly peaked process in high energy charged particle transport physics efficiently. However, the method suffers from an inability to reliably provide physically reasonable mean free paths or even physically valid mean free paths. This is due to the very large or very small parameters that result from solving the system of equations in Eq.(5.67). In some cases, the equations can even give negative parameters when more than one pseudo-DCS is used. The three moment model can help mitigate problems such as these, but it suffers from negativity in the parameters as well.

Also, we find that the elastic scattering DCS is still very difficult to model with the moment preserving methods. The reason is that the large angle scattering tail falls off very slowly. We saw that this was an issue for the Fokker-Planck model as well. It became clear in this chapter that this difficulty stemmed from the higher eigenvalues of the operators that were not being rigorously preserved. To get a good enough approximation over the ranges of interest for elastic scattering, as many as 25 moments would need to be preserved. Of course this is possible with the moment preserving method, but it would defeat the purpose of the approximation because the mean free path of the moment preserving cross sections would shrink to values comparable to the mean free path of the analog DCS.

As with the Fokker-Planck approximation, the conclusion is that the moment preserving method cannot be used by itself for elastic scattering. The intuitive reason is that the non-negligible large angle scattering is accounted for only by a slight increase in the average scattering angle, the average squared scattering angle, and so on. The result is to overestimate the scattering and radial spreading at shallow depths. In order for the distributions of the moment preserving method to converge to the distributions of the analog method, we need to let the particles penetrate deep enough so that the analog distribution can “catch up” to the moment preserving distribution. We will now consider ways in which we can speed up the convergence of the approximation without sacrificing computing time by preserving more moments.

Chapter 6

Hybrid Methods

The object of developing a hybrid method is to isolate the problematic portion of the DCS and treat it by another means. In our current problem, we have seen that the problematic portion is likely due to the large angle scattering tail of the DCS. Thus, the investigations of this chapter will focus on the isolation of the tail of the scattering distribution, often dubbed the smooth part, from the forward peaked portion of the scattering distribution, called the singular part.

Early attempts to isolate the smooth part of the distribution led to the successful Boltzmann Fokker-Planck operator. A thorough investigation of this first attempt will be analyzed in detail so that we may understand what further work may need to be done beyond this approximation. We will use this method as a starting point for the generalized Boltzmann Fokker-Planck approximation. Other hybrid methods will also be considered. Again, the focus will be on the elastic scattering of heavy ions. Hybrid methods for electrons have been treated extensively by other researchers, and their work won't be repeated here. Also, we have seen that moment preserving methods alone are sufficient for treating the energy loss of protons and heavier particles at high energies. Though hybrid methods are likely to be more accurate for inelastic scattering, the importance of treating inelastic scattering is not as high as the importance of treating elastic scattering.

6.1 DCS Decomposition Methods

We may expand the integral term of Eq.(5.96) to obtain

$$\begin{aligned}\frac{\partial\psi(s,E)}{\partial s} &= \int_0^{2\pi} d\theta' \int_{-1}^{\mu^*} d\mu_0 \Sigma_e(\mu_0)\psi(s,\Omega') \\ &+ \int_0^{2\pi} d\theta \int_{\mu^*}^{1} d\mu_0 \Sigma_e(\mu_0)\psi(s,\Omega') - \Sigma_{e,t}\psi(s,\Omega). \end{aligned} \tag{6.1}$$

If we let μ^* be very close to 1, then the first integral represents the smooth part of the scattering DCS and the second integral represents the singular part. In a cutoff approximation, we treat the smooth part exactly and we use an appropriate approximation for the singular part. It seems intuitive that the approximate operators from the last chapter should work well for approximating the singular part of the DCS.

Let $1-\mu^* = 10^{-5}$ as an example. Then, we may plot the moments of the singular part of the DCS for protons incident on tungsten. The results are shown if Fig.(6.1). The cutoff moments now fall much more quickly with moment number then before. Indeed we may show that the cutoff DCS moments, ξ_n^* will never start increasing as $n \to \infty$. This is exactly the sort of limit that we are considering when we use the Fokker-Planck approximation.

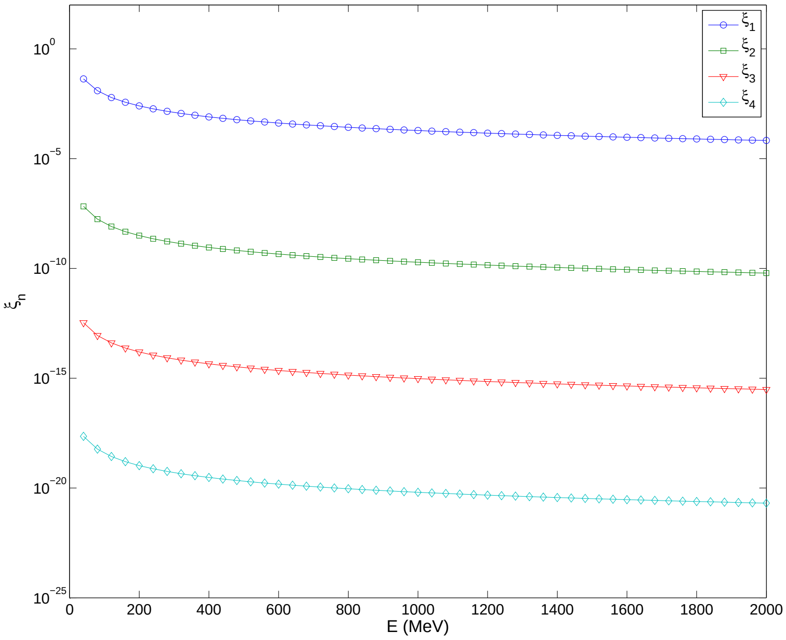

Figure 6.1: Cutoff transport moments, ξ_n^*, for protons incident on tungsten with $1-\mu^* = 10^{-5}$

6.1.1 Boltzmann Fokker-Planck Approximation

The most widely used hybrid approximation is the Boltzmann Fokker-Planck equation. For this approximation, we have

$$\frac{\partial \psi(s,E)}{\partial s} = \frac{\Sigma_{tr}^*}{2}\nabla_\Omega^2 \psi(s,\Omega) + \int_0^{2\pi} d\theta' \int_{-1}^{\mu^*} d\mu_0 \Sigma_e(\mu_0)\psi(s,\Omega') - \Sigma_{t,e}^*\psi(s,\Omega) \quad (6.2)$$

with

$$\Sigma_{t,e}^* = \int_{-1}^{\mu^*} d\mu \Sigma_e(\mu) \quad (6.3)$$

$$\Sigma_{tr}^* = \int_{\mu^*}^{1} d\mu (1-\mu)\Sigma_e(\mu) \quad (6.4)$$

This method has been used successfully in place of the Fokker-Planck approximation. Since this equation treats the large angle scattering exactly, the Fokker-Planck operator is left to treat a scattering operator that falls off much more quickly. Thus, its validity is often not questioned for this approximation.

Recall the error in using the Fokker-Planck operator given in Eq.(4.25).

$$L_B\psi(\Omega) - \nabla^2_\Omega \psi(\Omega) \propto \frac{\mathrm{var}(\mu_0)}{1-\overline{\mu}_0} \tag{6.5}$$

We saw that this error fell off very slowly with decreasing $\overline{1-\mu_0}$. In particular, the value given by Eq.(6.5) for our test problem, 1700 MeV protons incident on tungsten where $1-\overline{\mu}_0 \approx 10^{-9}$ is about 0.1. Figure 6.2 shows how the leading order error behaves for this same test problem as a function of $1-\mu^*$. From the figure, it is clear that the error of the Fokker-Planck approximation falls off much more quickly. This is to be expected since the singular part falls off infinitely fast at $\mu = \mu^*$.

The trade-off that is introduced with varying μ^* is the amount of time required to simulate the smooth part of the DCS as $\mu^* \to 1$. Figure 6.3 shows how the mean free path varies with increasing μ^*. If we require a mean free path that is $O(10^{-2})$ at the energy ranges shown in the figure, we see that we can only let $1-\mu^* \geq 10^{-5}$ at lower energies and $1-\mu^* \geq 10^{-7}$ at higher energies. Using these values for μ^* would apparently result in a small truncation error if we use Fig.(6.2) as a guide.

Even if we are happy with this prescription, there is no reason why we couldn't use a higher order approximation for the singular part of the DCS. In fact, it seems necessary to use a higher order approximation to obtain an equal or lower error if we require a reduction in μ^*. There is no reason to believe that the mean free path will not increase to unacceptably high values for certain energies or for other particles.

Indeed, we have seen that larger ions and lower energies lead to larger mean free paths for the analog DCS. The scattering is more forward peaked also, but we have seen that this does not mean the Fokker-Planck approximation is more accurate.

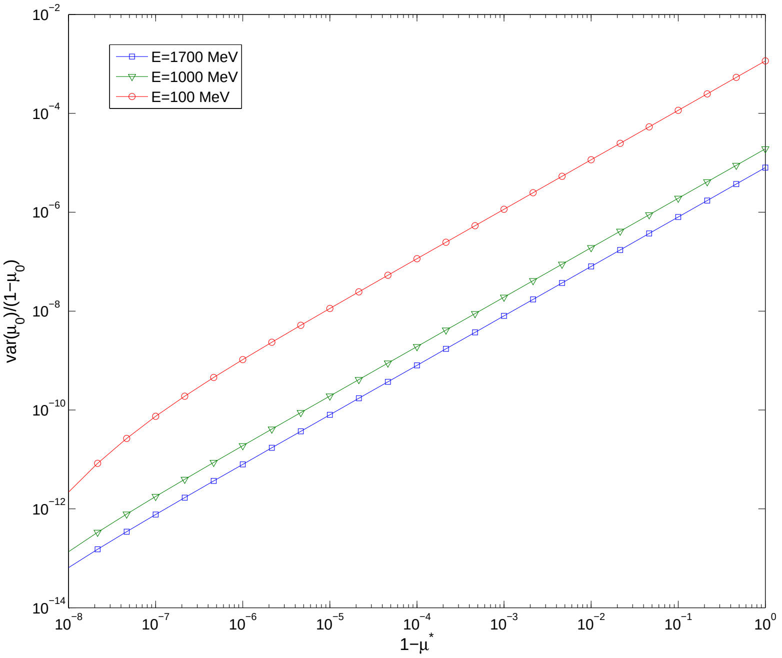

Figure 6.2: Leading order error of the Fokker-Planck approximation for protons incident on tungsten at various energies as a function of the cutoff $1 - \mu^*$.

On the contrary, we have seen that Fokker-Planck is as bad for protons as it is for electrons even though the scattering is much more forward peaked for protons. Thus, we expect that there will be smaller mean free paths required when using the Boltzmann Fokker-Planck operator for heavier ions.

6.1.2 Generalized Boltzmann Fokker-Planck Approximation

In any case, the need for higher order approximations for the peaked part of the DCS is clear. We introduce the approximation in the same way as we did for the Boltzmann Fokker-Planck approximation. We write it here in the operator notation

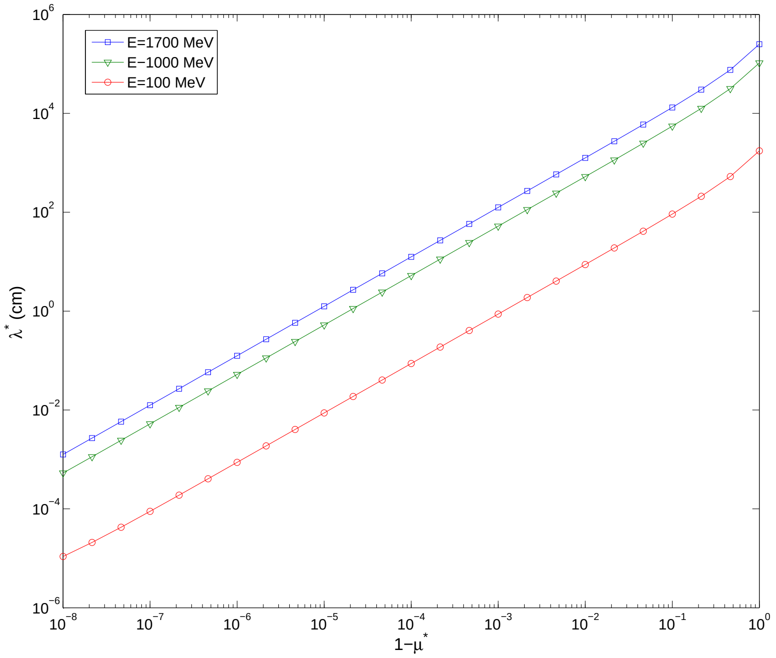

Figure 6.3: Mean free path of the smooth part of the DCS for protons incident on tungsten at various energies as a function of the cutoff $1 - \mu^*$.

introduced in the last chapter.

$$\frac{\partial \psi(s,E)}{\partial s} = L_B^* \psi(s,\Omega) + \int_0^{2\pi} d\theta' \int_{-1}^{\mu^*} d\mu_0 \Sigma_e(\mu_0)\psi(s,\Omega') - \Sigma_{t,e}^* \psi(s,\Omega) \quad (6.6)$$

The cross sections are defined the same in this equation as before. The operator L_B^* is any moment preserving approximation for the singular part of the DCS. That is, we define the transport moments for the singular part as

$$\xi_n^* = \int_{\mu^*}^1 d\mu (1-\mu)^n \Sigma_e(\mu) \quad (6.7)$$

The higher order approximations implicitly preserve more eigenvalues of the singular DCS, and they are much better at approximating the remaining eigenvalues. Therefore, it is necessarily a better approximation than the Fokker-Planck approximation.

Figure 6.4 shows the values obtained for the mean free path and $\overline{\theta}$ for protons incident on tungsten using the discrete model of order 2 and order 4. Unlike our previous treatment of the moment preserving models, the parameters obtained for the cut off DCS are physically reasonable. The mean free path is not too large and the average scattering angle is small enough to be valid for high energy ion transport.

These parameters are indicative of those obtained for other moment preserving models. The exponential model tends to give nearly equivalent parameters as the discrete model because the moments fall of very quickly. Thus, the $C(n)$ factor in Eq.(5.67) has little effect on the solution to those equations. The three moment model may also be used to approximate the singular part of the DCS. We have seen that the accuracy of the three moment model is bracketed by the accuracy of the two moment and four moment models for a full moment preserving treatment. We expect this result for the treatment of the singular part as well.

6.1.3 A Smooth Decomposition of the DCS

Often times it is very inconvenient to treat the integral decomposition in the ways depicted so far. The discontinuity at μ^* that is introduced can cause problems, for instance, with a deterministic treatment of high energy charged particle transport. The well know Gibbs phenomena will occur at the discontinuity when attempting to expand the smooth part of the DCS in Legendre polynomials. This is obviously not a problem for Monte Carlo calculations since the smooth part is just as easy to sample from as the entire DCS.

If a smooth decomposition is desired, the smooth part can be accounted for by

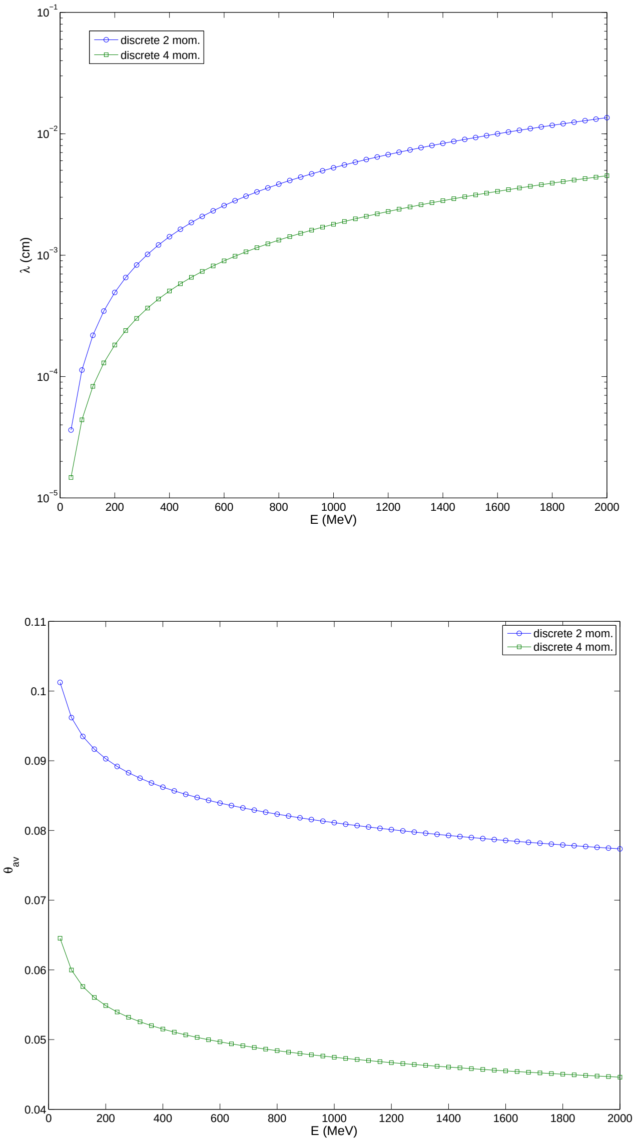

Figure 6.4: Mean free path and $\overline{\theta}$ of the discrete model of order 2 and 4 for protons incident on tungsten with $1 - \mu^* = 10^{-5}$.

introducing the DCS given by

$$\Sigma_e^*(\mu_0) = \frac{K(E)}{(1 + 2\eta^*(E) - \mu_0)^2} + \sum_{m=1}^{M} \alpha_m F(\mu_0, \beta_m). \tag{6.8}$$

The functions given by $F(\mu_0, \beta_m)$ are the normalized functions given by either the discrete representation or the exponential representation. They could also be given by some other pseudo-differential cross section that has yet to be discovered. The value of η^* is a synthetic scattering parameter that is chosen by the user to yield a large mean free path.

The moment preserving method applied to this new approximation is a very simple extension of the previous treatment. To avoid conflicting notations, we introduce the transport moments of the smooth DCS

$$\xi_n^{**} = \int_{-1}^{1} d\mu \frac{(1-\mu)^n K(E)}{(1+2\eta^*(E)-\mu)^2} \tag{6.9}$$

These moments are as easy to compute as the moments ξ_n of the analog DCS. Once obtained, we may use Eq.(5.67) to get the remaining parameters with ξ_n replaced by $\xi^n - \xi_n^{**}$.

This is equivalent to preserving moments of the "difference DCS" given by

$$\Sigma_D(\mu) = \frac{K(E)}{(1+2\eta(E)-\mu_0)^2} - \frac{K(E)}{(1+2\eta^*(E)-\mu_0)^2}, \quad \eta^*(E) \geq \eta(E) \tag{6.10}$$

The condition follows from the requirement that η^* is chosen to yield a larger mean free path combined with Eq.(3.34). This DCS has some interesting and often not obvious properties. First, we can prove that it is always positive. Indeed we get

$$\begin{aligned} \Sigma_D(\mu) \quad &= K\left[\frac{(1+2\eta^*-\mu_0)^2-(1+2\eta-\mu_0)^2}{(1+2\eta(E)-\mu_0)^2(1+2\eta^*-\mu_0)^2}\right] \\ &= 4K(\eta^*-\eta)\left[\frac{1-\mu_0+(\eta+\eta^*)}{(1+2\eta(E)-\mu_0)^2(1+2\eta^*-\mu_0)^2}\right] \end{aligned} \tag{6.11}$$

which is always positive for $\eta^* > \eta$. From the form of Eq.(6.11), we can argue that the difference DCS is also nearly zero for μ_0 sufficiently far from 1 if η^* is small. Then we would have

$$\Sigma_D(\mu) \approx 4K(\eta^*-\eta)\frac{1}{(1-\mu_0)^3} \tag{6.12}$$

and $\eta^* << 1$ implies $\eta^* - \eta << 1$. If η^* is chosen arbitrarily close to η, then we obtain the analog DCS for the smooth part of Eq.(6.8). The remaining parameters will shrink to zero as this occurs. At the other extreme, $\eta^* \to \infty$ would result in an isotropic smooth part with a negligible mean free path, and the remaining parameters would be nearly identical to those obtained by a full moment preserving treatment. Thus, we have a scheme that allows us to choose our degree of approximation where the approximation can never be worse than the usual moment preserving approach.

It is usual to choose the mean free path of the smooth part initially before treating the remaining parameters. In particular, if we would like to have a mean free path given by λ^* for the smooth part, then it can be shown using Eq.(3.34) that

$$\eta^*(E) = \frac{\sqrt{1 + 2K(E)\lambda^*}}{2} - \frac{1}{2} \tag{6.13}$$

Of course, we can also use a three moment model with a different mean free path specified to approximate the difference cross section. Therefore, we actually have the potential for two degrees of freedom in the specification of the smooth decomposition. The total mean free for the problem becomes

$$\lambda^{**} = \left[\frac{1}{\lambda^*} + \sum_{m=1}^{M} \alpha_m\right]^{-1} \tag{6.14}$$

Using a three moment model for the peaked part, the mean free path is fully specified by the user. We will see soon that the mean free path for the monoenergetic case is driven almost exclusively by the length scale of the problem as opposed to the physics. Therefore, we can get speedups of thousands or higher!

6.1.4 Spectral Analysis of the Singular DCS

It is reasonable to ask whether higher order treatments are even necessary. To answer this question, we may compute the eigenvalues of the singular part of the DCS and for the approximate operators as we did in section 5.3.2. Since the transport moments fall off very quickly, we see from Eq.(5.89) that the eigenvalues change very slowly. Since we would like for $\lambda \to -\infty$ very quickly so that the approximate modes are damped out very quickly, we find that our moment preserving approach may have problems converging to the true solution as the penetration of the medium increases. However, since we are approximating the higher modes with a greater accuracy, this does not pose a problem.

Figure 6.5 shows the first 400 eigenvalues computed for the Boltzmann operator with 1700 MeV protons incident on tungsten and $1 - \mu^* = 10^{-5}$. The length scale of the eigenvalues as introduced in Eq.(5.92) is also shown in the figure. Unlike the full Boltzmann operator, where the higher order transport moments increase very sharply after some initial number, the eigenvalues increase very slowly due to an almost negligible contribution from the higher order moments. The corresponding length scale decreases slowly with eigenvalue as well.

We see that approximately 50 eigenvalues are important for resolving the solution over ranges of interest (i.e. the range of a 1700 MeV proton in tungsten). We look at the error in the first 50 eigenvalues for the Fokker-Planck approximation, the 2 moment discrete model, and the 4 moment discrete model in Fig.(6.6). Though the errors are small in each case, we see that there is a slight contribution in error over several modes. The accumulation of these errors could contribute to an inaccurate solution for various penetration depths. On the other hand, the 4 moment discrete model has eigenvalues that are equal to the eigenvalues of the Boltzmann operator to within machine precision ($\approx 10^{-15}$) for almost all eigenvalues of interest.

We may similarly analyze the eigenvalues of the three moment models for approximating the singular part of the DCS. The results of computing the relative error of the eigenvalues of the three moment model using various mean free paths for 1700 MeV protons incident on tungsten are shown in Fig.(6.7). The astonishing

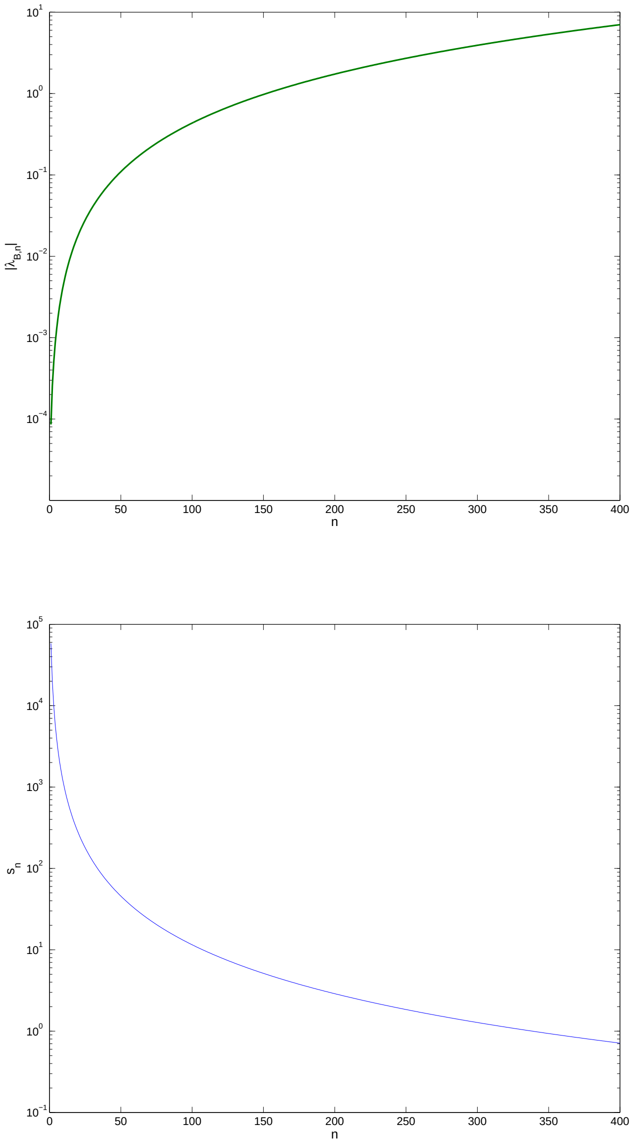

Figure 6.5: Eigenvalues and their length scale for the singular portion of the DCS for 1700 MeV protons incident on tungsten with $1 - \mu^* = 10^{-5}$.

fact is that the eigenvalues retain the same accuracy regardless of the mean free path chosen. Furthermore, the accuracy of the three moment models is perfectly centered between the two and four moment models. This is a direct consequence of the rapid-

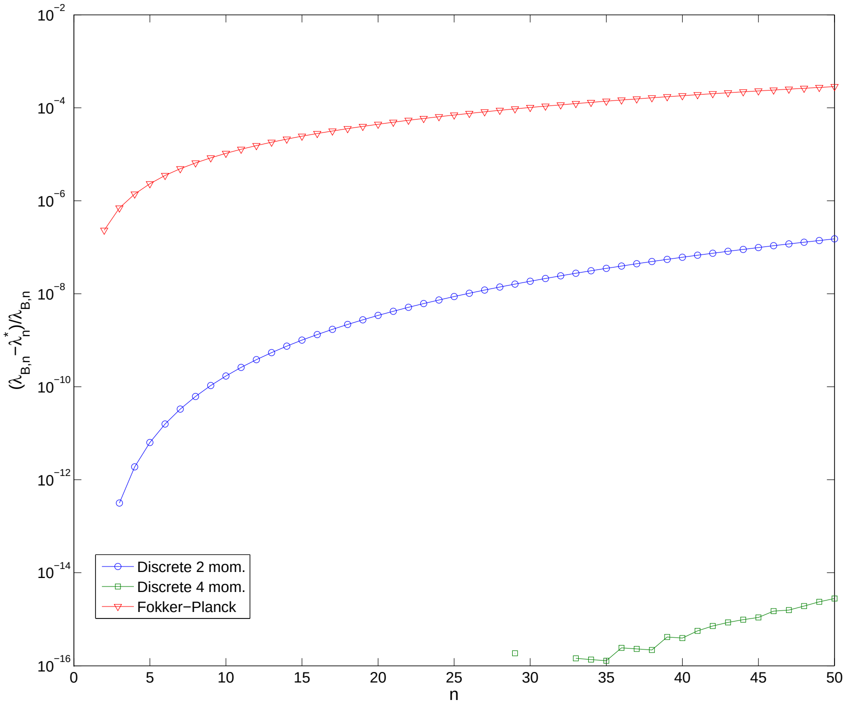

Figure 6.6: Relative error of the eigenvalues of the approximate operators for 1700 MeV protons incident on tungsten with $1-\mu^* = 10^{-5}$.

ity at which the higher order moments fall off with moment number n. The accuracy of the first few moments will dominate the accuracy of all of the eigenvalues due to the summation formula given in Eq.(5.89).

We have seen sufficient evidence to suggest that our decomposition schemes are very accurate for treating a highly peaked DCS. Also, we have seen that the accuracy of the methods can be much higher for a simple two or three moment model then for the Fokker-Planck model when approximating the peaked part of the DCS. We will now consider some numerical experiments to solidify these ideas.

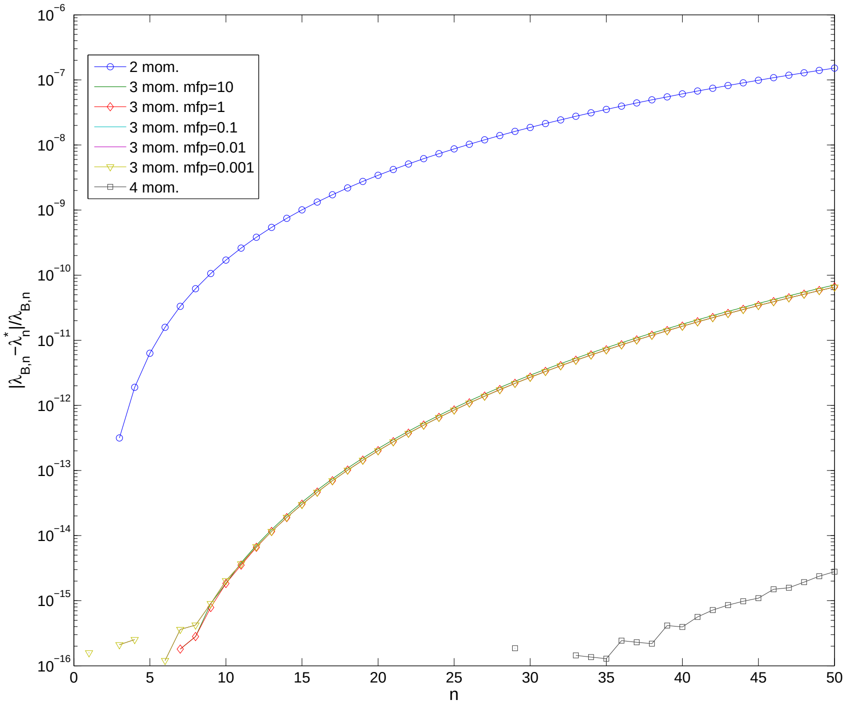

Figure 6.7: A comparison of the accuracy of the eigenvalues of the two moment, four moment, and three moment models with varying mean free path for 1700 MeV protons incident on tungsten with $1-\mu^* = 10^{-5}$

6.2 Numerical Experiments with Hybrid Methods

As a preliminary test, we consider the simulation of just the peaked part of the DCS. That is, we let

$$\Sigma_e(\mu) = \begin{cases} \frac{K(E)}{(1+2\eta(E)-\mu)^2} & : \quad \mu > \mu^* \\ 0 & : \quad \mu < \mu^* \end{cases} \tag{6.15}$$

In a Boltzmann Fokker Planck model, this represents the portion of the DCS that is being approximated. We've seen that $1-\mu^* = 10^{-5}$ represents a good tradeoff between run time and accuracy. Thus, we will use this value for the example.

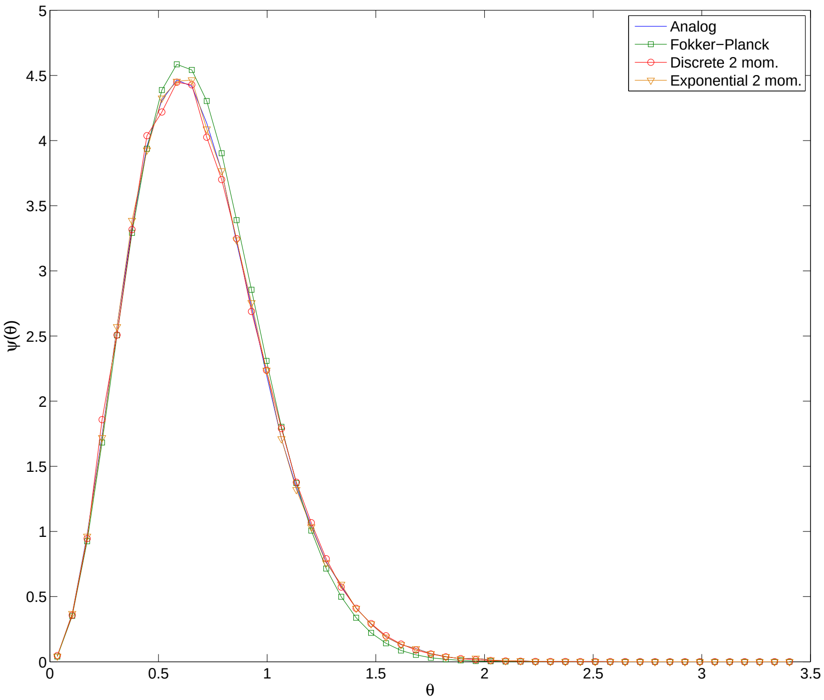

Figure 6.8: A comparison of the accuracy of the moment preserving methods with the Fokker-Planck method when simulating just the singular part of the DCS for 1700 MeV protons incident on 0.5 cm tungsten.

The results of a simulation using this cutoff DCS for 1700 MeV protons incident on 0.5 cm of tungsten are shown in Fig.(6.8). We see that, even though the leading order error of the Fokker-Planck approximation is small, the Fokker-Planck approximation is still fairly poor at capturing the solution to the problem. We can, of course, get better accuracy with a larger μ^*, but this would result in a larger run time for the problem. However, we see that the two moment models are much better at approximating the solution. This gain in accuracy can be accounted for by the much better approximation of the eigenvalues of the Boltzmann operator. We see that the three orders of magnitude difference in accuracy for the eigenvalues gives a much more accurate DCS over smaller distances since many eigenvalues are required to capture the important modes of the solution.

Moving on to more realistic problems, we now consider the solution for 1000 MeV protons incident on 1 cm of tungsten. The solution to this problem for a full moment preserving treatment was shown in Fig.(5.15). In Fig.(6.9) shows how accurate the three moment hybrid models are with varying mean free path. A smooth decomposition described by Eq.(6.8) was used to generate these plots. The mean free path stated in the figure is that of the smooth part and the singular approximation (i.e. $\lambda^{**} = \lambda^{*} =$MFP).

The smoothed hybrid methods do quite well at approximating the analog results with a mean free path of 0.01 cm. The approximation is less accurate when the mean free path 0.1 cm but is still much better than the Fokker-Planck approximation. The exponential model is a better model for the larger mean free path. This is no surprise since the exponential model consistently outperformed the discrete model with the full moment preserving treatment. Surprisingly, the Fokker-Planck model also does very well when $\lambda = 0.01$ cm. However, it is as bad as the three moment discrete model when the mean free path is 0.1 cm.

A great many more results can be obtained to prove the accuracy of the hybrid models under various conditions. However, we've seen that the behavior of the approximations remains the same for a large range of penetrations in previous problems. We will now consider other limits to which we may take the methods considered here. We first consider a reduction in energy of the particles. In Fig.(3.4) and Fig.(3.5) we see that the magnitudes of $K(E)$ and $\eta(E)$ increase drastically for reduced energies. However, they do so in such a way that $\overline{\mu}$ decreases since Σ_{tr} is increasing much more quickly then Σ_t. This is a difficult limit for each of the methods because we assume that $\overline{\mu}$ is very close to 1 in their derivations. However, the moment preserving methods are necessarily better for smaller $\overline{\mu}$ since the higher order moments and eigenvalues are accounted for.

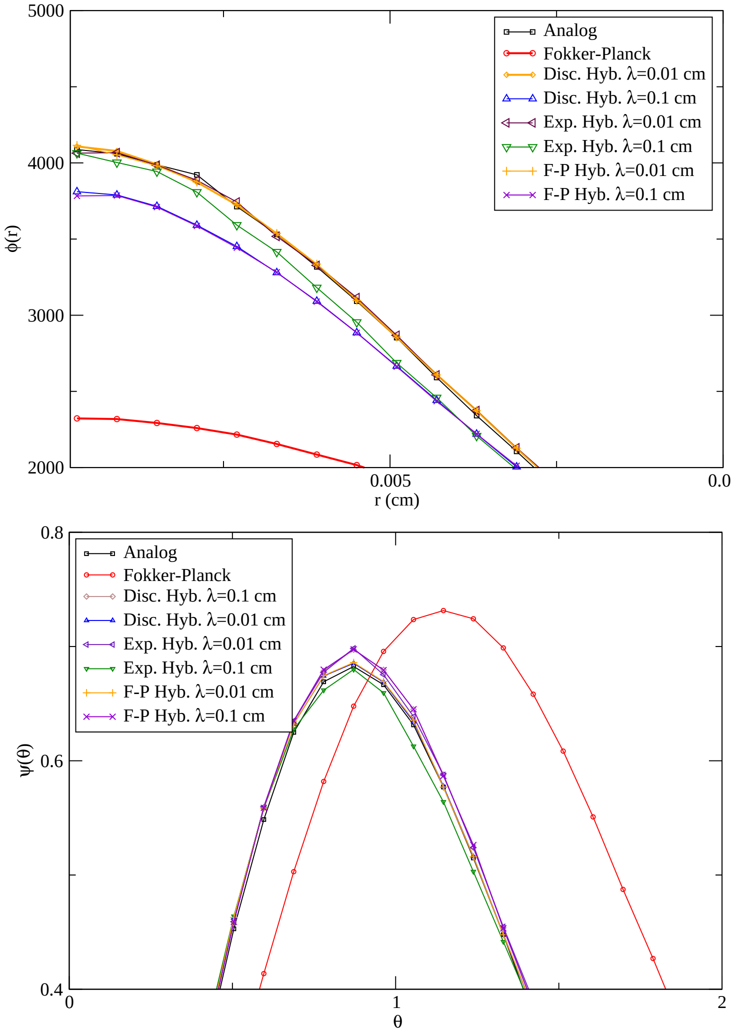

Figure 6.9: Comparison of the hybrid methods, Fokker Planck, and Analog methods for 1000 MeV protons incident on 1 cm tungsten

Figure 6.10 shows the result of using the Fokker-Planck method, the 4 moment hybrid methods with a smooth decomposition, the hybrid Fokker-Planck method and the analog method for 100 MeV protons incident on 1 cm of tungsten. As before, the Fokker-Planck method gives a very poor approximation. However, the hybrid methods are still very accurate. Though the methods are being tested at a much lower energy than before, the results are still basically the same. The Fokker-

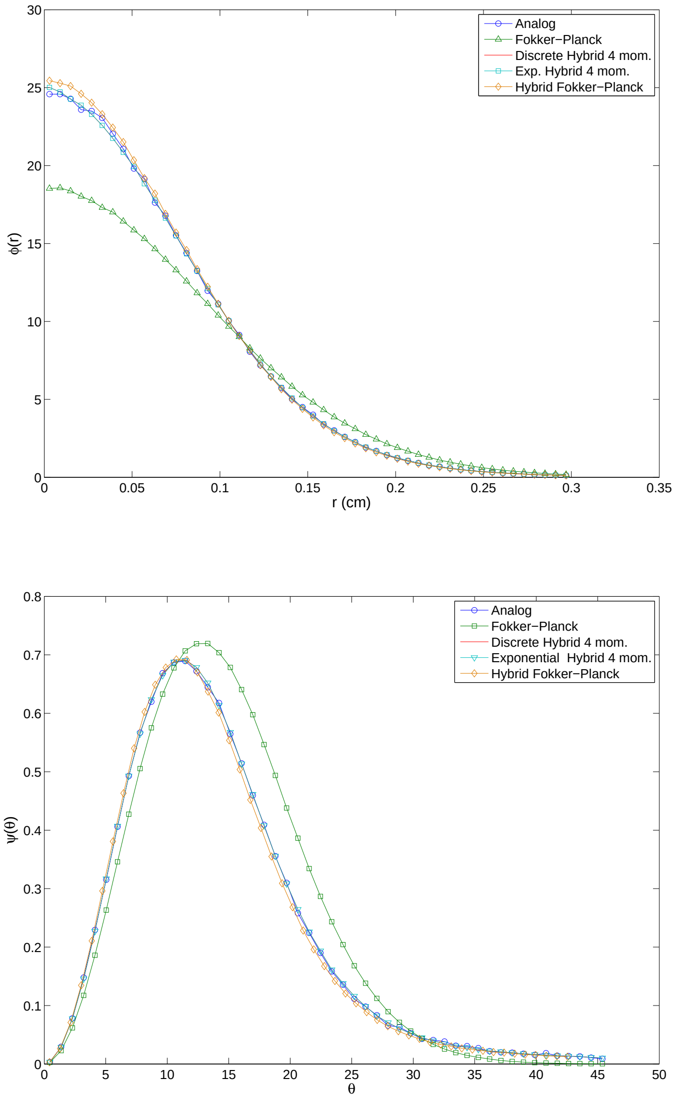

Figure 6.10: Comparison of the hybrid methods, Fokker Planck, and analog methods for 100 MeV protons incident on 1 cm tungsten

Planck method shows some discrepancy near the peak of the radial distribution and at smaller angles for the angular distribution. We note that this is likely due to a poorer approximation of the singular part of the scattering DCS. This becomes apparent now that $1 - \overline{\mu}$ is larger due to the lower energies.

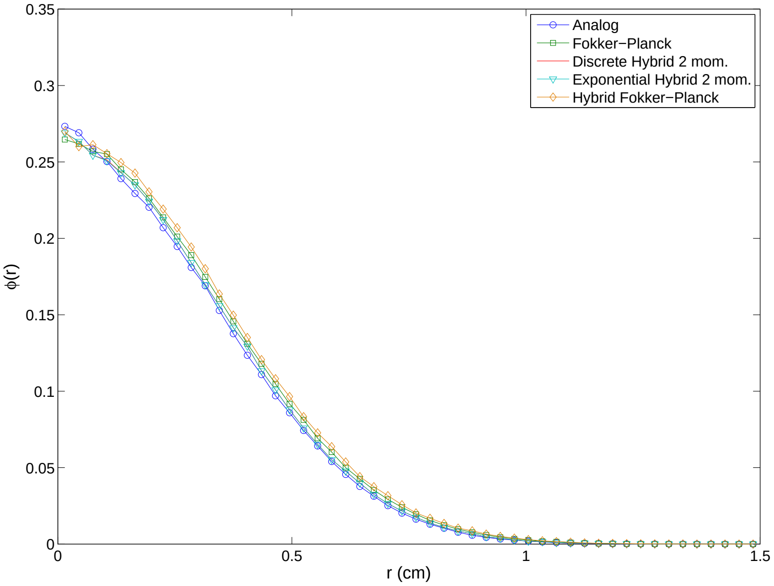

Figure 6.11: Comparison of the hybrid methods, Fokker-Planck, and analog methods for 10 MeV protons incident on 1 cm tungsten

At further reduced energies, we consider 10 MeV protons incident on 1 cm of tungsten. The resulting radial distributions are shown in Fig.(6.11). Somewhat surprisingly, we find that all methods have almost identical solutions. The analog solution is somewhat noisier since the number of particles was significantly reduced to run the problem in a fair amount of time. To explain the apparent success of the methods, including the Fokker-Planck method, we appeal to the eigenvalues of the problem. For this problem $\Sigma_{tr} = 1.95$ cm^{-1} and $1 - \overline{\mu}_0 \approx 10^{-6}$. This is in sharp contrast to the higher energy problems where the transport cross section and $1 - \overline{\mu}_0$ are both many orders of magnitude smaller.

This tells us that the eigenvalues of the problem are huge and a 1 cm penetration looks very large to the methods. Therefore, even Fokker-Planck does well for this problem. However, since the penetration depth is about 10^7 mean free paths, it is unrealistic that we will see this kind of convergence of the methods at low energies due to energy-loss effects. On the other hand, we do see evidence of the statement that the Fokker-Planck method does well when penetrations are on the order of λ_{tr}, the transport mean free path. Since this is much larger than the total mean free path of the problem, it is unlikely that it will help us, even when λ_{tr} is small.

Another interesting test of the methods is for their ability to handle larger ions. We've seen that the difference is embodied by the parameters $K(E)$ and $\eta(E)$ in the Rutherford DCS. For larger ions, the parameters both decrease in such a way that Σ_{tr} is decreased and Σ_t is increased. Since $\overline{\mu} = 1 - \Sigma_{tr}/\Sigma_t$, we find that $\overline{\mu}$ approaches unity as the mass number of the incident ion increases. This is precisely the limit that we require for the methods to work well.

As a test, we consider 200 MeV carbon ions incident on 1 cm of water. For this problem, $\Sigma_t = 1.2 \times 10^7$ and $\Sigma_{tr} = 1.35 \times 10^{-2}$. The radial distribution is shown in Fig.(6.12) for the analog method, the Fokker-Planck approximation, and the hybrid methods of order 3 with a 0.01 cm mean free path. Though we are considering a much more forward peaked problem, the Fokker-Planck approximation is still a poor approximation. However, the hybrid methods do very well at approximating the solution. In this case, the hybrid Fokker-Planck solution does as well as the other methods. This is likely due to the much smaller value for $1 - \overline{\mu}$.

The interpretation that we get from these results is that the moment preserving hybrid methods are very robust when approximating the transport for many types of ions and at a wide range of energies. Table 6.1 shows the speedups for the problems considered in this chapter for each of the methods used. The Fokker-Planck method is by far faster than any other method. However, it is also the least accurate method. Also, we find that the mean free path can be chosen to be quite large for the Fokker-Planck method without effecting the convergence that is associated with the chosen mean free path. We have the same ability to choose the mean free path of the hybrid

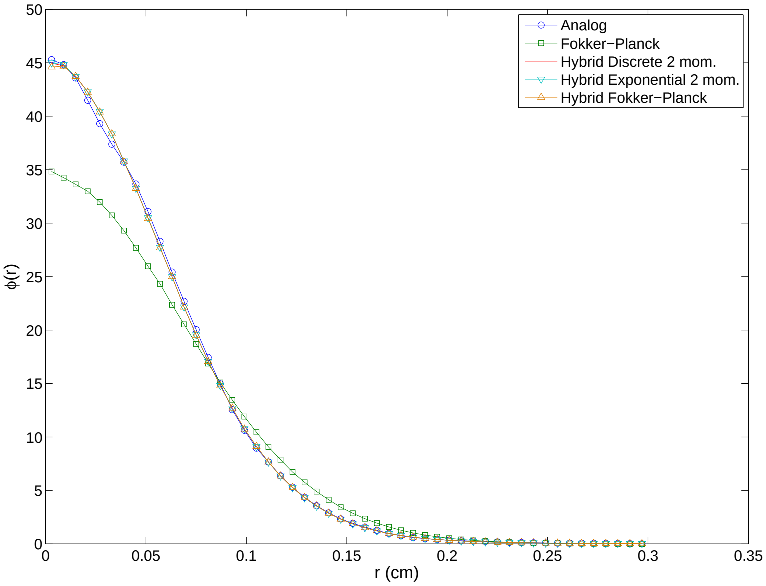

Figure 6.12: A Comparison of the analog solution, Fokker-Planck solution, hybrid Fokker-Planck, and the hybrid methods of order 3 with $\lambda^* = 0.01$ cm for 200 MeV carbon ions incident on water.

Test Case	**Speedup**			
	F-P	Hyb.Exp.	Hyb.Disc.	Hyb. F-P
1000 MeV p → W (1 cm)	1050	478	503	512
100 MeV p → W (1 cm)	5020	2185	2462	2601
10 MeV p → W (1 cm)	4370	1903	2147	2223
200 MeV C → H_2O (1 cm)	12500	5776	6105	6215

Table 6.1: Speedup of hybrid methods and the Fokker Planck method over the analog method for various elastic scattering problems.

methods. We find that $\lambda^* = 0.01$ cm leads to accurate results, while a larger mean free path is noticeably less accurate as seen in Fig.(6.9).

It is also worth noting that the hybrid methods have roughly the same speedup as the full moment preserving methods because in both cases, the mean free path is chosen to be the maximum value that doesn't appreciably effect the results. Thus, there is almost no additional cost required to use a hybrid method. It can easily be seen however that the speedup is reduced significantly for the 10 MeV problem. The reason for this is that the mean free path for the moment preserving method needed to be reduced by a full order of magnitude to maintain positive parameters. Though this was not necessary for the Fokker-Planck methods, the mean free path was reduced anyway so that comparisons could be made honestly with the other moment preserving methods.

6.3 Heavy on Light Ion Interactions

We've seen that the the artificial cutoff imposed on the Rutherford DCS allows for accurate treatment of the singular portion with a moment preserving method, or even Fokker-Planck in certain cases. This cutoff carried the caveat that the smooth portion must also be handled in some way. For heavy ions interacting with light ions, occurring for instance in an ion implantation application, there is a natural cutoff associated with the kinematics. We saw this briefly in Chapter 3 and the concept is displayed in Fig.(3.2). The phenomena is that heavy ions scattering off of light ions can only scattering into a certain narrow cone of angles.

To see how this phenomena works in our favor, we consider the formulation of the Fokker-Planck method in the lab frame. Up until this point, the approximation was made in the center of mass frame and the coordinate change occurred explicitly during the calculation. This works for Monte Carlo methods, but it does not work for deterministic methods. The coordinate change must be implicitly defined in the expression for the differential cross section. In the context of moment preserving methods, this means that all of the moments must be defined with respect to the lab frame scattering cosine μ_L given by

$$\mu_L = \frac{\alpha + \mu_0}{(\alpha^2 + 2\alpha\mu_0 + 1)^{1/2}} \tag{6.16}$$

$$\alpha = \frac{M_i}{M_t} \tag{6.17}$$

The parameters M_i and M_t are the incident particle and target particle masses respectively. Thus, the nth moment of the DCS becomes

$$\xi_{L,n} = \int_{-1}^{1} (1 - \mu_L)^n \Sigma_e(\mu_L) d\mu_L \tag{6.18}$$

To simplify matters, we use $\Sigma_e(\mu_L)d\mu_L = \Sigma_e(\mu_0)d\mu_0$. Then this integral can be rewritten in terms of the center of mass cosine μ_0.

$$\xi_{L,n} = \int_{-1}^{1} \left(1 - \frac{\alpha + \mu_0}{(\alpha^2 + 2\alpha\mu_0 + 1)^{1/2}}\right)^n \Sigma_e(\mu_0) d\mu_0 \tag{6.19}$$

Though this integral is much less appealing to solve, it can be done easily using adaptive quadrature methods. The resulting value for the moments is a significant decrease from the center of mass moments due to the natural cutoff imposed. When $\alpha > 1$, the cutoff is given by

$$\mu_{L,min} = \frac{\sqrt{\alpha^2 - 1}}{\alpha} = \frac{\sqrt{M_i^2 - M_t^2}}{M_i^2} \tag{6.20}$$

The lab frame DCS is plotted in Fig.(6.3) for increasing α when the center of mass DCS is given by the screened Rutherford relation. For this plot, $K = 0.001$ and $\eta = 10^{-10}$, values comparable to what is found with heavy ions. Not only does the natural cutoff increase the minimum μ, but it also reduces the magnitude of the DCS at larger angles (smaller μ). Since the total cross section remains unchanged by the kinetmatics, the DCS must be larger at smaller angles. The overall effect of increasing α is to increase $\overline{\mu}_L$ toward 1 for a given set of center of mass parameters K and η.

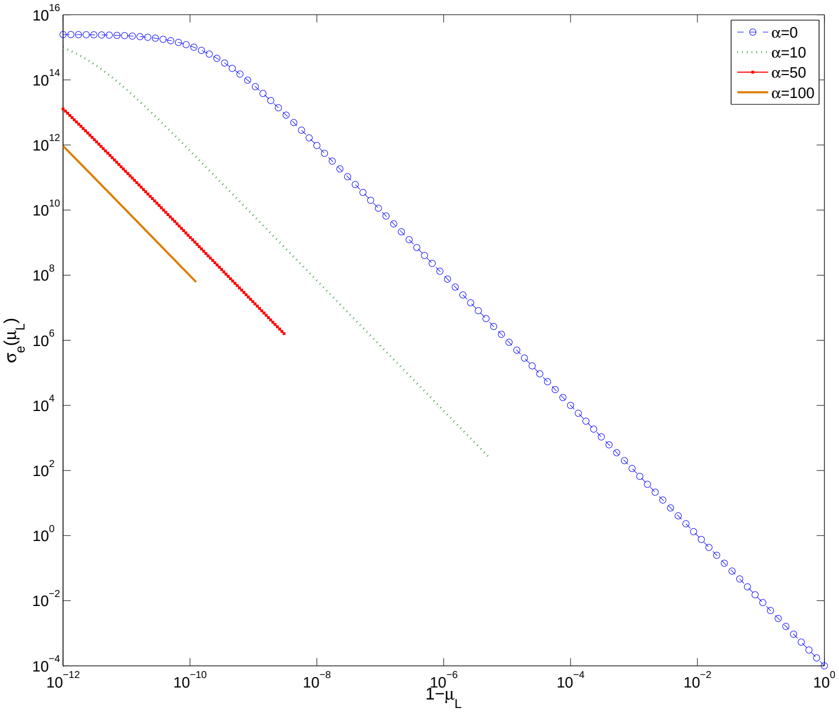

Figure 6.13: A comparison of the lab frame DCS for $K = 0.001$ and $\eta = 10^{-10}$ for increasing α.

We can plot the cutoff μ_{min} as a function of the mass ratio α. The result is shown in Fig.(6.3) for the same parameters as those given in the last paragraph for the largest range of realistic values for α. We see that the cutoff is very slowly varying in the range of interest, but the values are promising since they are in the range $10^{-3} - 10^{-4}$.

We can also look at a simple bound on the Fokker-Planck error term. If scattering were isotropic in the center of mass system, certainly we would expect that the ratio of the variance to the mean of $1-\mu_0$ to be larger than if we had Rutherford scattering in the center of mass system. Then, we could write the DCS in the lab system for a

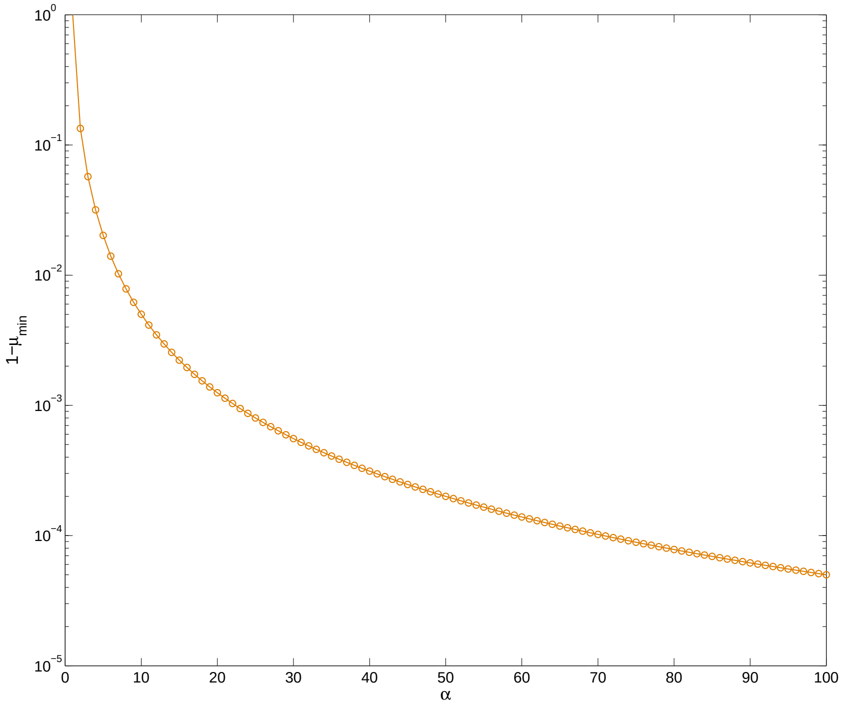

Figure 6.14: The natural cutoff as a function of α for $K = 0.001$ and $\eta = 10^{-10}$.

given Σ_t as

$$\Sigma_e(\mu_L) = \begin{cases} \Sigma_t/(1-\mu_{min}) & : \quad \mu_{min} \le \mu_L \le 1 \\ 0 & : \quad -1 \le \mu_L \le \mu_{min} \end{cases} \tag{6.21}$$

Then, it is simple to compute

$$\frac{\mathrm{var}(\mu_L)}{1-\overline{\mu}_L} \sim \frac{\overline{(1-\mu_L)^2}}{1-\overline{\mu}_L} = \frac{2}{3}(1-\mu_{min}) \tag{6.22}$$

Substituting Eq.(6.20) into Eq.(6.22) gives

$$\frac{\mathrm{var}(\mu_L)}{1-\overline{\mu}_L} \sim \frac{2}{3}\left(1-\sqrt{1-1/\alpha^2}\right) \sim O\left(\frac{1}{\alpha^2}\right) \tag{6.23}$$

This bound and a numerical calculation of the Fokker-Planck leading order error term are shown in Fig.(6.15). We see that the numerical calculation and the formula

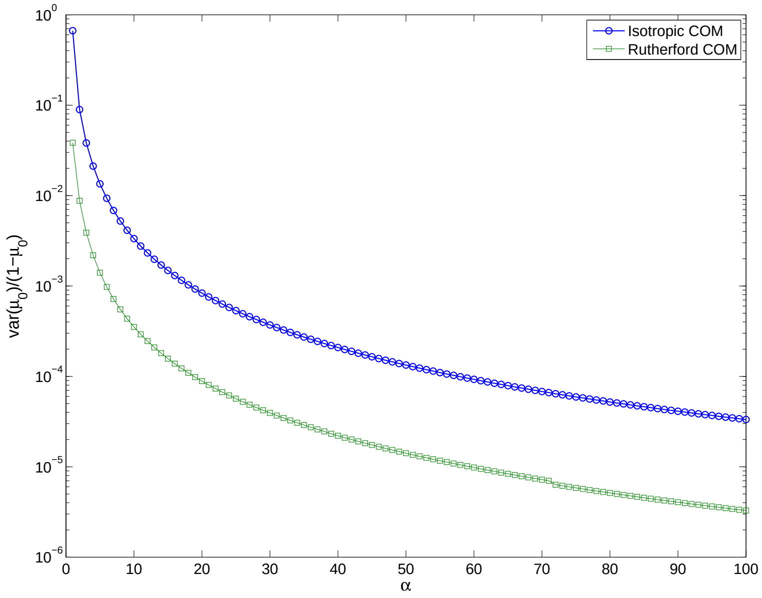

Figure 6.15: Leading order error term for the Fokker-Planck approximation for an isotropic DCS and a Rutherford DCS as a function of μ_{min}.

given in Eq.(6.23) have the same behavior for large α. However, the numerical calculation gives a magnitude that is much smaller because the Rutherford DCS is forward peaked in the center of mass frame. That is, we get the same asymptotic behavior as we see in the isotropic case but with a much smaller magnitude due to the form of the Rutherford DCS.

To understand how the parameter α effects the accuracy of a Fokker-Planck solution, we consider three analog problems with $\Sigma_{tr,L} = 10^{-6}$ with varying α and the corresponding Fokker-Planck solution for this Σ_{tr}. Since we are holding Σ_{tr} fixed, we must increase Σ_t to compensate for a decrease in $1 - \overline{\mu}_L$ with increasing α. The corresponding physical intuition is that the scattering is becoming more forward peaked. The angular and radial distributions for this problem are shown in Fig.(6.16). Though the convergence is slow with increasing α, the Fokker-Planck

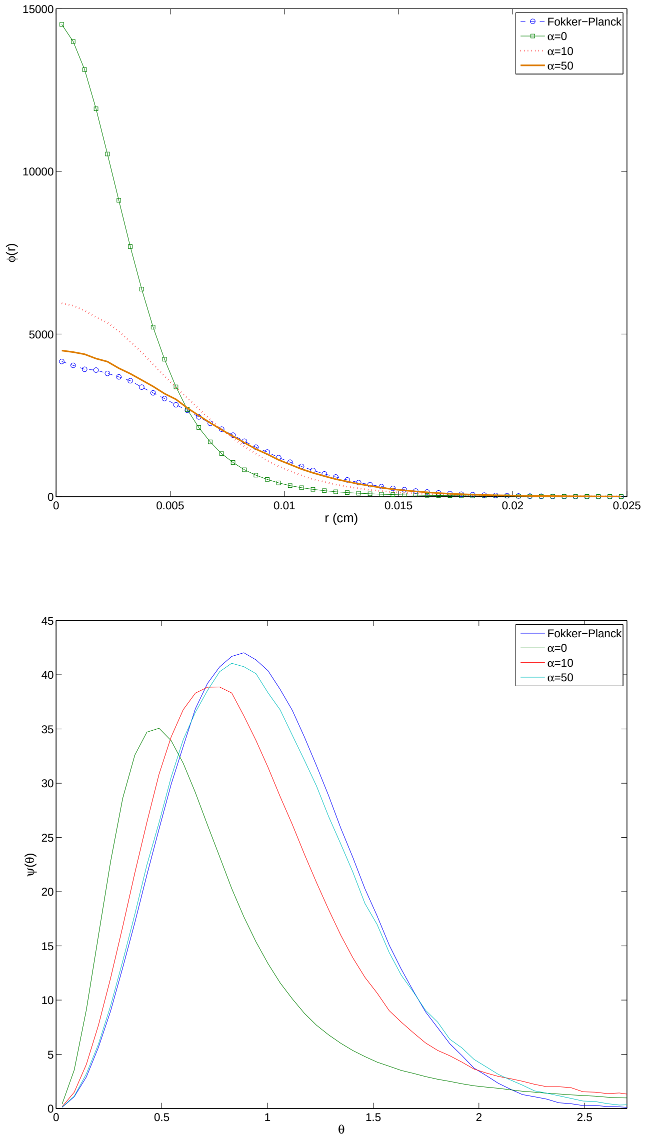

Figure 6.16: Convergence of the analog solutions toward the Fokker-Planck solution for increasing α with $\Sigma_{tr} = 10^{-6}$

solution does do well to approximate the solution in the limit of large α. Since the convergence is determined by the physics, we cannot count on this approximation to work well in general for realistic problems.

On the other hand, the procedure given above can be extended to general moment preserving methods quite easily. We simply required the lab frame moments given by Eq.(6.19) to obtain identical approximations to those given in this chapter. This was done for the $\alpha = 10$ and the $\alpha = 50$ cases given above. The results with the same analog and Fokker-Planck solutions are shown in Fig.(6.17) and Fig.(6.18) for $\alpha = 10$ and $\alpha = 50$ respectively.

In the $\alpha = 10$ case, the second moment in the lab frame was $\Sigma_2 \approx 5.5 \times 10^{-8}$. In the $\alpha = 50$ case, $\Sigma_2 \approx 2.2 \times 10^{-9}$. From this we see that the moments are decaying much more quickly. The solutions are much better for the two moment models than for the Fokker-Planck model. For $\alpha = 50$, the two moment model is almost identical to the analog solution. This demonstrates that a simple two moment model extension can improve the performance drastically over Fokker-Planck for heavy on light ion interactions. Obviously, a four moment model should work even better.

The simple advantage to this scheme is that the angular redistribution can be completely handled by smooth operators for deterministic calculations. Larsen and Leakes showed that this was easily performed by their eigenvalue preservation technique [27]. Thus, for this type of transport problem where straight-ahead transport is often used, one can get accurate solutions very quickly and very simply. If one would like to use multigroup transport codes to do the calculation, the exponential model can also be used to get the same result. The advantage to using the exponential model is that the DCS is much more smooth and one needs not worry about partial range expansions as in the generalized Boltzmann Fokker-Planck procedure.

6.4 A Look at Dose in Higher Dimensions

We've seen that dose in a one dimensional setting can be accurately captured with a simple two moment or four moment model for heavy charged particles. In many

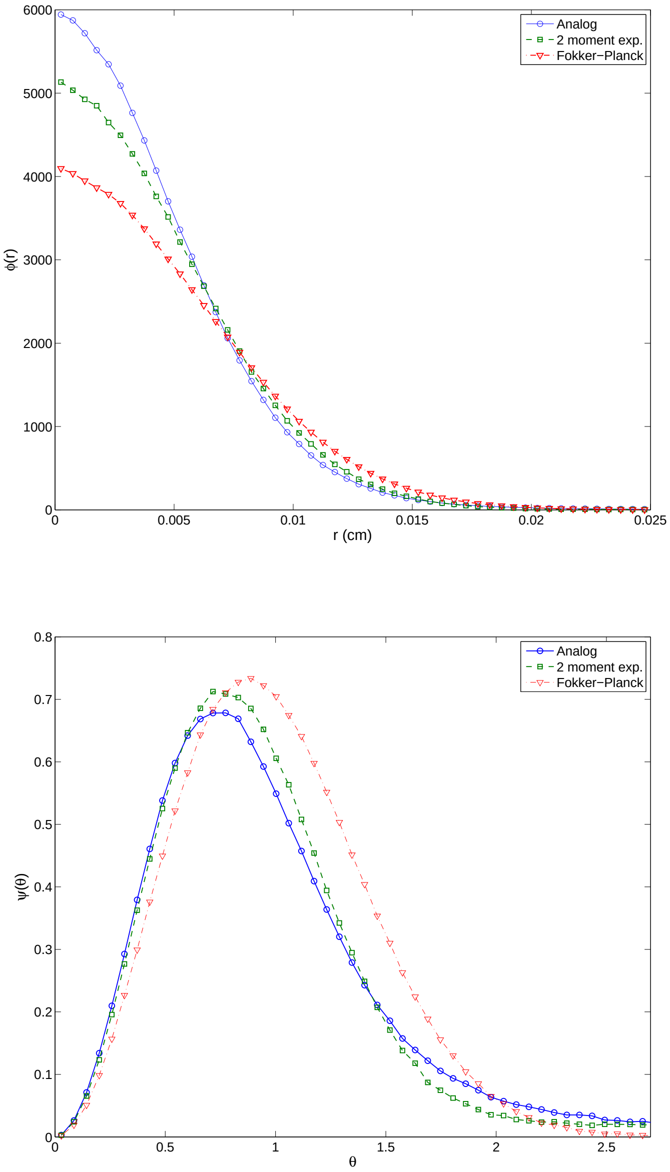

Figure 6.17: A comparison of the radial and angular distributions for heavy ions on light ions with $\alpha = 10$ for analog, Fokker-Planck, and a 2 moment exponential model.

cases, this is the only quantity of interest. However, simply combining the accurate moment preserving methods for energy loss with the equally accurate hybrid methods

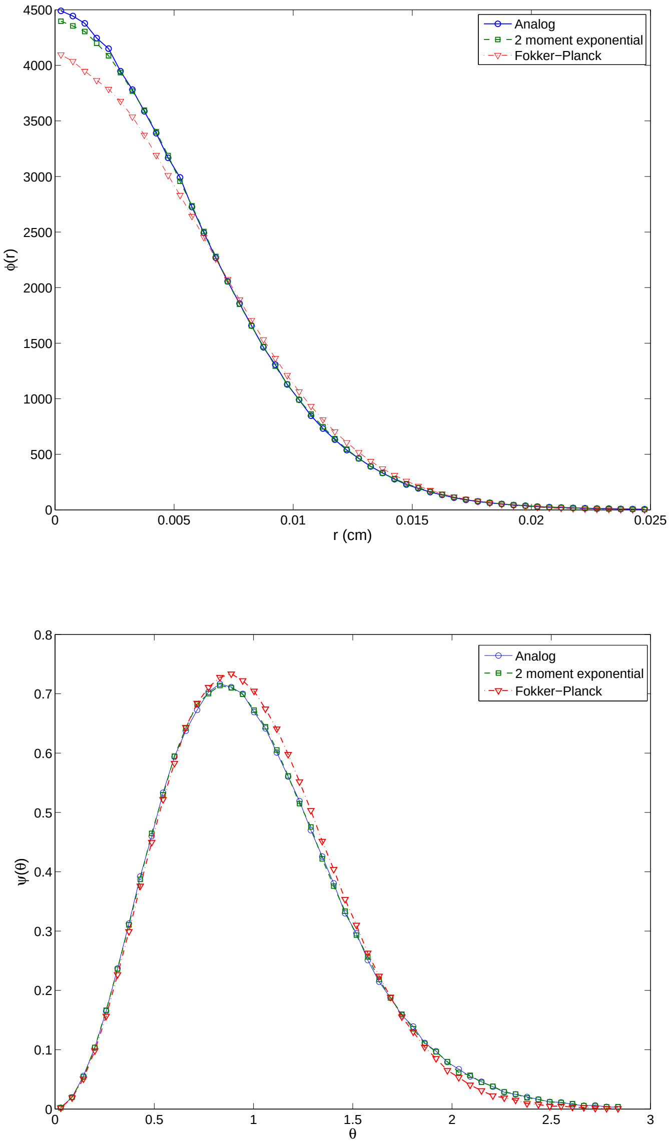

Figure 6.18: A comparison of the radial and angular distributions for heavy ions on light ions with $\alpha = 50$ for analog, Fokker-Planck, and a 2 moment exponential model.

for scattering requires some finesse.

Unfortunately, a blind combination of the two physics can lead to very poor results. The reason for this is simple. The relaxation of the space-angle modes of the solution to the transport equation cannot happen properly if energy loss is occuring to quickly or too slowly. It is not clear at this point what the optimum proportion of energy loss and scattering should be present so that an accurate solution to the full transport equation can be obtained. However, this problem has been encountered already in the development of condensed history codes.

In a condensed history setting, the spatial and angular spreading using distributions due to Goudsmit and Saunderson are combined with straggling due to Landau or Vavilov. It was found empirically that energy straggling should occur over an interval roughly equal to the distance required for a particle to lose 8% of its energy on average. That is, the step size s becomes

$$s = \int_{E_i}^{E_{i+1}} \frac{0.08E}{S(E)} dE \tag{6.24}$$

The integral allows for a continuous slowing down approximation to be used within the step while E_i and E_{i+1} are the energy bin bounds. Scattering within a straggling step is then done using substeps of varying number based on the energy of the particle. This number is not easily accessible but condensed history experts at LANL quote it at about 100 substeps per straggling steps[41].

It would be logical to use Eq.(6.24) to set the mean free path of the inelastic scattering pseudo-DCS and subsequently setting the mean free path of the elastic scattering pseudo-DCS to 1/100th of that value. However, this is impossible due to reasons that have already been discussed. The three moment model for inelastic scattering where a free parameter is introduced does not allow for an arbitrary setting of the mean free path. In fact, the upper limit of the mean free path is likely, but not proven to be, limited to the mean free path of the two moment model. This discouraging fact can be remidied by using hybrid methods for inelastic scattering. However, this was not done for the research presented in this thesis.

To test the ideas considered here, however, the mean free path of the elastic scattering pseudo-DCS was set to 1/100th of the mean free path of the inelastic scattering pseudo-DCS. As a test case, we consider 500 MeV protons incident on tungsten metal with a lower energy cutoff set to 50 MeV. This lower energy cutoff was chosen to make the problem solvable in a reasonable amount of time with the methods used. Due to reason discussed in the previous chapter, allowing the lower energy cutoff to slip to values below 50 MeV substantially increases the computing time required to complete the calculation for even the moment preserving methods.

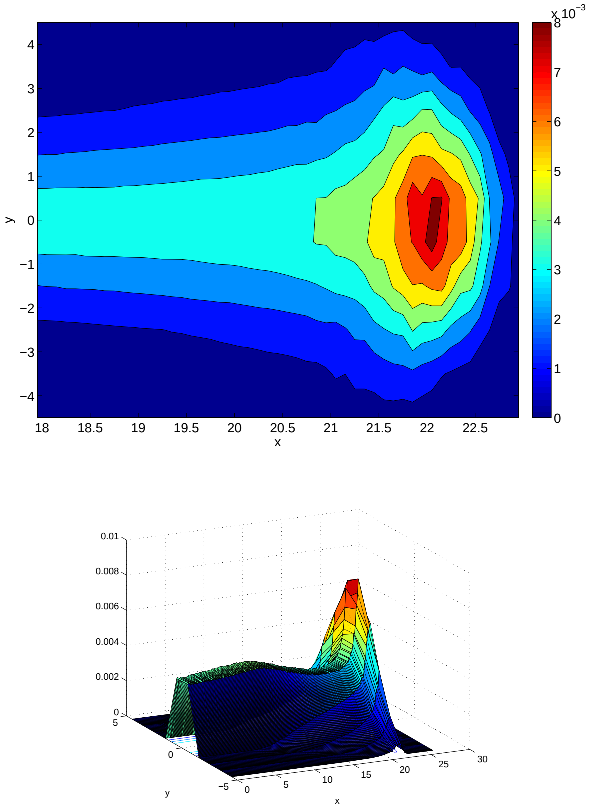

Figure 6.19: Dose profile for 500 MeV protons incident on tungsten metal with a 50 MeV lower cutoff for energy.

Figure 6.19 shows a contour plot and surface plot of the dose profile obtained by using an analog method for the problem described above. As we would expect, there is a distinct Bragg peak located near the range of the particle. It is this Bragg peak that we are interested in capturing accurately. The radial spreading from the beam center occurs symmetrically causing the peak to spread out spatially. An inaccurate means of handling the spatial spreading with respect to the energy loss will result in signficant error when computing the size and location of this peak.

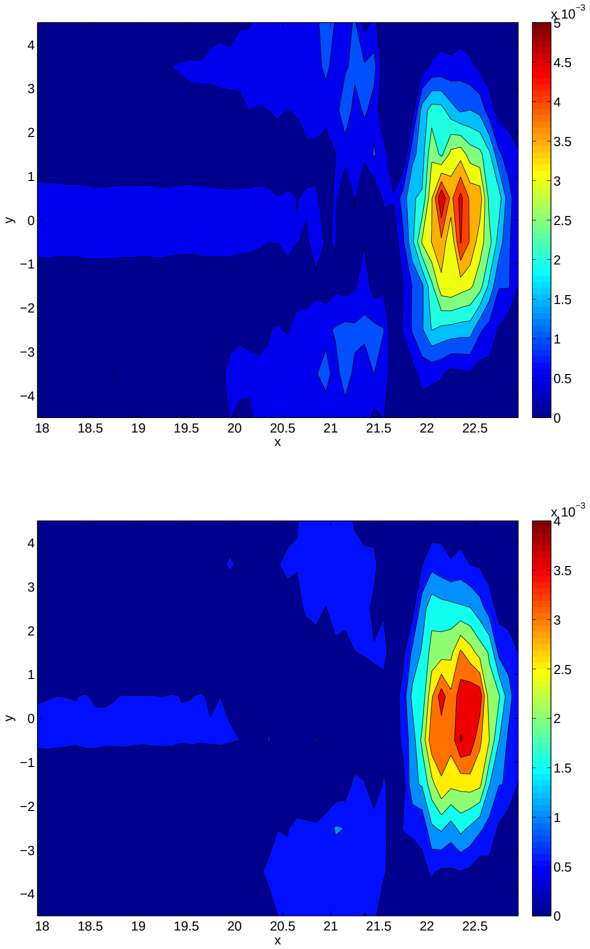

Figure 6.20: Local error obtained from computing the dose profile in Fig.(6.19) using a Fokker-Planck approximation or a 3 moment hybrid discrete method for scattering.

Figure 6.20 shows a profile of the local error near the peak of the dose distribution when using Fokker-Planck and a three moment hybrid discrete method for elastic scattering. The three moment hybrid method is applied without taking into account the mean free path of the inelastic scattering pseudo-DCS. Thus, the error is as large for the hybrid method as it is for a simple Fokker-Planck approximation because the energy loss is occuring much more rapidly than scattering. This leads to an unphysical situation in which there are fewer scatters and thus less spatial redistribution than what should be present for the physics.

The condensed history like treatment for elastic scattering was used for the same problem. The resulting error profile is given in Fig.(6.21). The error is noisier indicating that it is statistical in nature. The colorbar also indicates that the magnitude of the error is much smaller than the error in Fig.(6.20). A sum over the local relative errors in the y-direction for each of the three approximations is shown in figure 6.22. Again, we see that the local relative error is about the same for the Fokker-Planck and the hybrid method when applied arbitrarily. However, the relative error for the hybrid method with a condensed history like treatment of the elastic scattering mean free path is much smaller near the peak. Thus, it is appropriate to use this methodology when combining the elastic and inelastic scattering pseudo-DCS for multi-dimensional treatments of dose.

However, there is no indication that this is an ideal treatment of combined scattering. In fact, requiring at least 100 times as much elastic scattering as inelastic scattering makes the problem expensive computationally. The speedup for the problem given above is only 2.36 when using the condensed history treatment. However, the hybrid method without the condensed history treatment gives a speedup of 233. Thus, we lose most of the efficiency by introducing the additional constraints on the mean free path. Clearly, this can all be remidied by finding an appropriate hybrid method for inelastic scattering. Such a task has been completed previously and will not be repeated for this thesis.

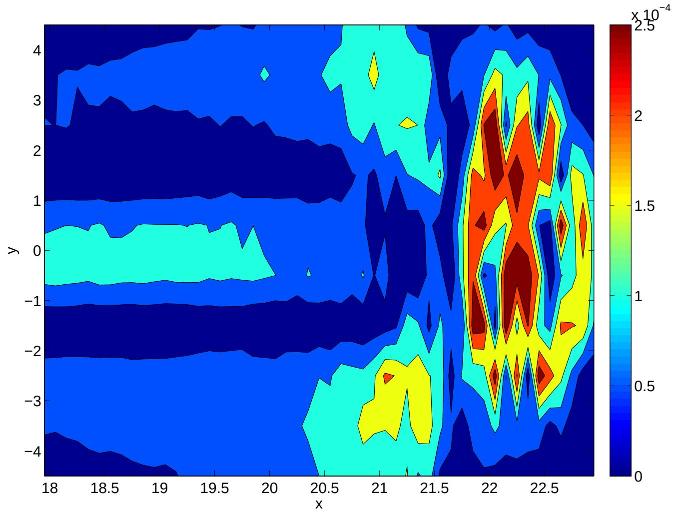

Figure 6.21: Local error obtained when using a condensed history like treatment of the mean free path for elastic scattering.

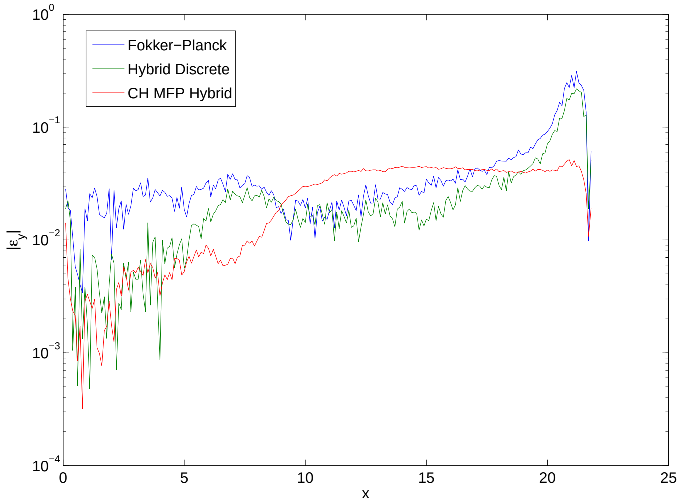

Figure 6.22: Local relative error of the three previously described methods for computing the dose profile summed over the y-direction.

6.5 Hybrid Methods Summary

We conclude that the hybrid methods are a powerful and robust means for simulating arbitrary charged particles at almost arbitrary energies. We see that the degree of approximation can be adjusted very simply by either adjusting the cutoff in the GBFP model or by adjusting the synthetic parameter η^* in the smooth model. Thus, one may easily compare solutions at varying degrees of approximation to determine the appropriate degree of approximation for their application.

While this concept is not new, indeed the Boltzmann Fokker-Planck model has been in use for some time, the addition of moment preserving methods to the singular part of the DCS allows greater flexibility in the choosing of the cutoffs or synthetic parameters. That is, we may simulate more of the DCS with the moment preserving models for the same accuracy than with the Fokker-Planck model. In addition, the moment preserving models can be either smooth operators for deterministic calculations or probability distributions for Monte Carlo calculations. This is a flexibility that cannot rigorously be given by the Fokker-Planck model.

For transport problems with a natural cutoff or μ_{min} that is associated with the problem, one may use the moment preserving schemes to enhance the accuracy of the Fokker-Planck method. Thus, while Fokker-Planck would still require a decomposition method to be valid for these problems, a two or four moment model can simulate the physics accurately without a decomposition scheme. This has the potential to drastically reduce the work required for this class of problems.

Finally, we have seen that a blind application of moment preserving methods to the differing physics of the transport problem separately can lead to unphysical and thus inaccurate results for dose computations. This is due to the local nature of dose computations requiring a sensitive treatment of the elastic scattering. We have seen that a simple condensed history like method, where the mean free path of the elastic scattering pseudo-DCS is set to 1/100th of the mean free path of the inelastic scattering DCS, can be used to rectify this problem. However, such a method can be expensive when used with the simple moment preserving inelastic scattering models. This means that, though the inelastic scattering is well approximated by using moment preserving methods alone, a hybrid method is required for combined scattering. The hybrid method allows us to adjust the mean free path to a large enough value, while still maintaining accuracy, to keep the problem tractable in Monte Carlo calculations.

Chapter 7

Conclusions and Future Work

We have seen that the moment preserving methods combined with a hybrid technique can be a robust and efficient means for accurately solving the transport equations for high energy charged particles. We see huge speedups for particles of very high energy where the scattering is very forward peaked. In this region, the Fokker-Planck limit is valid. However, the Fokker-Planck approximation, and thus the Fermi approximation, are very slow to converge to the true solution with $\overline{\mu} \to 1$.

A moment preserving approach speeds up this convergence since more eigenvalues are precisely preserved, and other eigenvalues are accurately approximated. However, the higher order methods still give only marginal gains over the Fokker-Planck approximation. In order to capture the higher order modes of the solution, a hybrid method must be used. In a hybrid method, less of the DCS needs to be approximated by the moment preserving method. This allows the hybrid methods to maintain efficiency while still giving an excellent approximation to the physics of the problem.

There has been much interest in using the moment preserving methods to improve the condensed history method. This method is known to perform badly near boundaries and interfaces. Using moment preserving methods to define pseudo-differential cross sections that may be used to perform the transport within a step would eliminate this error because it does not require the sampling of a predetermined distribution.

A method for doing this in MCNP6 has been implemented by Harding[6]. He used discrete moment preserving methods to approximate the inelastic scattering of electrons, much like we did in this thesis. A similar implementation for the elastic scattering could also be done. However, other approaches that use the predetermined distributions already present within the condensed history code could also be developed.

Another requirement for future work is the extension of these methods to the production of secondary particles. In an analog Monte Carlo simulation, secondary particles are easily sampled based on the magnitude of the energy transferred during a collision. However, a moment preserving method relies on the formation of a pseudo-DCS. The structure of this DCS, by necessity, cannot be used to sample physical events. Thus, a consistent way of sampling secondaries along a track must be formulated. To be consistent, the method would require some connection to the moment preserving approach discussed in this thesis.

Though we have shown the benefits of the moment preserving methods for heavy and light charged particles, there is still much work to be done. Future work should be focused on the implementation of these methods into a production level Monte Carlo code. Extensive studies of the advantages and disadvantages of using the moment preserving methods in place of the condensed history method should be considered, and the appropriate method for incorporating moment preserving methods should be determined.

Appendix A

Differential Cross Section Derivation

There are several layers of complexity for computing differential cross sections. The first layer, which uses only classical ideas, can be very detailed and understandable. The addition of special relativity adds the additional complexity of treating space and time on the same footing. This leads to more complex relationships between energy and momentum. The only appropriate way to treat collisions between charged particles is to use quantum mechanics. This requires an entirely new set of methods and approximations.

The object here is to gather each of these physical models into one place where the reader may see how to treat scattering appropriately given any level of approximation. The motivation for this appendix is the scattered and often incomplete treatment that cross section derivation is given in many books. Often times, a formula is stated with very little discussion on its origin or validity, much like what was done in Chapter 3. The hope here is to give the reader more insight to these formulas.

A.1 Full Classical Treatment

The first step in this venture is to obtain an equation of motion. This can be done using Lagrangian mechanics, Hamiltonian mechanics, or any other classical method. Each approach has its advantages based on what is known and what information is needed. Hamiltonian mechanics gives the equation of motion of a particle when the kinetic energy $T(q, \dot{q})$ and potential energy $U(q, \dot{q})$ are both well known functions of position and velocity of the particle. Also, the equations are first order equations with direct connections to conservation theorems. Thus, it becomes the optimal methodology here.

Before substituting the potential, we can actually get the equation of motion for a general potential U arising from a stationary scattering center in the lab frame. Using polar coordinates, the kinetic energy of the system of particles can be written

$$T = \frac{1}{2}M_i(\dot{r}_i^2 + r_i^2\dot{\theta}_i{}^2) + \frac{1}{2}M_t(\dot{r}_t^2 + r_t^2\dot{\theta}_t{}^2) \tag{A.1}$$

The Lagrangian of the system is defined as $L = T - U$ and can be given in the present case by

$$L = \frac{1}{2}M_i(\dot{r}_i^2 + r_i^2\dot{\theta}_i{}^2) + \frac{1}{2}M_t(\dot{r}_t^2 + r_i^2\dot{\theta}_t{}^2) - U(|r_1 - r_2|) \tag{A.2}$$

It is typical to consider these problems in the center of mass frame where we let

$$M_i r_i + M_t r_t = 0 \tag{A.3}$$

$$r = r_i - r_t \tag{A.4}$$

$$\theta_i = \theta_t \equiv \theta \tag{A.5}$$

Then the Lagrangian in the center of mass reduces to

$$L = \frac{1}{2}\gamma(\dot{r}^2 + r^2\dot{\theta}^2) - U(r) \tag{A.6}$$

$$\gamma = \frac{M_i M_t}{M_i + M_t} \tag{A.7}$$

This is tantamount to ignoring the transverse displacement of the center of mass of the system during the collision; this is typically an uninteresting quantity and is not needed.

In Hamiltonian mechanics, the equations of motion are given by

$$\begin{aligned} \dot{q}_n &= \frac{\partial H}{\partial p_n} && \text{(A.8)} \\ -\dot{p}_n &= \frac{\partial H}{\partial q_n} && \text{(A.9)} \\ H &= \sum_n p_n \dot{q}_n - L && \text{(A.10)} \end{aligned}$$

where $q_n = r, \theta$ and p_n are the generalized momenta given by

$$p_n = \frac{\partial L}{\partial \dot{q}_n}. \tag{A.11}$$

Though these equations look complicated, they reduce the equations of motion to four first order ordinary differential equations in two dimensions. In the present case, this gives

$$\begin{aligned} \dot{p}_\theta &= \frac{d}{dt}\frac{\partial L}{\partial \theta} = 0 && \text{(A.12)} \\ \rightarrow l &\equiv \gamma r^2 \dot{\theta} = \text{constant} && \text{(A.13)} \end{aligned}$$

This is an expression of the conservation of angular momentum. The other equations of motion could be used to solve the system. However, the conservation of energy gives us the final integral of the motion that we seek since conservation of momentum is automatically satisfied in the center of mass coordinate system.

$$\begin{aligned} E = \text{constant} \quad &= T + U \\ &= \frac{1}{2}\gamma \dot{r}^2 + \frac{1}{2}\gamma r^2 \dot{\theta}^2 + U(r) \\ &= \frac{1}{2}\left(\gamma \dot{r}^2 + \frac{l^2}{\gamma r^2}\right) + U(r) && \text{(A.14)} \end{aligned}$$

Solving this for $\dot{r}$ gives

$$\dot{r} = \sqrt{\frac{2}{\gamma}(E - U(r)) - \frac{l^2}{\gamma^2 r^2}} \tag{A.15}$$

Finally, we may obtain an equation of the form $\theta(r)$ by noting $\dot{r} = \dot{\theta}\, dr/d\theta$. Substituting, using separation of variables and integrating we obtain

$$\theta(r) = \int_{r_1}^{r_2} \frac{(l/r^2)dr}{\sqrt{2\gamma\left(E - U - \frac{l^2}{2\gamma r^2}\right)}} \tag{A.16}$$

This integral will give the equation of motion $\theta(r)$ for any central potential $U(r)$. To eliminate the angular momentum from the equation, we introduce the impact parameter b as the distance of closest approach if the particle had not been deflected. This quantity is depicted in Fig.(A.1).

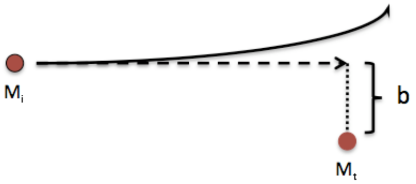

Figure A.1: Impact parameter for incident particle deflected by the field from the target particle

This quantity is useful because the angular momentum can be expressed as

$$\begin{aligned} l &= \gamma\dot{\vec{r}} \times \vec{r} \; = \; M_i v_i b \\ &= b\sqrt{2\gamma T_0} \end{aligned} \tag{A.17}$$

where T_0 is the initial kinetic energy. Then Eq.(A.16) can be rewritten after some simplification as

$$\theta(r) = \int_{r_1}^{r_2} \frac{(b/r^2)dr}{\sqrt{1 - \frac{U(r)}{T_0} - \frac{b^2}{r^2}}} \tag{A.18}$$

We may use the bare charge Coulomb potential energy $U(r) = -Z_i Z_t e^2/r$ with charge in statacoulomb so that the constant $1/4\pi\epsilon_0 = 1$. Also, we may take $r_1 = -\infty$ since we are considering a particle moving into a potential in an initially undeflected trajectory. The resulting form of Eq.(A.18) has an exact solution given by

$$\frac{A}{r} = 1 + B\cos\Theta \tag{A.19}$$

$$A = \frac{2b^2\gamma E}{Z_i Z_t e^2} \tag{A.20}$$

$$B = \sqrt{1 + \frac{4E^2b^2}{Z_i Z_t e^2}} \tag{A.21}$$

$$\Theta = \frac{\theta}{2} - \frac{\pi}{2} \tag{A.22}$$

This is the hyperbolic solution promised in Chapter 3. In scattering problems, the asymptotic scattering angle is the desired quantity. A particle obtains this angle in the limit as $r \to \infty$. Then we can write

$$\cos^2\Theta_\infty = \frac{1}{1 + 4E^2b^2/(Z_i Z_t e^2)^2} \tag{A.23}$$

Solving this for the impact parameter b obtains

$$\begin{aligned} b^2 &= \frac{(Z_i Z_t e^2)^2}{4E^2}(\sec^2\Theta_\infty - 1) \\ &= \frac{(Z_i Z_t e^2)^2}{4E^2}\cot^2\frac{\theta_\infty}{2} \end{aligned} \tag{A.24}$$

The Rutherford cross section is obtained by using the change of variables described in Chapter 3. Many other classical differential cross sections may be obtained by substituting a different central potential for $U(r)$. For instance, the screening of outer electrons may be approximately accounted for by using a potential of the form

$$U(r) = -\frac{Z_i Z_t e^2}{r}\exp\left(-\frac{r}{a}\right) \tag{A.25}$$

where a is some effective atomic radius. Other screening functions that can replace the exponential in Eq.(A.25) have been introduced. For an excellent summary, see the discussion by Keen[22].

A.2 Nonrelativistic Quantum Mechanics

The description given above, though used in some limited cases, is often not a valid description of charged particle kinematics. At length scales and momenta that are comparable with Planck's constant h, we are forced to use quantum theory to obtain differential cross sections. Fortunately, this complication does not extend to the transport equation since all of the physics of scattering is wrapped into the cross sections. However, we will see that an exact treatment like the one given previously cannot be obtained, even with the simplest quantum mechanical relations. We will give an overview of the calculations involved in computing differential cross sections in the non-relativistic limit in this section.

A.2.1 Coulomb Interaction and Matter Waves

It is convenient to consider the incident particle as a wave when treating the scattering of that particle using quantum mechanics. In that case, the Schrödinger equation is a valid description of the kinematics of that particle. Using a center of mass treatment as before, the Schroedinger equation becomes

$$-\frac{h}{4\pi\gamma}\nabla^2\psi - U(r)\psi = E\psi \tag{A.26}$$

The function ψ is the wave function for the system and completely describes the system's state at any time. Also, we have the Coulomb potential $U(r)$ as before. We immediately see a problem with our description in the framework of quantum mechanics. The potential function represents a continuous means of transferring energy to the incident particle. However, quantum mechanics arose from the need to describe energy transitions in terms of packets of energy called quanta. Thus, the potential energy must be represented by an operator that gives discrete energy packets to the incident particle. Thus, already we have an approximation to the full formalism.

Nonetheless, we can solve this equation for the particular form that the potential energy takes for a continuous Coulomb field. The solution follows that given by Messiah[21]. We can substitute the parameter groups

$$E = \frac{h^2 k^2}{8\pi^2 \gamma} \tag{A.27}$$

$$b = \frac{2\pi Z_1 Z_2 e^2}{hv} \tag{A.28}$$

into Eq.(A.26) with v the velocity of the incident wave packet and k the wave number. Doing so gives

$$\nabla^2 \psi + \left(k^2 - \frac{2bk}{r}\right)\psi = 0 \tag{A.29}$$

Solutions of the form $e^{ikz} f(r-z)$ exist for this equation. Substituting this form into the equation and letting $u = ik(r-z)$ gives the ordinary differential equation

$$u\frac{d^2 f}{du^2} + (1-u)\frac{df}{du} + ibf(u) = 0 \tag{A.30}$$

The solution to this equation is

$$f(u) = C_1 F(-ib|1|u) \tag{A.31}$$

where C_1 is a constant to be determined and $F(\alpha|\beta|x)$ is the confluent hypergeometric series. Thus, the wave function becomes

$$\psi = C_1 e^{ikz} F[-ib|1|ik(r-z)] \tag{A.32}$$

This solution can be split into two distinct functions whose asymptotic forms are

$$\psi_i = e^{i[kz+b\ln k(r-z)]}\left[1+\frac{b^2}{ik(r-z)}+...\right] \tag{A.33}$$

$$\psi_s = -e^{i[kz-b\ln k(r-z)]}\frac{b\Gamma(1+ib)}{k(r-z)\Gamma(1-ib)}\left[1+\frac{(1+ib)^2}{ik(r-z)}+...\right] \tag{A.34}$$

The function ψ_i is interpreted as the plane wave representing the unscattered beam and ψ_s is interpreted as a scattered wave. It can be rewritten using the relation $z = r\cos\theta$ as

$$\psi_s \approx \frac{1}{r}\exp[i(kr - b\ln 2kr)]g(\theta) \tag{A.35}$$

$$g(\theta) = -\frac{b}{2k\sin^2(\theta/2)}\exp[-ib\ln(\sin^2\theta/2) + 2i\sigma_0] \tag{A.36}$$

$$\sigma_0 = \arg\Gamma(1+ib) \tag{A.37}$$

Forming the current densities

$$j = \frac{h}{4\pi i\gamma}[\psi^*\nabla\psi - \psi(\nabla\psi)^*] \tag{A.38}$$

for both the incident wave and the wave scattering into the range of angles between θ and $\theta + d\theta$ and taking their ratio gives the differential cross section

$$\sigma(\theta) = |g(\theta)|^2 = \frac{b^2}{4k^2\sin^4(\theta/2)} \tag{A.39}$$

$$= \left(\frac{Z_1Z_2e^2}{4E}\right)^2\frac{1}{\sin^4(\theta/2)} \tag{A.40}$$

This form is identical to the asymptotic classical solution. However, the approximations made in getting to this form of the DCS leave it as approximate as the classical version. The difficulty in treating this potential with wave mechanics is its very long range. The wave function never truly leaves the influence of the potential. The reader is referred to Messiah for a good discussion on these matters.

A.2.2 General Potentials and the Partial Wave Expansion

The solution to the Schrödinger equation for a Coulomb potential is special for at least two reasons. First, the equation can be recast into a form that has an analytic solution in terms of known functions. Second, the potential has such a long range that the usual method for solving these problems, that of a partial wave expansion, leads to a slowly converging series.

However, the bare charge Coulomb potential is itself an approximation to true physics of elastic scattering. It was mentioned briefly in the previous section that the screening by atomic electrons of the target nucleus results in a much more rapidly decaying potential with distance from the nucleus. Furthermore, it can be shown that any potential that tends to zero more rapidly than $1/r$ when substituted into Eq.(A.26) leads to asymptotic eigensolutions of the form

$$\psi_\infty = e^{ikz} + f(\Omega)\frac{e^{ikr}}{r} \tag{A.41}$$

It can be argued that the DCS is then given by

$$\sigma_e(\Omega) = |f(\Omega)|^2 \tag{A.42}$$

Thus our task is to find this function for a given scattering potential. We note that the functions ψ_r and $f(\Omega)$ are independent of the azimuthal angle ϕ. Thus, the functions can be expanded in Legendre polynomials yielding

$$\psi_r(\theta) = \sum_{l=0}^{\infty} \frac{y_l(r)}{r} P_l(\mu) \tag{A.43}$$

$$f(\theta) = \sum_{l=0}^{\infty} f_l P_l(\mu) \tag{A.44}$$

$$\mu = \cos\theta \tag{A.45}$$

For the general problem, we have our solution $\psi_r(\theta)$ given in terms of the functions

$y_l(r)$ solving the equations

$$\frac{d^2y_l}{dr^2} + \left(k^2 - U(r) - \frac{l(l+1)}{r^2}\right) y_l = 0 \tag{A.46}$$

This equation arises from the separation of variables of the Schrödinger equation. This function must be asymptotically equivalent to the function ψ_∞. Expanding the asymptotic form in Eq.(A.41) gives

$$\psi_\infty = \sum_{l=0}^{\infty} \left((2l+1)i^l j_l(kr) + f_l \frac{e^{ikr}}{r}\right) P_l(\mu) \tag{A.47}$$

by using the expansion of e^{ikz} in terms of spherical Bessel functions given by

$$e^{ikz} = \sum_{l=0}^{\infty} (2l+1)i^l j_l(kr) P_l(\mu). \tag{A.48}$$

Multiplying ψ_∞ by r and using the asymptotic form for $j_l(kr)$

$$j_l(kr) \approx \frac{1}{kr}\sin(kr - l\pi/2) = \frac{e^{ikr-l\pi/2} - e^{-(ikr-l\pi/2)}}{2ikr} \tag{A.49}$$

gives the series

$$r\psi_\infty \approx \sum_{l=0}^{\infty} \left[(-1)^{l+1}\frac{2l+1}{2ik}e^{-ikr} + \left(\frac{2l+1}{2ik} + f_l\right) e^{ikr}\right] P_l(\mu) \tag{A.50}$$

Setting this equal to y_l and noting that it has the asymptotic form given by

$$y_l \approx a_l \sin(kr - l\pi/2 + \delta_l) \tag{A.51}$$

which can be derived from Eq.(A.46), the following equalities must hold if the asymptotic form is to be given by ψ_∞:

$$a_l = i^l \frac{2l+1}{k} e^{i\delta_l} \tag{A.52}$$

$$f_l = \frac{2l+1}{k} e^{i\delta_l} \sin\delta_l \tag{A.53}$$

The parameter δ_l is the phase shift characterizing the scattering of the incident particle. The desired function for computing the DCS becomes

$$f(\theta) = \frac{1}{k}\sum_{l=0}^{\infty}(2l+1)e^{i\delta_l}\sin\delta_l P_l(\mu) \tag{A.54}$$

The summation of this series requires the values δ_l. Knowing these values requires the exact solution and analysis of Eq.(A.46). However, the Born approximation gives the phase shifts as

$$\delta_l \approx \frac{8\pi^2\gamma k}{h^2}\int_0^{\infty} j_l^2(kr)U(r)r^2 dr \tag{A.55}$$

when $U(r)$ is sufficiently small and δ_l is near zero. If one knows the phase shift for some potential $U(r)$ and would like to estimate the potential for $\hat{U}(r)$ close to $U(r)$, it is given by

$$\delta_l - \hat{\delta}_l \approx \frac{8\pi^2\gamma}{h^2 k}\int_0^{\infty} \hat{y}_l^2(U(r) - \hat{U}(r))dr \tag{A.56}$$

This is known as the generalized Born formula.

A.3 Relativistic Quantum Mechanics

In all of the discussions so far, it has been assumed that the particle speed is small compared to the speed of light. However, in the high energy particle physics world, this assumption is not valid in most applications. If it still assumed that the field is continuous, then the Dirac equation for the system may be used to describe the particles relativistically.

$$i\gamma^{\nu}\partial_{\nu}\psi - e\gamma^{\nu}A_{\nu}\psi - m\psi = 0 \tag{A.57}$$

The summation convention (i.e. summation over repeated indices) is used from here on unless otherwise noted. All indices range over the integers 0, 1, 2, and 3. The parameter m now expresses the reduced mass of the system given in Eq.(A.7). A_ν is the electromagnetic field four vector that is given by a particular form of Maxwell's equations. It represents the potential energy $U(r)$ in a form more convenient for solving the Dirac equation. Also, the Dirac matrices γ^ν have been introduced. They satisfy

$$\gamma^\nu\gamma^\mu + \gamma^\mu\gamma^\nu = 2g^{\mu\nu} \tag{A.58}$$

where $g^{\mu\nu}$ is the spacetime metric given in special relativity by simply

$$g^{\mu\nu} = \begin{bmatrix} 1 & 0 & 0 & 0 \\ 0 & -1 & 0 & 0 \\ 0 & 0 & -1 & 0 \\ 0 & 0 & 0 & -1 \end{bmatrix} \tag{A.59}$$

Finally, we have introduced the generalization of the gradient to space time given by

$$\partial_\mu = \left[\frac{\partial}{\partial t}, \nabla\right] \tag{A.60}$$

$$\partial^\mu = \left[\frac{\partial}{\partial t}, -\nabla\right] \tag{A.61}$$

$$\partial_\mu\partial^\mu = \frac{\partial^2}{\partial t^2} - \nabla^2 \tag{A.62}$$

The qualitative differences between the Dirac equation and the Schrödinger equation is that spin is explicitly treated by the form of the solution ψ. The solution to the Dirac equation is a bispinor, a four component vector-like quantity that has certain transformation properties. The components are interpreted as the positive and negative energy states of the spin up and spin down states of the particle. This equation is required for the relativistic treatment of electrons and any other swift particle with non-integer spin. For slow particles, the spin can be accounted for while still using the Schrödinger equation by hypothesizing its existence in advance.

For particles that don't have spin, the Dirac equation can be reduced to the Klein-Gordon equation given by

$$(\partial_\mu + ieA_\mu)(\partial^\mu + ieA^\mu)\psi + m^2\psi = 0 \tag{A.63}$$

It is this form that can be derived from the correspondence principle and the relativistic relation

$$E^2 = p^2c^2 + m^2c^4 \tag{A.64}$$

when the natural units are employed where $c = h = 1$. The Klein-Gordon and the Dirac equations can be approximately solved using methods described above. However, the solutions are much more complicated and will not be given here. It is worth noting that the Mott DCS for electrons is derived using the Dirac equation. Numerous other differential cross sections exist whose origin is the Klein-Gordon equation.

Extending quantum mechanics to relativistic particles often requires a relativistic treatment of the fields. This principle is the foundation of quantum field theory. The basic idea is to obtain operators that have been quantized through a specific and complicated procedure. These fields are obtained via the correspondence principle applied to a set of classical field equations (i.e. Maxwell's equations). Once the operators have been obtained, the formalism of collision theory must be used to obtain the cross sections. That is, the cross section is given by

$$\sigma_{a\rightarrow b} = \frac{(2\pi m)^2}{h^4} |<\phi_b|U|\psi_a>|^2 \tag{A.65}$$

That is, the scattering from state a given by wave function ψ_a to state b given by wave function ϕ_b is determined by the transition probability represented by the inner product $<\phi_b|U|\psi_a>$. The operator U determined by a detailed quantum field theory treatment may contain several transitions from a to b, and a sum over each of these transitions is required. Also, the actual wave functions ψ_a is not know a priori but is the solution to a complicated equation. However, the Born approximation is equivalent to setting $\psi_a = \phi_a$ where ϕ is just the plane wave solution to the equation for scattering problems. This solution is often known in advance, and the determination of the scattering DCS amounts to an integral once the field U is characterized.

References

[1] J. Doggett and L. Spencer, “Elastic Scattering of Electrons and Positrons by Point Nuclei,” *Physical Review*, vol. 103, p. 1597, 1956.

[2] J. Duderstadt and W. Martin, *Transport Theory.* John Wiley and Sons, 1978.

[3] J. E. Morel, “On the validity of the extended transport correction for low energy electron transport,” *Nuclear Science and Engineering*, vol. 71, pp. 64–71, 1979.

[4] D. Hubbard, *How to Measure Anything: Finding the Value of Intangibles in Business.* John Wiley and Sons, 2007.

[5] M. H. Kalos and P. A. Whitlock, *Monte Carlo Methods.* John Wiley and Sons, 1986.

[6] L. T. Harding, “Monte carlo simulations of electron and positron energy-loss straggling,” Master’s thesis, University of New Mexico, 2006.

[7] M. J. Berger, *Methods in Computational Physics*, vol. 1, ch. Monte Carlo Calculation of the Penetration and Diffusion of Fast Charged Particles, pp. 135–215. Academic Press, 1963.

[8] X-5 Monte Carlo Team, “MCNP - a general purpose Monte Carlo N-particle transport code, version 5,” *Technical Report LA-UR-03-1987, LANL*, 2003.

[9] W. R. Nelson, H. Hirayama, and D. W. O. Rogers, “The EGS4 code system,” *Technical Report SLAC-265, SLAC*, 1985.

[10] J. A. Halbleib, R. P. Kensek, T. A. Mehlhorn, G. D. Valdez, S. M. Seltzer, and M. J. Berger, “ITS version 3.0: The Integrated TIGER Series of coupled electron/photon Monte Carlo,” *Technical Report SAND91-1634, SNL*, 1992.

[11] L. Landau, “On the energy loss of fast particles by ionization,” *Journal of Physics: Soviet*, vol. 8, p. 201, 1944.

[12] S. Goudsmit and J. L. Saunderson, "Multiple scattering of electrons i," *Physical Review*, vol. 57, p. 24, 1940.

[13] S. Goudsmit and J. L. Saunderson, "Multiple scattering of electrons ii," *Physical Review*, vol. 58, p. 36, 1940.

[14] G. Moliere, "Theorie der streuung schneller geladener teilchen i: Einzelstreuung am abgeschirmten coulomb-feld," *Z. Naturforch*, vol. 2a, p. 133, 1947.

[15] P. V. Vavilov, "Ionization losses of high-energy heavy particles," *Soviet Physics JETP*, vol. 5, pp. 749–751, November 1957.

[16] B. Rossi, *High-Energy Particles.* Prentice-Hall, 1952.

[17] L. Waters, "Mcnpx user's manual," *Technical Report LA-UR-02-2607, LANL*, 2002.

[18] E. Larsen, "A theoretical derivation of the condensed history algorithm," *Annals of Nuclear Energy*, vol. 19, no. 10-12, pp. 701–714, 1992.

[19] R. D. Evans, *The Atomic Nucleus.* McGraw-Hill Book Company, Inc., 1955.

[20] S. Thornton and J. Marion, *Classical Dynamics of Particles and Systems.* World Scientific, 5 ed., 2005.

[21] A. Messiah, *Quantum Mechanics*, vol. 1. John Wiley & Sons, 1958.

[22] N. Keen, "Ion cross section and monte carlo simulations using multigroup boltzmann fokker-planck transport," Master's thesis, University of New Mexico, 1999.

[23] C. Möller, "Zur theorie des durchgang schneller elektronen durch materie," *Ann. Phys.*, vol. 14, p. 568, 1932.

[24] J. E. Turner, *Atoms, Radiation, and Radiation Protection.* John Wiley and Sons, 1992.

[25] E. Larsen and C. Börgers, "On the accuracy of the Fokker-Plank and Fermi pencil beam equations for charged particle transport," *Medical Physics*, vol. 23, pp. 1749–1759, October 1996.

[26] M. A. Peterson, "Angular Distributions in Multiple Scattering," *Physical Review A*, vol. 28, p. 135, 1983.

[27] C. Leakes and E. Larsen, "Generalized Fokker-Planck Approximations of Particle Transport with Highly Forward-Peaked Scattering," *Nuclear Science and Engineering*, vol. 137, p. 236, 2000.

[28] G. C. Pomraning, "The Fokker-Planck Operator as an Asymptotic Limit," *Mathematical Models and Methods in Applied Science*, vol. 2, p. 21, 1992.

[29] I. Stakgold, *Boundary Value Problems of Mathematical Physics.* Siam, 2000.

[30] E. T. Wright, "A Detector for Muon Tomography: Data Aquisition and Preliminary Results," Master's thesis, University of Texas, 2007.

[31] A. Prinja and G. Pomraning, "Higher-order multiple scattering theories for charged particle transport," *Medical Physics*, vol. 23, p. 1761, October 1996.

[32] A. K. Prinja, "Stochastic interpretation of the fermi pencil beam problem," *Transport Theory and Statistical Physics*, vol. 26, p. 555, 1997.

[33] G. C. Pomraning, "Higher order fokker-planck operators," *Nuclear Science and Engineering*, vol. 124, p. 390, 1996.

[34] H. Lewis, "Multiple scattering in an infinite medium," *Physical Review*, vol. 78, p. 526, 1950.

[35] F. Graziani, ed., *Computational Methods in Transport*, vol. 48 of *Lecture notes in Computational Science and Engineering.* Springer Berlin Heidelberg, February 2006.

[36] D. P. Sloan, *A New Multigroup Monte Carlo Scattering Algorithm Suitable for Neutral and Charged-Particle Boltzmann and Fokker-Planck Calculations.* PhD thesis, University of New Mexico, 1983.

[37] A. K. Prinja and L. T. Harding, "An energy-loss decomposition scheme for efficient energy straggling computations," *Transactions of the American Nuclear Society*, pp. 503–505, 2003.

[38] E. D. Fichtl, "Methods for electron energy-loss straggling in deterministic and binary statistical media," Master's thesis, University of New Mexico, 2005.

[39] B. C. Franke and A. K. Prinja, "Monte Carlo electron dose calculations using discrete scattering angles and discrete energy losses," *Nuclear Mathematical and Computational Sciences: A century in Review, A century Anew, Gatlinburg, Tenessee, April 6-11*, 2003.

[40] J. Janni *Atomic Data and Nuclear Data Tables*, vol. 27, p. 515, July 1982.

[41] G. Hughes. Personal Communication, 2008.